

Toward a systematic integration of optical remote sensing for inland waters studies

THÈSE N° 8622 (2018)

PRÉSENTÉE LE 26 JUIN 2018

À LA FACULTÉ DE L'ENVIRONNEMENT NATUREL, ARCHITECTURAL ET CONSTRUIT
LABORATOIRE DE PHYSIQUE DES SYSTÈMES AQUATIQUES - CHAIRE MARGARETHA KAMPRAD
PROGRAMME DOCTORAL EN GÉNIE CIVIL ET ENVIRONNEMENT

ÉCOLE POLYTECHNIQUE FÉDÉRALE DE LAUSANNE

POUR L'OBTENTION DU GRADE DE DOCTEUR ÈS SCIENCES

PAR

Vincent Maurice NOUCHI

acceptée sur proposition du jury:

Prof. M. Lehning, président du jury
Prof. A. J. Wüest, Dr D. Bouffard, directeurs de thèse
Prof. T. Kutser, rapporteur
Dr D. Odermatt, rapporteur
Prof. F. Golay, rapporteur



ÉCOLE POLYTECHNIQUE
FÉDÉRALE DE LAUSANNE

Suisse
2018

“Jusqu’ici tout va bien...”

— *La Haine* (1995), de Mathieu Kassovitz.

Acknowledgements

First and foremost, I would like to thank my supervisors, starting with my professor, Johnny Wüest. I am very grateful for the opportunity he gave me to work in his group, the valuable contacts he provided throughout my thesis, and his strong interest in my work. I thank Damien Bouffard for his important support during the tough times of my PhD, and for helping me mature during those five years. To close this paragraph, I would like to express my respect and gratitude to Daniel Odermatt. I sincerely enjoyed working alongside him, he always provided fruitful and interesting discussions, and simply taught me how to do scientific research.

I express my deepest thanks to all the Léman-Baikal team: François Bernard, Natacha Tofield-Pasche, Yosef Akhtman, Dragos Constantin, Kevin Barbieux, Abolfazl Irani, Martin Rehak, Michael Tarasov, Galina Shinkareva, Olga Rusanovskaya, Marie-Caroline Tiffay and everyone who participated in this amazing experience, which is now engraved in my memory. Two very special thanks to my incredible boat captain, Baptiste Bernard, and to the best assistant you can dream of, a true diplomat and a real boss, Ivan Pachenko, whom I am very proud to now call friends.

I am very thankful to all my colleagues from the APHYS laboratory: Théo Baracchini, Oscar Sepúlveda, Hanna Chmiel, Sébastien Lavanchy, Robert Schwefel, Love Raman, Tania Gonin, Hugo Ulloa, and more recently Shubham Krishna for all the great times and their help in all situations. Théo, see you on the road my friend.

A very special thanks to Tiit Kutser, for his guidance, his constructive comments, and for initiating an entire chapter of my thesis. I would also like to express my sincerest thanks to Miki Hondzo for showing me the way of scientific work, for the very interesting discussions, and for the invaluable advice he gave me. In this regard, I am especially thankful to my friend, Nicolas Escoffier, I am not sure I would have finished my PhD without his amazing support, trust, and all the advice he provided. A special thanks also to Nicolas, and Oscar as well, for the proofreading in a critical timing! Finally, I would like to thank Beat Müller for his responsiveness and his contribution to this thesis.

Last but definitely not least, I would like to express my warmest gratitude to my family for their long-lasting support. I thank my dad, my mother, my two sisters, my grandma, my aunts, my uncle, and my cousins for always believing in me, for their patience, and their encouragement.

Abstract

Freshwater resources play a central role in social and economic development of modern civilisations, yet their value is often underestimated and neglected in developed countries. In fact, freshwater habitats are facing unprecedented threat because of human activities, and it is necessary to provide reliable water quality indicators to monitor the response of aquatic systems. In this context, remote sensing has a great potential to provide a complementary source of data for monitoring and understanding the processes involved in inland waters around the world at fine temporal and spatial resolutions.

The scientific approach adopted in this thesis is based on the integration of complementary sources of information provided by state-of-the-art monitoring methods to foster our understanding of freshwater habitats. Specifically, we demonstrate the additional value provided by combining complementary sensors with bio-geochemical measurements and hydrodynamic models, using a rare event in Lake Geneva which got a wide public attention in local newspapers: a calcite precipitation event.

The principal focus of the remote-sensing community has recently been directed towards very turbid waters in order to address the challenges involved with the retrieval of mixed constituent concentrations. In this thesis, I highlight some important challenges relative to clearer waters which also require further attention from the community. Specifically, I provide a solution to account for vertical non-uniformities of water constituent concentrations using simple approximation models in Lake Geneva.

Finally, I provide a comprehensive comparison between state-of-the-art atmospheric correction methods, which are presumably relevant for inland water monitoring and applicable to the new constellation of remote sensors. The aim is to provide reliable recommendations to help forthcoming studies to apply the most suited procedure to their investigation.

Keywords

Remote sensing, inland waters, lake processes, water quality, Lake Geneva, atmospheric correction, Sentinel-2, Landsat-8, MODIS, calcite precipitations.

Résumé

Les ressources en eau douce naturelles occupent une place prépondérante au sein de la société actuelle, et sont malgré tout souvent négligées, considérées comme un bien acquis et inépuisable dans les pays développés. L'impact de l'homme sur ces ressources est pourtant considérable et il apparaît nécessaire de développer des moyens de suivi robustes et réguliers de l'état écologique des écosystèmes. L'enjeu étant de fournir des indices précis pour guider les prises de décisions locales, régionales, et internationales des parties prenantes. Dans ce contexte, la télédétection apporte une solution particulièrement séduisante, à compter que la qualité de ces observations soit assurée.

Dans cette étude, et pour palier à la complexité des lacs et autres réservoirs naturels, nous nous basons sur une nouvelle approche visant à développer nos connaissances vis à vis de ces environnements au moyen d'outils technologiques modernes à notre disposition. Spécifiquement, Nous démontrons le potentiel de combiner différentes plateformes de télédétection avec des analyses bio-géochimiques et des résultats de modèles hydrodynamiques, par le biais d'une étude concernant un événement particulièrement intéressant survenu au sein du Léman à la fin du printemps de l'année 2014. Une précipitation calcite.

Les principaux défis identifiés par la communauté concernent majoritairement les eaux turbides pour lesquelles la décomposition du signal est considérablement complexifiée par la mixture d'éléments rencontrés. Cependant, au sein de cette étude nous attirons l'attention de la communauté sur des défis relatifs à l'observation spatiale d'eaux relativement claires, telles que celles du Léman. Directement, nous proposons des solutions concrètes afin d'améliorer la précisions des produits brutes de la télédétection tout en prenant en compte l'impact saisonnier sur la distribution verticales des éléments de la colonne d'eau.

Finalement, nous fournissons une comparaison détaillée des méthodes contemporaines pour la correction atmosphérique d'appareils de télédétection récemment mis sur orbite autour de la Terre par l'agence spatiale Européenne (ESA, for European Sapce Agency). Au travers de cette étude, nous procurons des recommandations afin de guider les futurs utilisateurs vers la solution la plus adaptée au sujet d'étude en question.

Mots-clés

Télédétection, lacs, processus des lacs, qualité des eaux, Léman, Sentinel-2, Landsat-8, MODIS, précipitation calcaire

Contents

Acknowledgements.....	iii
Abstract.....	v
List of Figures.....	xiii
List of Tables	xvii
Chapter 1 Introduction	1
1. 1. Inland water monitoring	2
1. 2. Remote sensing of inland water	2
1.2.1. Optical properties of natural waters.....	3
1.2.2. Radiative transfer theory.....	8
1.2.3. Atmospheric contribution	8
1. 3. Research objectives	10
1.3.1. Scope.....	10
1.3.2. Questions	11
1. 4. Structure of the dissertation	11
Chapter 2 Resolving biogeochemical processes in lakes using remote sensing.....	13
2. 1. Introduction	14
2. 2. Study site and Methods	16
2.2.1. Satellite data and processing.....	17
2.2.2. In-situ dataset.....	18
2.2.3. River intrusion model	19
2.2.4. Hydrodynamic model	20
2.2.5. Calculation of the calcite saturation index Ω	20
2. 3. Results and discussion.....	21
2. 4. Conclusion.....	31
Chapter 3 Effects of non-uniform vertical constituent profiles on remote-sensing reflectance of oligo- to mesotrophic lakes.....	35
3. 1. Introduction	36
3. 2. Methods.....	38
3.2.1. Site description	38
3.2.2. Bio-geochemical constituents.....	39

3.2.3. Vertical profile approximations.....	40
3.2.4. Radiometric measurements.....	40
3.2.5. Specific Inherent Optical Properties.....	41
3.2.6. Radiative Transfer Model.....	43
3.2.7. Optical closure.....	43
3.2.8. Statistics.....	44
3.2.9. Inversion Algorithms.....	44
3. 3. Results.....	45
3.3.1. Optical closure.....	45
3.3.2. Average annual course of constituent non-uniformities.....	46
3.3.3. Vertical approximation of seasonally typical profiles.....	47
3.3.4. Frequency and temporal distribution of non-uniformities.....	50
3.3.5. Assessment of profile approximation models.....	51
3.3.6. Relative relevance of CHL and TSM.....	52
3.3.7. Band-ratio algorithm.....	53
3. 4. Discussion and conclusions.....	54
Chapter 4 Inter-comparison of atmospheric corrections for S-2 observations over Lake Geneva.....	59
4. 1. Introduction.....	60
4. 2. Methods.....	60
4.2.1. Lake Geneva.....	61
4.2.2. Atmospheric corrections.....	64
4.2.3. Statistics.....	66
4. 3. Preliminary results and discussion.....	67
4.3.1. Atmospheric conditions.....	67
4.3.2. Water-leaving reflectance.....	70
4.3.3. Water optical properties.....	72
4.3.4. Environmental factors.....	74
4. 4. Conclusion & perspectives.....	75
Chapter 5 Conclusion.....	79
5. 1. Main achievements.....	80
5. 2. Outlook.....	81

References	85
Curriculum Vitae	101

List of Figures

Figure 1-1: Illustration of the depth weighting function from Gordon and Clark (dashed light blue line), Zaneveld et al. (dashed dark blue line) and actual K_d profile (blue line). Source: Piskozub, 2008.	6
Figure 1-2: Left panel: absorption spectra of pure water (blue), NAP (red), CDOM (yellow), and phytoplankton (green). Right panel: scattering from pure water (blue), phytoplankton (green) and TSM (red). All data were taken from WASI-2D (Gege, 2014) except for the backscattering of phytoplankton taken from IOCCG report 5 (2006).	8
Figure 1-3: Schematics of the light paths for a sensor observing natural waters.	9
Figure 2-1: Overview map of Lake Geneva. The two sampling stations in the lake (SHL2) and in the Rhône (Porte-du-Scex, PS) are indicated.	17
Figure 2-2: Sketch showing the main processes occurring during the intrusion of the Rhône waters (1) in the lake (2): entrainment of lake waters into the Rhône plume (3) and detrainment of particles from the Rhône water into the surface layer of the lake (4).	19
Figure 2-3: Distribution of CHL (left) and TSM (right) from June 8 to 21, 2014. Each row corresponds to a different date.	22
Figure 2-4: Landsat-8 image of Lake Geneva from May 23, 2014. The inset zoom (top right) shows the Rhône inflow area. Crosses indicate the pixels where water reflectance spectra shown in Figure 2-8 were collected.	24
Figure 2-5: Landsat-8 image of Lake Geneva from June 8, 2014. The inset zoom shows the Rhône inflow area. Crosses indicate the pixels where water reflectance spectra shown in Figure 2-8 were collected. Note that the image histogram was stretched to show the different hydrodynamic structures and colours.	24
Figure 2-6: Landsat-8 image of Lake Geneva from June 15, 2014. The inset zoom shows the Rhône inflow area. Crosses indicate the pixels where water reflectance spectra shown in Figure 2-8 were collected.	25
Figure 2-7: Landsat-8 image of Lake Geneva from July 17, 2014. The inset zoom shows the Rhône inflow area. Crosses indicate the pixels where water reflectance spectra shown in Figure 2-8 were collected. Note that most of the bright area next to the inflow is due to sun glint not due to water turbidity.	25
Figure 2-8: ρ_w collected from four Landsat-8 images. Exact locations of the extracted pixels are shown in Figure 2-4 to Figure 2-7.	26
Figure 2-9: CIPEL CTD profiles at station SHL2 of CHL (left) and turbidity (right) for June 2 2014 (black) and June 30 2014 (blue).	27

Figure 2-10: Histogram of the depth distribution of Rhône intrusions into Lake Geneva for early April 2014 (black) and for end of June 2014 (blue). River data have a time interval of 10 min and are taken over 5 days before the measurements at SHL2.	28
Figure 2-11: The background correspond to the Landsat-8 image of Lake Geneva from June 15, 2014 (Fig. 6). The overlaid surface plot represent the percent of particles originating from the Rhône River inflow area, passing by an element of the grid of the hydrodynamic model. One particle was released around the Rhône River mouth (maximum spread of 500 m) every 10 minutes between June 8 and June 15 2014 and advected into the lake using the average velocity field between 1 and 15 m depth.	28
Figure 2-12: Ω at SHL2 for June 2 2014 (left), and Ca precipitation (right) estimated over the month of June 2014 plotted as the difference in the Ca concentration between June 30 and June 2. The Ca depletion is restricted to the top 20 m with the maximum right at the surface. The integrated Ca precipitation for this event was 44 g m^{-2} in the top 20 m.	30
Figure 2-13: Rhône physico-chemical parameters at PS from 2011 to 2017.	31
Figure 3-1: Overview map of Lake Geneva. SHL2 indicates the main location of routine monitoring.	39
Figure 3-2: PD between 15 in-situ measured and simulated R^- for the concentrations obtained by the Nelder-Mead optimization. $N = 15$, boxes are 1 st and 3 rd quartile and bars extend to min and max. The line in each box corresponds to the median.	46
Figure 3-3: Irradiance reflectance at 1 m depth from in-situ measurements (solid lines) and simulated by Hydrolight (dashed lines) for the three different stations listed in Table 3-2.	46
Figure 3-4: Average annual course of CHL(z) (top) and TSM(z) (bottom panel) at station SHL2 (Figure 3-1) in the years 2002 - 2015, aggregated by moving a 15-days averaging time window, and using interpolated 10 cm depth intervals. The black line in the TSM plot shows the thermocline depth aggregated by moving a 15-days averaging time window.	47
Figure 3-5: Typical examples of CHL profiles (top row), TSM profiles (middle row) and resulting R_{rs} (bottom row) for winter, spring, summer and autumn (left to right). The legend in the top left plot indicates the color code for each simulation and in the bottom row the PD and θ values of M1, M5, GAL, TLM and LIN against INT.	49
Figure 3-6: Seasonal evolution of the spectral angle for the uniform profiles M1 and M5 (top row) and for the three non-uniform approximation models GAL, TLM and LIN (bottom row).	51

Figure 3-7: Maximum PD (top row) and median PD (bottom row) over all simulations for INT input profiles against the uniform (left) and non-uniform profile approximation models (right).	52
Figure 3-8: Scatter plot of GONS (top row) and OC4 (bottom row) algorithms applied on M1 (left) and M5 (right) against R_{rs} from measured CHL(z). The grey line represents the 1:1 relationship and the black line represent the regression with the resulting slope and R^2 provided in the text box of each plot. Note that a log-log scale is applied to cope with the scatter of OC4 samples while a lin-lin scale is required to display the negative values in GONS.....	54
Figure 4-1: S2 acquisition over Lake Geneva on June 24, 2016. The red circles show the water sampling locations for the same day.	62
Figure 4-2: S2 acquisition over Lake Geneva on September 22, 2016. The red circles show the water sampling locations for the same day.	62
Figure 4-3: S2 acquisition over Lake Geneva on June 19, 2017. The red circles show the water sampling locations on June 22, 2017.	63
Figure 4-4: Transect of the AOD product of iCor over Lake Geneva region for the S2 acquisition of June 24, 2016.	68
Figure 4-5: $\rho_w(\lambda)$ for Lake Geneva at S2 bands 1 to 6 for the four ACs: namely, Acolite (blue), Polymer (orange), c2rcc (green) and iCor (red) against in-situ $\rho_w(\lambda)$ (black. Each panel correspond to a different S2 scene. In the legend is given the rmse and θ in parenthesis for each AC against in-situ measurements. The quantity of TSM and Chl from water sampling is indicated on each panel.....	71
Figure 4-6: θ (left) and rmse (θ) for each bands of S2 considered in the analysis. The scene from September 22, 2016 was discarded in order to remove the impact of high altitude clouds of the retrieval accuracy.....	72
Figure 4-7: Total scattering retrieved from c2rcc AC procedure. The inlets correspond to the total scattering (right) and the relative contribution by white scatterer (left) along a transect (red line). The southern part of the arrow correspond to the zero on the x-axis. On the white scatterer plot, the y-axis ranges between 0 and 0.175 m^{-1} , and it ranges between 0 and 6 m^{-1} on the total scattering plot. 73	
Figure 4-8: Profile plot of the backscattering coefficient retrieved by Polymer on the S2 acquisition from June 24, 2016 (right inlet) and from June 19, 2017 (left inlet). The right profile correspond to the transect represented by the red line, and the left profile to the red line in Figure 4-7. Increasing values in the x-axis correspond the east-west direction for obvious logical reason. Environmental factors.....	74
Figure 4-9: Scatter plot of ρ_w at S2 band 3 (560 nm) for the acquisition on June 24, 2016 of c2rcc versus polymer (left) and c2rcc versus iCor (right).	75
Figure 4-10: Second component of the PCA analysis of S2 band 3 (560 nm) from all atmospheric corrections applied to the acquisition from June, 24 2016. 75	

Figure 4-11: $\rho_w(\lambda)$ for Lake Geneva at S2 bands 1 to 6 for the four AC: namely, Acolite (blue), Polymer (orange), c2rcc (green) and iCor (red) against in-situ $\rho_w(\lambda)$ (black). Each panel correspond to a different S2 scene. In the legend is given the rmse and θ in parenthesis for each AC against in-situ measurements. 77

List of Tables

Table 3-1: In-situ campaigns conducted in Lake Geneva.....	41
Table 3-2: Water constituents parameters used in the optical closure. Note: CHL and TSM are near-surface measurements, while a long-term average is used as initial guess for a_{CDOM}	46
Table 3-3: Median and maximum spectral angles between INT and individual approximation models over all simulations.	52
Table 4-1: AOD statistics from MODIS observations over the Lemman region, and station number sampled for six Sentinel-2 observations in Lake Geneva. All water sampling was performed the same day of the overpass, except for the acquisition on June 19, 2017 when the sampling was performed on June 22, 2017.....	61
Table 4-2: Description of the methods tested for the estimation of ϵ in Acolite.	65
Table 4-3: Statistics of the performances of different procedure used in ACOLITE to retrieve the aerosol contribution. The median rmse designated by ' \diamond ' is partitioned into two spectral region: visible (VIS) and near-infrared (NIR). The VIS region encompasses the first 4 bands of S2 from 444 to 665 nm, and the NIR region refers to band 5 and 6 of S2 centered at 704 and 740 nm, respectively. The last column indicate the number of matchups with at least one negative value in the 6 bands considered.....	69
Table 4-4: In-situ matchup table in relatively dark to very dark waters in Finland.	76

Chapter 1

Introduction

1. 1. Inland water monitoring

Fresh water resource management is one of the biggest challenges of modern civilisations. Inland waters play a major role in social and economic development; they are vital for human health, agricultural production and fishery, transportation, and sanitation, and they are places of natural beauty and inspiration. However, freshwater habitats cover only ~3 % of the continental 'land' surface (Gleick, 1996) and these resources are facing unprecedented threat because of population growth, human activities and climate change (Allan et al., 2013; Halpern et al., 2008). In 2015, the World Health Organization (WHO) reported that at least 9 % of the total population still lack access to safe water resource. One of the most widespread environmental problems of inland waters is their eutrophication (UNEP, 2000). The principal cause of eutrophication is anthropogenic enrichment of water with two essential nutrients, nitrogen and phosphorous, which promote the growth of algae, bacteria, and other micro-organism. These two nutrients are introduced into drainage systems via agricultural fertilisers and industrial waste waters. Eutrophication leads to harmful algal blooms, oxygen depletion in the hypolimnion, deterioration of the recreational value, and alteration of fishery activities. To confront these challenges, the Water Framework Directive (WFD - 2000/60/EC) was adopted by the European Union member states in order to preserve, restore and monitor freshwater systems. Outside the European Union, most countries have adopted their own national water protection measures, but they differ widely in detail, strictness and implementation. In Switzerland, even though the WFD is not adopted, there is a long tradition of water quality monitoring with a vast network and routine collaborations in transboundary waters. In this context, it appears critical to dispose of robust and accurate methods for monitoring inland water quality and functioning at both regional and global scales.

1. 2. Remote sensing of inland water

Spaceborne observations provide a powerful complementary source of data for monitoring and understanding the physical, chemical and biological processes in inland waters at various spatial scales. The traditional point sampling approach adopted for water quality assessment is limited in terms of both temporal and spatial scales (Bierman et al., 2011). In this regard, remote sensing is a valuable alternative to overcome these limitations. Hydrodynamic and bio-geochemical models can further benefit from remote observations for validation and calibration through data assimilation (Brando et al., 2007; Pahlevan et al., 2012). A number of regional and local studies have demonstrated the capability of optical remote sensing techniques to assess a variety of applications, such as the quantification of primary production (e.g. Gitelson et al., 1993; Gons et al., 2008; Tyler et al., 2006), total suspended matter (e.g. Miller et al., 2004; Nechad et al., 2010) and detection of harmful algal blooms

(e.g. Jupp et al., 1994; Kutser et al., 2009; Simis et al., 2005; Wang et al., 2016). Moreover, its application has been extended to process-oriented studies such as the role of inland waters in the carbon cycle (Kutser et al., 2015) or the response of coral reefs to climate change (Andrefouët and Riegl, 2004; Hedley et al., 2016; Hochberg et al., 2003). For many years, the lack of appropriate sensors with sufficient temporal coverage or spatial resolution hindered the development of remote sensing in aquatic research (Mouw et al., 2015). Nevertheless, recent improvements, such as the launch of two satellite sensors, namely, Sentinel-2 and Sentinel-3, by the European Space Agency (ESA), open exciting perspectives. Indeed, recent studies have already demonstrated the suitability of Sentinel-2 for mapping lake water quality parameters (Pahlevan et al., 2017; Toming et al., 2016), and they discussed promising improvements associated with new wavebands (Hieronymi, 2016) for atmospheric corrections (Vanhellemont and Ruddick, 2015, 2016) and the quantification of dissolved organic compounds (Kutser et al., 2016). However, because of the singularity of inland waters, a thorough understanding of the relations between remote observations and in-water constituents is a prerequisite for the integration of remote sensing in water quality monitoring (Palmer et al., 2015). In this sense, validation exercises need to be extended and coordinated. For instance, each lake can be considered as a unique entity with a mixture of constituents of its own (Forel, 1892) and there is currently no widely accepted consensus, as for the inversion algorithm to be used for such complex waters. A workable approach is to adopt a water-specific approach (Moore et al., 2014; Spyarakos et al., 2017). Finally, environmental managers are often unfamiliar with remote-sensing solutions, and further collaborations between the scientific community and the decision makers will enhance the visibility of such approach (Schaeffer et al., 2013).

1.2.1. Optical properties of natural waters

The great variability of constituent compositions in natural waters translates to a great variety of optical properties in remote sensing of aquatic systems. The bulk optical properties are commonly divided in two groups (Preisendorfer, 1961): the inherent optical properties (IOPs) and the apparent optical properties (AOPs). The IOPs depend only on the medium and are independent of the ambient light field within the medium. The AOPs depend both on the medium and on the light field, and they display enough regular features and stability to be useful descriptors of a water body (Mobley, 1994). The radiative transfer theory provides the connections between these two groups and allows a mathematical formulation of the photon interactions in the water body and at the surface, as well as the illumination conditions and geometry of observations. For optical remote sensing, the low energies involved with visible light allow us to considerably simplify the radiative transfer theory to linear interactions of light with the medium. In this section, I discuss the theoretical basis implied by the

interpretation of remote observations tailored by the need to introduce the reader to the discipline. For a thorough introduction to the interactions of light in water and across the air-water interface, I refer to the first three chapters of the book by Mobley (1994) entitled: ‘Light and water’.

Inherent optical properties (IOPs)

The two most basic IOPs of water constituents are the absorption coefficient ($a(\lambda)$, in m^{-1}) and the volume scattering function $\beta(\theta)$ ($\text{m}^{-1} \text{sr}^{-1}$). Absorption depends on wavelength but is geometrically straightforward because affected photons are simply removed. Scattering has a weak dependence on wavelength, but it redirects a photon off the path with a complex angular distribution. We further differentiate two types of scattering to $\beta(\theta)$: (i) elastic scattering with properties similar to any object thrown at a surface and (ii) inelastic scattering associated with a change in wavelength and optionally a change in direction. Over the years, a number of instruments have been developed in order to measure $\beta(\theta)$ in-situ (Tyler, 1961; Petzold, 1972; Jerlov, 1961; Lee and Lewis, 2003), but their limited availability and their measurement complexity have considerably limited their application. The integral of β between 0 and π radians is called the scattering coefficient ($b(\lambda)$, m^{-1}), and it is defined as:

$$b(\lambda) = 2\pi \int_0^\pi \sin(\theta) \beta(\theta) d\theta \quad (1-1)$$

Likewise, the backscattering coefficient $b_b(\lambda)$ (m^{-1}) is the integral of β in the backward direction from $\pi/2$ to π , defined as:

$$b_b(\lambda) = 2\pi \int_{\pi/2}^\pi \sin(\theta) \beta(\theta) d\theta \quad (1-2)$$

Scattering is often described by the phase function ($\tilde{\beta} = \beta/b$), which specifies the angular dependence of the scattering without regard to its magnitude. Many different phase functions have been used in radiative transfer modelling of natural waters. The most widely used, calculated from in-situ measurements, is the Petzold (1972) phase function, which gives a backscatter fraction (b/b_b) of 0.183. Although this function gives satisfactory results for average situations, it can cause large errors when modelling a specific water body. Fournier and Forand (1994) derived an approximate analytic form of the phase function based on the Mie theory. The advantage of this phase function is the ability to generate a realistic shape with any desired backscatter fraction (Mobley et al., 2002).

In practice, researchers typically make scattering measurements ($b(\lambda)$, m^{-1}) at a single or a few angles to estimate the backscattering coefficient ($b_b(\lambda)$, m^{-1}). Several studies have shown that measuring $\beta(\theta)$ at an angle around 120° is optimal for the estimation of $b_b(\lambda)$ (Oishi, 1990; Boss and Pegau, 2001; Berthon et al., 2007). However, several constraints still require considerations: (i) The modelling of

$\beta(\theta)$ involves the Mie theory, which assumes a homogeneous, spherical particle population that may not be representative of particle shapes in natural waters (Ulloa et al., 1994; Babin et al., 2003; Reynolds et al., 2010); (ii) the $\beta(\theta)$ measurements used in the analyses were made in limited oceanic regions, and the variability for natural waters needs to be better quantified (Boss and Pegau, 2001).

Finally, note that the sum of absorption and scattering is called the beam attenuation (c).

Apparent optical properties (AOPs)

AOPs are the quantity that can be estimated through direct measurements of the radiant energy by the remote sensor. However, unlike the quantities directly measured, and as previously mentioned, they must be sufficiently stable to be useful descriptors of a water body. To understand this condition we can take the example formulated by Mobley (1994) in *Light and Water* about the downwelling irradiance $E_d(z, \lambda)$ ($\text{W m}^{-2} \text{nm}^{-1}$) propagating through the water column. Remember that irradiance is defined as the hemispherical integral of a radiant flux incident on a surface area from a given direction, whereas the radiance is defined as its conical integral over a solid angle. The modification of $E_d(z, \lambda)$ at a specific depth z will, in fact, depend on the medium, but does not satisfy the stability condition, because a cloud passing in front of the sun or a wind gust changing the sea surface roughness will cause an abrupt change of the magnitude of E_d . However, the ratio between E_d and the upwelling irradiance $E_u(z, \lambda)$ ($\text{W m}^{-2} \text{nm}^{-1}$) is almost insensitive to environmental factors such as the sea state or the overcast condition. This dimensionless ratio, called the irradiance reflectance $R(z, \lambda)$, is defined at a depth z as:

$$R(z, \lambda) = \frac{E_u(z, \lambda)}{E_d(z, \lambda)} \quad (1-3)$$

Another important metric used throughout this thesis is the remote-sensing reflectance $R_{rs}(\lambda)$ (sr^{-1}) just above the water surface, defined as:

$$R_{rs}(\lambda) = \frac{L_w(z=a, \lambda)}{E_d(z=a, \lambda)} \quad (1-4)$$

where $z = a$ indicates that the quantity is evaluated in-air, just above the air–water interface. The term L_w stands for the water-leaving radiance in $\text{W m}^{-2} \text{nm}^{-1} \text{sr}^{-1}$, which is the quantity that bears information on the water constituents and that is measured by a remote sensor along with the atmospheric contribution and the surface effects. The radiance is the conical integral counterpart of the irradiance. In-air $R(z = a, \lambda)$ is the bi-hemispherical integral of $R_{rs}(\lambda)$ and can be related to each other by a simple factor of π when assuming a Lambertian surface.

Two important AOPs are the diffuse attenuation coefficient of $E_d(z, \lambda)$ and $E_u(z, \lambda)$ between two depths K_d and K_u (m^{-1}), respectively, which is directly connected to the euphotic depth. In radiative transfer, it is used as a depth weighting function. A first formulation of this function was proposed by Gordon and Clark (1980):

$$f(z) = \exp\left[-\int_0^z 2K_d(z')dz'\right] \quad (1-5)$$

In order to take into account vertical non-uniformities, Zaneveld et al. (2005) proposed a different approach which depends on the round trip attenuation of the signal $\tau_g(z)$, defined as:

$$\tau_g(z) = \int_0^z [K_u(z') + K_d(z')]dz' \quad (1-6)$$

Figure 1-1 shows the behaviour of both functions when there is a concentration of optically significant constituents between 6 and 14 m.

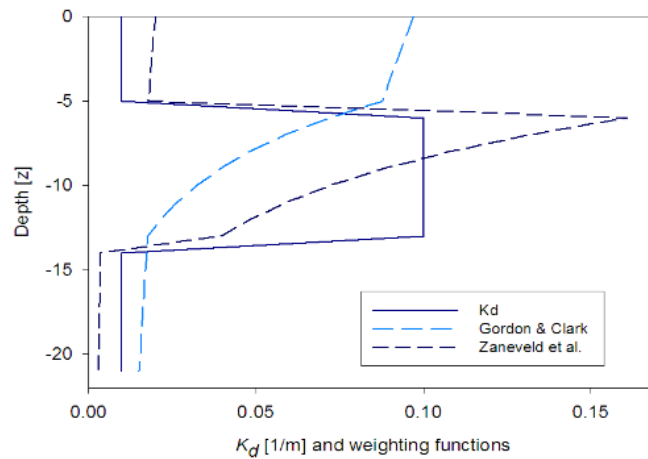


Figure 1-1: Illustration of the depth weighting function from Gordon and Clark (dashed light blue line), Zaneveld et al. (dashed dark blue line) and actual K_d profile (blue line). Source: Piskozub, 2008.

Optically significant water constituents

The principal optically significant water constituents are commonly arranged as follows:

- **Pure water:** The blue colour of clear lake water is a consequence of the absorption spectra of pure water given in Figure 1-2 (left panel), which increases exponentially in the visible domain.
- **Phytoplankton:** This category includes the majority of aquatic organisms involved in the photosynthesis. They are the most abundant primary producers in natural waters and have an

important effect on the food web structure of aquatic systems with a direct impact on the carbon cycle (Tranvik et al., 2009). In theory, any pigment with a significant contribution to the bulk absorption can be studied from remote observations, especially with the development of hyperspectral systems in recent years (Cubero-Castan et al., 2015; Wang et al., 2016). In practice, the most common and the most abundant bio-marker for phytoplankton is Chlorophyll-a (Chl) (Figure 1-2), but Phycocyanin, which characterises natural waters rich in cyanobacteria (Kutser et al., 2009; Simis et al., 2007), has also been used. The scattering properties of phytoplankton are also a challenge to account for the great variability of their size, shape, and composition (Babin et al., 2003; Matthews and Bernard, 2013).

- Coloured (or chromophoric) dissolved organic matter (CDOM): These compounds originate mainly from decomposing plants and consist mostly of humic and fulvic acids. High concentrations of CDOM result in yellowish brown to dark and almost black water bodies with an absorption spectra almost antagonist to pure water (Figure 1-2). CDOM is conveniently considered non-scattering (Dall'Olmo et al., 2009). When filtering a water sample, everything that passes the 0.2 μm filter is included in this category. Note that the pore size may vary between authors.
- Non-phytoplankton organic particles (or tripton or detritus): They are produced when phytoplankton dies (senescent cells) and include the fecal matters produced by zooplankton.
- Inorganic particles: They generally consist of quartz sand, clay minerals or metal oxides in various sizes from less than one μm to several tens of μm (Mobley, 1994).
- Air bubbles: Usually generated by breaking waves for significant wind speed. They mainly affect in-situ measurements, and contaminated records are excluded in the processing.

Note that phytoplankton, tripton and inorganic particles are grouped into total suspended matter (TSM). In a similar manner, inorganic particles and tripton are grouped into non-algal particles (NAP). The definition of the principal optically significant water constituents allows us to partition the bulk absorption (a) at each wavelength λ into its contributor as:

$$a(\lambda) = a_w(\lambda) + a_{phy}(\lambda) + a_{NAP}(\lambda) + a_{CDOM}(\lambda) \quad (1-7)$$

where $a_w(\lambda)$ is the absorption by pure water, $a_{phy}(\lambda)$ is the absorption by phytoplankton and $a_{NAP}(\lambda)$ is the absorption by NAP. The term $a_{CDOM}(\lambda)$, as the name suggests, is the absorption by CDOM.

In a similar manner, scattering $b(\lambda)$ can be partitioned as:

$$b(\lambda) = b_w(\lambda) + b_{phy}(\lambda) + b_{NAP}(\lambda) \quad (1-8)$$

The mass-specific representations of the IOPs are called the specific IOPs (SIOPs) per unit of constituents and are usually derived using bulk IOPs and concentration measurements of the water constituents of interest. The relation between water constituents, IOPs and SIOPs is described by bio-optical models, for which examples are provided in Chapter 3.

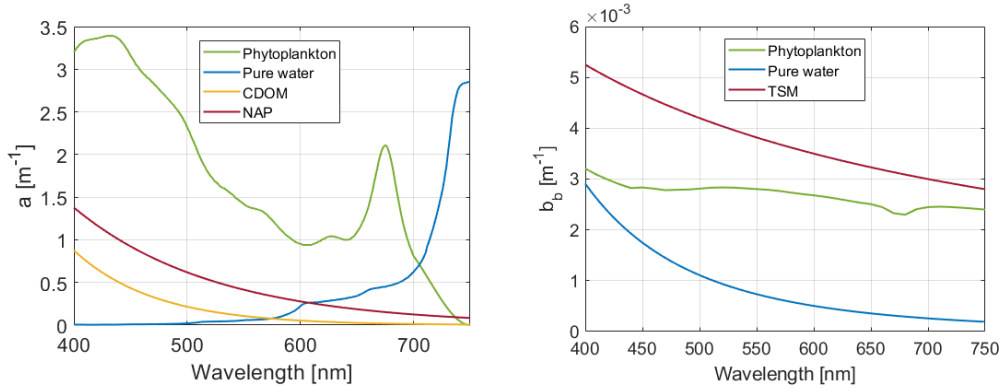


Figure 1-2: Left panel: absorption spectra of pure water (blue), NAP (red), CDOM (yellow), and phytoplankton (green). Right panel: scattering from pure water (blue), phytoplankton (green) and TSM (red). All data were taken from WASI-2D (Gege, 2014) except for the backscattering of phytoplankton taken from IOCCG report 5 (2006).

1.2.2. Radiative transfer theory

The radiative transfer theory is an analytical description of the paths of an incident radiance flux through a volume. All interactions are summarised in a single equation, which, in its standard form, relates the variation of radiance to beam attenuation, scattering distribution (elastic and inelastic components) and the source of radiant energy (e.g. bioluminescent organism). Therefore, models based on the radiative transfer equations (RTE) are also called forward models as they allow determining the expected radiant fields from the IOPs of water. The radiative transfer model that we will use throughout the study is Hydrolight model v5.3 (Mobley and Sundman, 2016).

1.2.3. Atmospheric contribution

At-sensor radiance measured by spaceborne sensors is mostly dominated by atmospheric signals over water (IOCCG, 2010), which need to be corrected. Figure 1-3 illustrates the typical light paths to the sensor in natural waters. The top of atmosphere (TOA) radiance (L_{toa} in $\text{W m}^{-2} \text{nm}^{-1} \text{sr}^{-1}$) measured by a satellite has three principal sources: (i) scattering of sunlight through the atmosphere toward the sensor (L_{atm} in Figure 1-3), (ii) reflection of sunlight by the sea surface (L_{surf} in Figure 1-3) and (iii)

the light exiting the water body (L_w in Figure 1-3). The path radiance referred to in Chapter 4 includes both the atmospheric and surface effects.

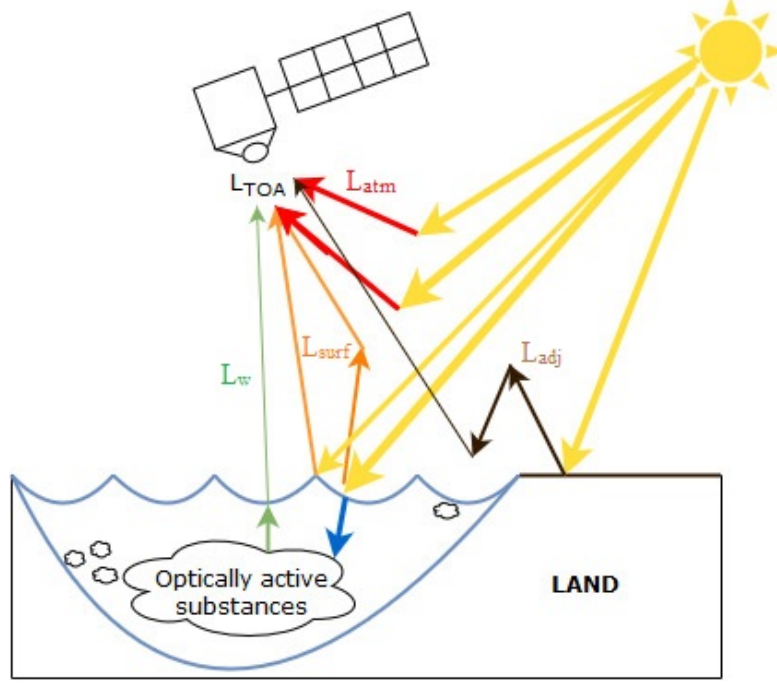


Figure 1-3: Schematics of the light paths for a sensor observing natural waters.

L_{toa} can be further partitioned into its contributors as (IOCCG, 2010):

$$L_{toa}(\lambda) = L_r(\lambda) + L_a(\lambda) + L_{ra}(\lambda) + t(\lambda)L_{wc}(\lambda) + T(\lambda)L_g(\lambda) + t(\lambda)t_o(\lambda)\cos\theta_0 L_w \quad (1-9)$$

where $L_r(\lambda)$ is related to Rayleigh scattering in the absence of aerosols by air molecules. This component is usually associated to ozone in the atmosphere and is well described by the Rayleigh mathematical model. $L_a(\lambda)$ is the aerosol contribution as if aerosols were the only component of the atmosphere. It is often coupled with $L_{ra}(\lambda)$, the multiple scattering between aerosols and air molecules. This coupled term is critical for the correction of atmospheric contribution and is responsible for the majority of the error in this procedure (Doerffer and Fischer, 1994). $L_{wc}(\lambda)$ denotes the contribution from white caps, and L_g is the specular reflection of direct sunlight at the air–water interface. $L_w(\lambda)$ is the quantity that is being retrieved by the atmospheric correction procedure, which contains information on the water column, namely, the normalised water-leaving radiance. $T(\lambda)$ stands for the direct transmittance from the surface to the sensor, and $t(\lambda)$ and $t_o(\lambda)$ stand for the diffuse transmittance of the atmosphere from the surface to the sensor and vice versa, respectively. Note that equation (1-9) does not include the adjacency effect, which is usually corrected in a separate procedure or not

corrected at all because it only affects the shores of a lake and the oceanic coastlines (Santer, 2000). The adjacency effect is a typical issue for remote sensing of inland waters because of their geographical situation. It describes the portion of photons reaching the sensor but coming from the reflection of the sunlight on the surrounding lands and scattered through the atmosphere towards the sensor (L_{adj} in Figure 1-3).

Atmospheric correction over inland waters is particularly complex because of (i) the influence of anthropogenic aerosol sources (Gordon, 1997), (ii) the large range of the IOPs of these waters and (iii) the contamination of the signal by surrounding land. In fact, the black pixel assumption in the NIR used for open ocean correction is not valid for turbid lake waters (Hu et al., 2000) and/or for waters with Chl concentrations larger than $2 \mu\text{g L}^{-1}$ (Siegel et al., 2000).

1. 3. Research objectives

1.3.1. Scope

The launch of a new constellation of satellite sensors with complementary spatial, spectral and temporal resolutions marks a new era in remote sensing of inland waters. With almost daily coverage of any water body around the world at a spatial resolution ranging from 300 to 30 m with bands relevant for the observation of water bodies, the possibilities of investigating our environment are now enormous. However, this source of information is still not integrated into the classical analysis framework from scientists and stakeholders. The aim of this work is to build the local and regional foundations to further incorporate remote-sensing data as key information for understanding lakes as dynamic systems.

The potential of integrating remote sensing data is first demonstrated in Chapter 2, showing an original application to monitor a rare calcite precipitation event in Lake Geneva. The core of this study was the combination of multiple satellite sensors with hydrodynamic modelling and chemical analysis, to identify and monitor a complex process in lakes that is not yet fully understood. Specifically, we demonstrate that combining complementary sources of information from inter-disciplinary research allows a thorough description of lake processes. The mechanism of the Rhône River intrusion in Lake Geneva bringing cold waters loaded with glacier particles further introduces an often neglected concept in remote sensing: the stratification and vertical differentiation of the water constituents in the water column.

The quality of remote-sensing products in oligo- to mesotrophic lakes is hampered by the lack of information regarding the vertical structure of the optical constituents. This research gap was the topic

of Chapter 3 entitled ‘Effects of non-uniform vertical constituent profiles on remote-sensing reflectance of oligo- to mesotrophic lakes’. Finally, in Chapter 4, we provide an evaluation of state-of-the-art atmospheric correction methods for inland water monitoring. To date, only one study was published for Sentinel-2 observations over Amazon flood plains (Martins, 2017). In Chapter 4, we extend these results to the peri-alpine region using in-situ measurements in Lake Geneva.

1.3.2. Questions

In this thesis we address the challenges related to the recent launch of remote sensors adapted to the monitoring of inland water. Specifically we address the following questions:

- (i) How can remote sensing be further integrated into interdisciplinary lake studies?
- (ii) How can additional informations provided by hydrodynamic models and biogeochemical analysis, be integrated to the interpretation of remote sensing observations?
- (iii) How does vertical non-uniform constituents profiles affect the remote sensing reflectance measured in oligo- to mesotrophic lakes?
- (iv) What is the effect of vertical non-uniform constituents profile on inversion algorithm?
- (v) What is the most suited atmospheric correction for Sentinel-2 over clear and dark inland waters?

To answer these questions we used spaceborne observations from multiple sensors combined with bio-physico-chemical measurements and in-situ optical measurements at key stations in Lake Geneva and the watershed.

1. 4. Structure of the dissertation

The scientific motivation of the thesis is a novel approach for lake water studies developed by the APHYS laboratory. The approach consists in a three-way integration of in-situ measurements, hydrodynamic models, and remote sensing observations to foster the understanding of inland waters processes. Therefore, in the second chapter we demonstrate the complementarity of each ends to monitor a rare calcite precipitation event. In Chapter 3, we propose a two-way integration between in-situ measurements and remote sensing which is being implemented for the systematic processing of Sentinel-2 observations over Lake Geneva. The fourth Chapter presents the preliminary results of ongoing research related to the recent availability of atmospheric corrections methods, which are presumably adapted for inland water monitoring. The final Chapter summarize the findings of the thesis and discuss the future development.

Chapter 2

Resolving biogeochemical processes in lakes using remote sensing

Vincent Nouchi¹, Tiit Kutser², Alfred Wüest^{1,3}, Beat Müller³, Daniel Odermatt⁴, and Damien Bouffard³

¹*Physics of Aquatic Systems Laboratory, Margaretha Kamprad Chair, EPFL-ENAC-IEE-APHYS, CH-1015 Lausanne, Switzerland (vincent.nouchi@epfl.ch)*

²*Department of Remote Sensing and Marine Optics, Estonian Marine Institute University of Tartu, Mäealuse 14, 12618, Tallinn, Estonia*

³*Eawag, Swiss Federal Institute of Aquatic Science and Technology, Surface Waters – Research and Management, Seestrasse 79, CH-6047 Kastanienbaum, Switzerland*

⁴*Odermatt & Brockmann GmbH, Stampfenbachstrasse 57, CH-8006 Zürich, Switzerland*

This chapter will be submitted to Aquatic Science, it is currently cited as: Nouchi, V., Kutser, T., Wüest, A., Müller, B., Odermatt, D., and Bouffard, D, 2018. Resolving biogeochemical processes in lakes using remote sensing.

Abstract

Remote sensing helps foster our understanding of inland water processes allowing a synoptic view of water quality parameters. In the context of global monitoring of inland waters, we demonstrate the benefit of combining in-situ water analysis and remote sensing for investigating biogeochemical processes at a global scale. We take the example of four Landsat-8 scenes acquired by the OLI sensor and MODIS-Aqua imagery over Lake Geneva (France - Switzerland) from spring to early summer 2014. Remotely sensed data suggest a strong temporal and spatial variability during this period. We show that combining the complementary spatial, spectral and temporal resolutions of these sensors allows for a comprehensive characterization of estuarine, littoral and pelagic near-surface features. Moreover, by combining in-situ measurements, biogeochemical calculations and hydrodynamic model to the remote sensing data, we link these features to river intrusion and calcite precipitation processes. In addition, we propose a procedure to monitor whiting events, which regularly occur in late spring or early summer in lakes.

2. 1. Introduction

Lake remote sensing was hampered for many years by absence of appropriate satellite sensors (Palmer et al. 2015). Yet, land remote sensing sensors were used for inland water studies (Brezonik et al. 2005; Kallio et al. 2008; Kutser 2012), but their radiometric resolution remained a severe limitation especially for oligo- to mesotrophic water bodies. MERIS was among the first suitable sensor for investigating large lakes at 300 m resolution, but finished its operations in 2012. At the time, only MODIS could partially substitute the observational capabilities, yet, with a coarser spatial resolution and less spectral bands in the near-infrared part of the spectrum than MERIS, but with nearly daily revisit time. With a significantly better radiometric resolution than its precursors, Landsat-8 (launched in 2013) allowed for mapping water quality parameters (Kutser et al. 2016; Lee et al. 2016; Slonecker et al. 2016) yet at 16 days temporal resolution, and thus complementing MODIS' capabilities in the spatio-temporal domain. Since the launch of Sentinel-2A (2015) and 2B (2017), as well as Sentinel-3A (2016) there is medium (10 to 60 m) and low resolution (300 m) imagery available with improved spectral resolution and 5 and 2 days revisit intervals at higher latitudes and at the equator, respectively. The combined use of such high and medium resolution data sources is key to better resolving near surface aquatic processes in lakes at all temporal and spatial scales.

The attempt to provide a unique remote sensing algorithm performing well over the wide variety of inland water is very challenging, if possible. In 1892, Forel already described lakes as unique envi-

ronment: *“Every lake is a geographical individual well separated from its congeners, in which physical and biological facts develop as in a world apart, independently of any relation with other lakes”*. This diversity was taken into account in the recent C-GLOPS approach (Spyrakos et al. 2018) by clustering lakes into 13 different classes and applying different sets of algorithms for each of them. However, there are often multiple processes that may produce similar optical signature (IOCCG 2000). We illustrate this difficulty with two examples. First, the vertical structure of the optically active substances has significant impact on the remote sensing signal (Bouffard et al. 2018; Nouchi et al. submitted; Pitarch et al. 2014). It has been shown that vertical distribution of cyanobacteria, capable of moving in the water column, influences both the absolute values and the shape of the remote sensing signal (Kutser et al. 2008). Then, the high backscattering signal in a lake may result from elevated concentration of allochthonous particles brought to the lake by river inflows or autochthonous “whiting” (calcite precipitation) within the water column. Whiting typically occurs when calcium carbonate is oversaturated due to high pH and/or high calcium input (Wells and Illing 1964). The initiation of whiting requires impurities that act as nucleation cells for calcites which are often initiated by phytoplankton blooms (Obst et al. 2009) or river inflows (Spencer et al. 1985). It is quite common in peri-alpine lakes that river water, often rich in fine glacial particles from mountainous catchments, plunges to deeper layers within tens to a few hundred meters from the river mouth after entering a lake (Finger et al. 2006). Most of the time, river flows intrude into the thermocline where the density of the river water equilibrates with the lake water density (Råman Vinnå et al. 2017a). In spring or early summer, the thermocline can be relatively shallow and the lake clear enough to allow riverine suspended solids trapped in the thermocline region to be detected from satellite sensors. The problem of detecting river particles intruding into lakes becomes even more challenging as the flow is often trapped near the shore at shallow water depth. Therefore, parts of the signal detected by satellites may only reflect near-shore lake beds. As an example, it may be nearly impossible to separate sandy sediment in 1 m depth with clear water from water rich in mineral particles where transparency is 1 m, especially when multispectral sensors are used (Kutser et al. 2006).

While new methods are being developed to account for the lake variability (in between lakes but also spatially and temporally on a given lake), we show in this study that combining information sources is a very efficient way to interpret remote sensing signals for lake functioning. Lakes have been historically monitored with in-situ measurements and more recently with hydrodynamic and water quality models. Local and remotely sensed observations are typically used to calibrate and validate numerical models. Here, we show that in-situ and model data can be used, not only to validate remotely

sensed products but also to ultimately provide a system-based understanding of remotely sensed maps.

Lake Geneva is a particularly interesting waterbody from remote sensing perspective. Most of the year the surface water is clear. Phytoplankton blooms occur close to the surface in late spring (Anneville et al. 2002a; Kiefer et al. 2015) and progressively move into deeper waters during the productive season becoming undetectable by remote sensing except when basin-scale internal waves move the thermocline upward into the photic zone (Bouffard et al. 2018; Bouffard and Lemmin 2013). Phytoplankton growth-related whiting events are known to happen in parts of Lake Geneva (Plée et al. 2010). Whether they are initiated by phytoplankton blooms or suspended matter is however still unknown.

The duration of algal blooms, whiting and major inflows is such that these events are often missed by the conventional monitoring of the lake. Remote sensing can make a major contribution in understanding of these processes assuming it is possible to recognize the biogeochemical processes involved at medium and low resolution remote sensing imagery.

This study was triggered by a striking event of lake waters turning from clear blue to opaque turquoise in June 2014. This event received wide attention by the general public which frames its time of occurrence quite accurately. An article was published in local newspapers on June 18, 2014 (<https://www.lematin.ch/suisse/Pourquoi-les-eaux-du-Leman-sont-turquoises/story/13801189>) with the event itself starting probably one or two days earlier. We used low-resolution MODIS and medium-resolution Landsat-8 imagery in combination with in-situ data and hydrodynamic model to investigate this particular event.

2. 2. Study site and Methods

Lake Geneva is the largest lake in Western Europe divided between Switzerland and France (Figure 2-1). The Rhône is the main tributary of the lake accounting for 68 % of the total water inflow (Burkard 1984). Minor rivers are Venoge and Aubonne in the north flowing down from the Jura Mountains and the Dranse in the south originating in the Alps. The Rhône, transporting mineral-rich glacier water, is the main source of particulate material flushed into the lake. Its water is all year round colder than the surface lake water and plunges to deeper layers of the lake (thermocline or below) very close to the river mouth not allowing riverine particles to spread at the surface.

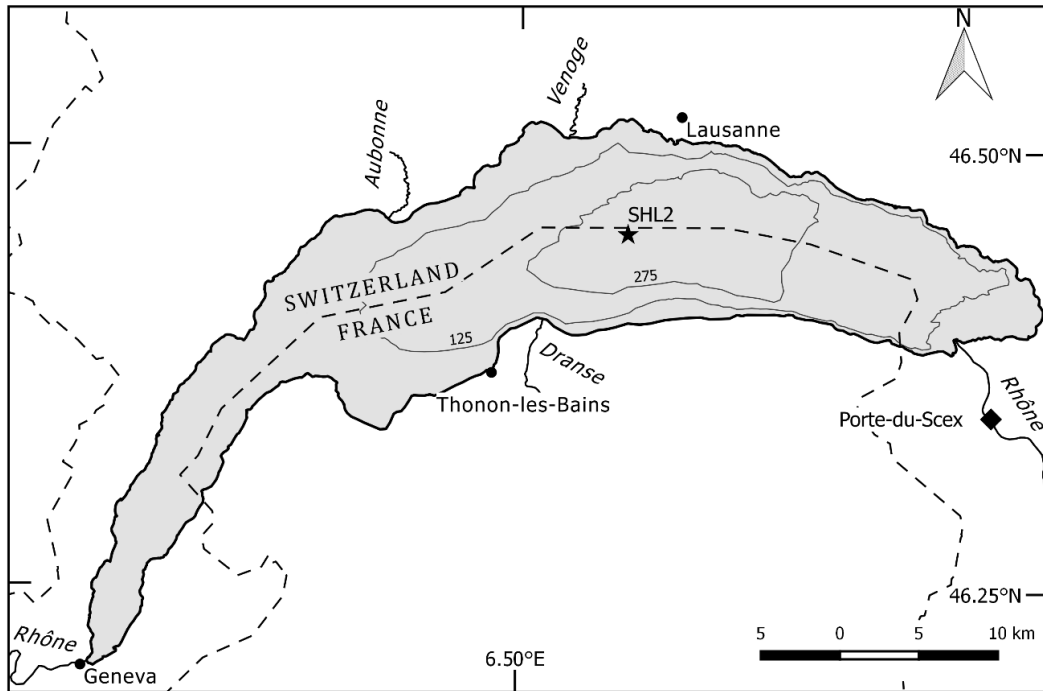


Figure 2-1: Overview map of Lake Geneva. The two sampling stations in the lake (SHL2) and in the Rhône (Porte-du-Scex, PS) are indicated.

The socio-economic and ecological impact of the lake on the region conciliated the French and Swiss Governments to sign a convention in 1963 to protect and preserve its waters. This convention, triggered by eutrophication of the lake, formalized the effort to continuously monitor the lake and its watershed at key stations and advanced measures to reduce the nutrient loads to the lake which initiated its slow recovery (Anneville et al. 2002a). In this study, we used bio-physico-chemical datasets from two stations: in Lake Geneva at SHL2 (Figure 2-1) and from the Rhône at Porte-du-Scex (PS, Figure 2-1). The lake monitoring data were provided by of the Commission Internationale pour la Protection des Eaux du Léman (CIPEL) which monitor the lake since 1957 at monthly to fortnightly intervals depending on seasons. In the river, PS data were provided by the Swiss Federal Office of the Environment (FOEN), measured at high frequency of 10 min.

2.2.1. Satellite data and processing

Modis-Aqua

Lake Geneva is covered by MODIS tile h18v4 with a spatial resolution of ~1 km for bands relevant for water observations. The MODIS-Aqua level 1A (raw radiances) from 1 to 30 June 2014 were obtained from the U.S NASA Goddard Space Flight Center (GSFC, <https://oceancolor.gsfc.nasa.gov>) and processed on the ESA Calvalus Earth observation data processing cluster. We used SeaDAS 12gen v7.4 to produce calibrated at-sensor radiance from L1A products. Further processing involved

the Case-2 Regional Coast Colour (C2RCC) applied using NCEP v0.18 auxiliary data for atmospheric correction and retrieval of inherent optical properties and water constituents. C2RCC is a neural network algorithm based on the approach by Doerffer and Schiller (2007) which allow the retrieval of the optically active components using a large database of radiative transfer simulations (Brockmann et al. 2016). In this study we used the chlorophyll-a (CHL) and the Total Suspended Matter products (TSM). CHL estimates with its predecessor C2R and MERIS data were successfully validated for Lake Geneva (Odermatt et al. 2010). In this study we used the CHL and the TSM products.

Landsat-8

There are two Landsat-8 orbits that cover most of Lake Geneva, i.e. the 28th row of both path number 195 and 196. It means that the imagery is available with double frequency compared to the 16 days revisit time. Landsat-8 imagery, showing high water leaving signal in some parts of the lake was available for June 8 and 15, 2014 during the prominent event in summer 2014. Cloud-free images before and after the event were available on May 23, and July 17, 2014. Atmospheric correction, for the estimation of the water-leaving reflectance (ρ_w , dimensionless), was performed using the SWIR correction of ACOLITE (Vanhellemont and Ruddick 2014, 2015, 2016) with fixed aerosol type ($\epsilon = 1$), and a smoothing window of 330 m. Regarding the input settings, the Level-1 radiance were adjusted using the spectral gains suggested by Pahlevan et al. (2014).

2.2.2. In-situ dataset

Physico-chemical measurements at station SHL2 used in this study are provided at 20 depth levels: 0; 2.5; 5; 7.5; 10; 15; 20; 25; 30; 35; 50; 100; 150; 200; 250; 275; 290; 300; 305 and 309 m. The sampling procedure is standardised by UMR CARTELE INRA at Thonon-les-Bains (Unité Mixte de Recherche entre l'INRA et l'Université de Savoie; Centre Alpin de Recherche sur les Réseaux Trophiques des Ecosystèmes Limniques). Analysis are validated using uncertainty maps and errors are provided. All water samples are analysed for CHL using the Strickland and Parsons (1968) method. Concentrations of calcium (Ca) are determined analytically by ion chromatography and alkalinity is measured by acid titration (0.01M HCl) to the inflection point. Lake water pH was measured immediately after sampling while the pH of the Rhône water at PS is available at 10 min intervals. Water sampling at PS was accomplished in the frame of the NADUF program (National Long-term Surveillance of Swiss Rivers, <http://www.eawag.ch/en/departement/wut/main-focus/chemistry-of-water-resources/naduf/>) where samples were collected proportional to water discharge. Water sampling at PS follow the same analytical procedure as CIPEL with additional measurements of TSM using gravimetric method. In parallel to water sampling, a transparency measure using a Secchi disk is performed

at SHL2 and multiparameter probes are used to provide measurements of temperature, conductivity, and turbidity within the entire water column (Blanc et al. 1993) and at a single depth in the river at PS. Sampling and analysis of Lake Geneva site SHL2 water is performed at a minimum of monthly intervals and we used data from April 7, June 2, and June 30, 2014 accessed through the Information System of the SOERE OLA-IS © (<http://si-ola.inra.fr>) on May 19, 2017. Discharge, pH, temperature and conductivity data were provided between 2011 and 2017 at 10 min intervals while TSM and Ca are provided at fortnightly intervals for the same time period (<https://www.bafu.admin.ch>).

2.2.3. River intrusion model

Whiting events share similar features as river plumes which also bring mineral particles into the lake. While both sources will consistently increase the general amplitude of R_{rs} in the whole spectral domain, calcite particles are more efficient scatterer (Balch et al. 1989; Bricaud and Morel 1986). In the following, we describe the mechanism of the river intrusion in order to comprehend its observability from a remote sensing perspective. Figure 2-2 illustrates the processes in Lake Geneva beyond the Rhône River inflow. It has been shown that the maximum distance from the shore to the plunging point of the river flow (Hauenstein and Dracos 1984) is about 100 ± 20 m quite independently of the Rhône inflow, as the river mouth topography is very steep (Sastre et al. 2010).

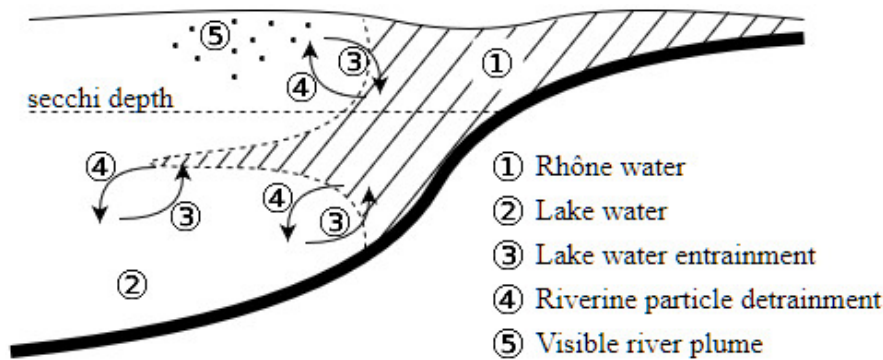


Figure 2-2: Sketch showing the main processes occurring during the intrusion of the Rhône waters (1) in the lake (2): entrainment of lake waters into the Rhône plume (3) and detrainment of particles from the Rhône water into the surface layer of the lake (4).

The maximum depth, where the river waters intrude into the lake waters depends on the density difference between the water masses. A small part of mineral particles can stay in the surface layer due to detrainment and the amount of such particles is larger when the density difference (depending mainly on temperature difference) is smaller (i.e. in winter and early spring). Therefore, seeing small amounts of river plumes in spring is realistic, but it is unlikely in summer. Yet, the intruded water can be at a shallower depth than the maximum depth of light penetration and thereby being detectable

by remote sensing sensors. Consequently, a first estimate of the river intrusion depth is needed to analyse the images from satellites.

The river intrusion depth was calculated according to the model previously developed for Lake Geneva and thoroughly described in Råman Vinnå et al. (2017b) from density difference calculation and lake water entrainment. To feed the river intrusion model, river and lake water density were calculated using the Chen and Millero (1986) formulas for temperature and salinity (measured via conductivity) and the density increment caused by the inorganic river particles at PS was added.

2.2.4. Hydrodynamic model

The Delft3D-FLOW hydrodynamic simulation program has been selected for this study. It is an open-source hydrodynamic modelling suite solving a coupled system of differential equations for momentum, heat, mass and salinity driven by atmospheric forcing. Delft3D-FLOW has been successfully applied to Lake Geneva (Bouffard et al. 2018).

In this study, the z-layers scheme is used since it is the only one able to reproduce the stratification with the given steep lake morphologies. The horizontal grid resolution was set to 500 m. A time-step of one minute is defined to maintain model stability with the κ - ϵ turbulence closure model. As initial conditions, the lake is initialized (uniformly horizontally) from an in-situ profile taken at the deepest point of the lake in January.

In terms of atmospheric forcing, MeteoSwiss COSMO2 reanalysis products, consisting of seven meteorological variables on a regular 2.2 km grid with an hourly resolution are used. Those variables include solar radiations, wind direction and intensity, relative humidity, cloud cover, pressure, and air temperature from their weather model tailored to the Alpine region with data assimilation.

2.2.5. Calculation of the calcite saturation index Ω

The concentration of the species $[Ca^{2+}]$ was calculated from the analytically determined concentrations of total Ca, $[Ca]_{tot}$, considering the dissolved Ca complexes given in equation (2-1):

$$[Ca^{2+}] = [Ca]_{tot} - ([CaOH^+] + [CaHCO_3^+] + [CaCO_3]_{aq}) \quad (2-1)$$

Concentrations of the components of the carbonate system (pCO_2 , $H_2CO_3^*$, HCO_3^- , CO_3^{2-}) were calculated from the measurements of alkalinity and pH as described in Stumm and Morgan (1996).

Chemical equilibrium constants applied were adjusted to the measured temperatures using the relationships suggested by Plummer and Busenberg (1982).

The saturation index Ω , for calcite was calculated as the ratio of the activity product of $\{Ca^{2+}\}$ and $\{CO_3^{2-}\}$ and the temperature-corrected solubility constant, K_{s0} :

$$\Omega = \frac{\{Ca^{2+}\}\{CO_3^{2-}\}}{K_{s0}} \quad (2-2)$$

Chemical activities were calculated with the Debye-Hückel approximation (Stumm and Morgan, 1996) and the ionic strength from the concentrations of major anions and cations which are available from the CIPEL monitoring at SHL2 (CIPEL, 2015).

2. 3. Results and discussion

Given the short temporal scale of the observed event, the first logical step in the attempt to understand the processes that took place in June 2014 is to screen the daily MODIS products for variations in CHL and TSM (Figure 2-3). As expected for the nutrient depletion phase after the spring bloom, CHL levels are relatively low at baseline concentrations around 1 mg m^{-3} , with short-term slightly elevated values of $2\text{-}3 \text{ mg m}^{-3}$ occurring on June 1 and 6. They are barely detected in the TSM products until June 8, when locally increased CHL levels in the western part of the lake are contrasted sharply by contrary variations in TSM, which is strongly increased on the eastern side. This striking evidence and the low productivity on previous days suggest that the detected particles in the east are inorganic. Furthermore, their presence either prevents algal growth or at least its detection by C2RCC. On the following days, the inorganic particle pattern varies in density and develops from the southern shore, while CHL remains low and increases only occasionally and in coincidence with the inorganic matter. After June 21, the lake is back to background concentrations of $1\text{-}2 \text{ mg m}^{-3}$ CHL and $1\text{-}2 \text{ g m}^{-3}$ TSM (Figure 2-3).

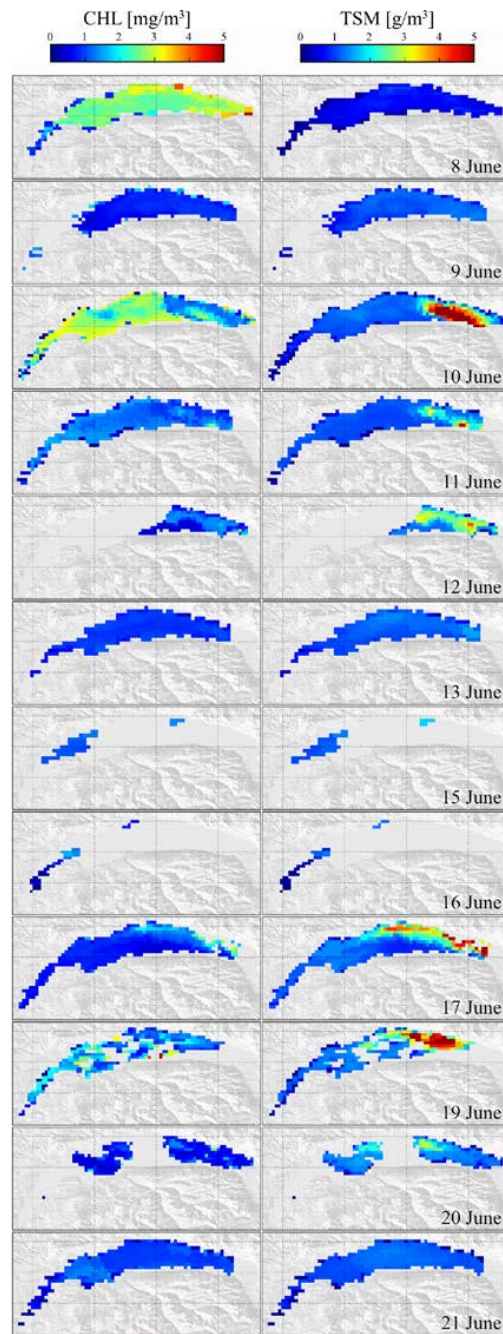


Figure 2-3: Distribution of CHL (left) and TSM (right) from June 8 to 21, 2014. Each row corresponds to a different date.

As the inorganic TSM pattern starts from the Rhône mouth and follows the general circulation pattern in the lake one may conclude that the high TSM in the lake and turquoise waters reported in the press were caused by a massive turbid water inflow. Local knowledge tells us however that the highly turbid Rhône waters cannot cause such large river plumes and in addition, massive blooms of cyano-

bacteria, coccolithophores or other highly scattering phytoplankton species do not occur in Lake Geneva (Anneville et al. 2002b). In the following we first interpret medium resolution Landsat-8 imagery, and gradually include additional information provided by hydrodynamic models and biogeochemical measurements.

Four Landsat-8 imagery are shown for the period May to July 2014 in Figure 2-4Figure 2-7. Insets of the imagery show zooms of the Rhône inflow area. The water was quite clear in most of the lake by end of May 2014 (Figure 2-4) with higher turbidity near the Rhône River, small river inlets and near the shores. The situation drastically changed in the beginning of June 2014 (Figure 2-5). There are two types of waters present that differ optically from the clear central part of the lake and have bright blue (P4 in Figure 2-5) and greenish appearances (P3 in Figure 2-5). In some parts of the lake, these two water masses are spatially separated whereas both water types are present along the north shore and near the Rhône inflow. However, in these regions spatial patterns of the water masses are slightly different indicating that these water masses were probably at different depths.

One week later the situation was strikingly different. Most of the June 15 image (Figure 2-6) is contaminated with Cirrus and partly Cumulus clouds as well as sun glint. Despite those disturbances, a large area with elevated reflectance is clearly present in the eastern part of the lake. On July 17 most of the lake is clear again (Figure 2-7). The signal is only elevated near the Rhône inflow. Close inspection showed that this signal stems partly from the turbidity plume and mostly from sun glint.

The insets in Figure 2-4Figure 2-7 allows to identify the plunge points defined as the location where the density-driven river water sinks to the thermocline and disappears from the surface. From Landsat-8 images we observe maximum distances that Rhône water inflows reach from the river mouth are $\sim 90 \pm 30$ m. A threefold increase in the discharge hardly changes the off-shore distance of the point, where the Rhône plunges to deeper layers. However, the 4 km long plume with elevated reflectance and the small plumes near the river inflows indicate that the condition were favourable for the detrainment of riverine particles close to the surface (Figure 2-4). This is typical for spring, when the difference between lake and river temperatures are relatively low (Lambert and Giovanoli 1988).



Figure 2-4: Landsat-8 image of Lake Geneva from May 23, 2014. The inset zoom (top right) shows the Rhône inflow area. Crosses indicate the pixels where water reflectance spectra shown in Figure 2-8 were collected.



Figure 2-5: Landsat-8 image of Lake Geneva from June 8, 2014. The inset zoom shows the Rhône inflow area. Crosses indicate the pixels where water reflectance spectra shown in Figure 2-8 were collected. Note that the image histogram was stretched to show the different hydrodynamic structures and colours.



Figure 2-6: Landsat-8 image of Lake Geneva from June 15, 2014. The inset zoom shows the Rhône inflow area. Crosses indicate the pixels where water reflectance spectra shown in Figure 2-8 were collected.



Figure 2-7: Landsat-8 image of Lake Geneva from July 17, 2014. The inset zoom shows the Rhône inflow area. Crosses indicate the pixels where water reflectance spectra shown in Figure 2-8 were collected. Note that most of the bright area next to the inflow is due to sun glint not due to water turbidity.

In order to go further from mechanistic analysis described in conjunction of Figure 2-3 we analysed water reflectance spectra from each image. Rhône waters are rich in mineral particles (median of 229 g m^{-3} between May 23 and July 17). Therefore, the pixels collected within the Rhône just before entering Lake Geneva have high reflectance. A turbidity plume with variable amount of suspended matter (and variable reflectance) is seen in the image of May 23 (Figure 2-4) at the easternmost end of the lake. A small plume is detectable also near River Dranse on that day.

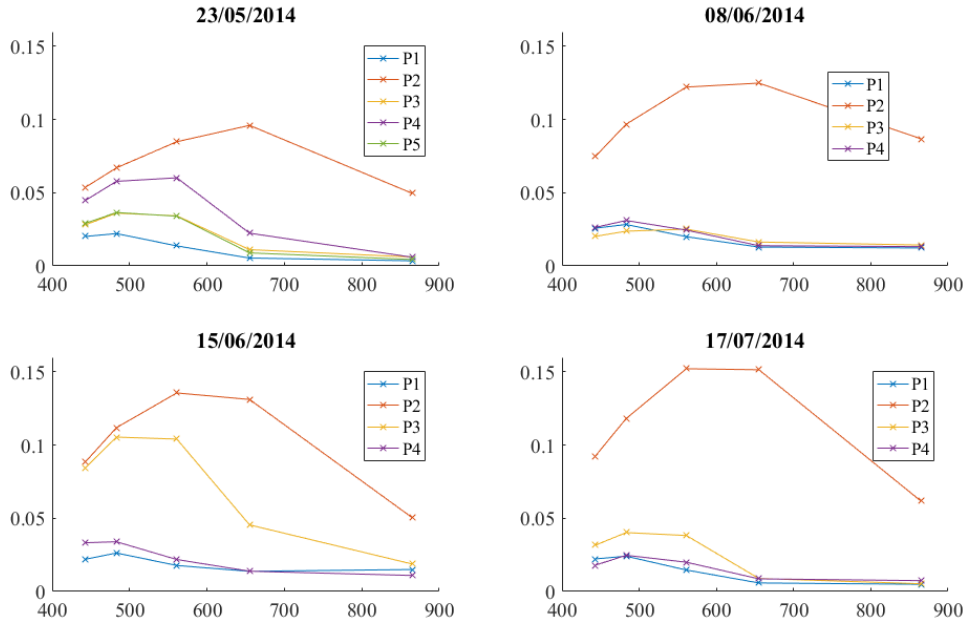


Figure 2-8: ρ_w collected from four Landsat-8 images. Exact locations of the extracted pixels are shown in Figure 2-4 to Figure 2-7.

Optically the situation is the most complex on the June 8 image (Figure 2-5). There are relatively clear water areas, and regions where the water looks whitish or greenish with variable shape of the reflectance spectra. Difference in the reflectance spectra collected in these three water masses are minimal in brightness (reflectance values, top right panel of Figure 2-8). The shape of the reflectance spectra from greenish water masses indicate that these are areas with elevated phytoplankton biomass as the water-leaving signal is absorbed at shorter wavelengths.

Spatial patterns of the greenish and whitish water masses do not co-vary in many places. This suggests that these two water masses are located at different depths. Indeed, the vertical profiles of CHL and turbidity measured a few days before (Figure 2-9) show that the algal biomass maximum is at ~2.5 m depth, whereas the turbidity maximum occurred at 7 m depth. We cannot identify reasons of the whitish water based on the reflectance spectra. The extent of such areas suggest that it was not riverine mineral particles from the Rhône or other smaller inflows and it was also not resuspension of particles in shallow nearshore areas that exist only in some parts of the lake as narrow stripes. Therefore, the initiation of a whiting event is the most probable cause.

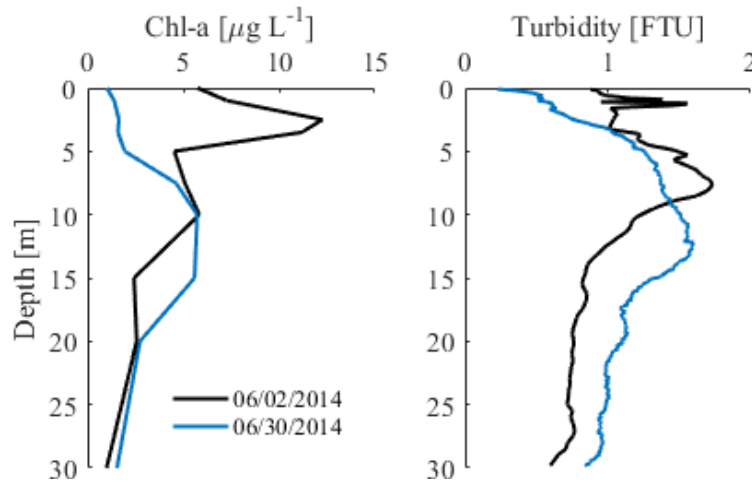


Figure 2-9: CIPEL CTD profiles at station SHL2 of CHL (left) and turbidity (right) for June 2 2014 (black) and June 30 2014 (blue).

Practically the whole Lake Geneva was covered with thin clouds or haze on June 15, 2014. Nevertheless, a large area with very high water reflectance is seen in the eastern half of the lake. The plume starts right from the Rhône inflow. The first assumption may be that there was a massive inflow event of mineral particles from the Rhône. Theoretically it is possible that the maximum intrusion depth is close to the water surface and satellites can detect the turbidity plume through clear top water layer. We simulated the depth distribution of river intrusion based on the physical conditions (temperature, conductivity and particle content). Figure 2-10 shows that in spring, when the temperature difference between lake and river water is small, the typical intrusion depth is between 5 m and 10 m. In June the intrusion occurred mostly between 15 and 20 m. Secchi depths in the middle of the lake at SHL2 in spring 2014 were in the range of 5.8 to 6.2 m. In June 2014, they varied between 5.7 m and 8.8 m at the same location meaning that the turbid water intrusion is too deep to be detected by remote sensing even if the top water layer is clear.

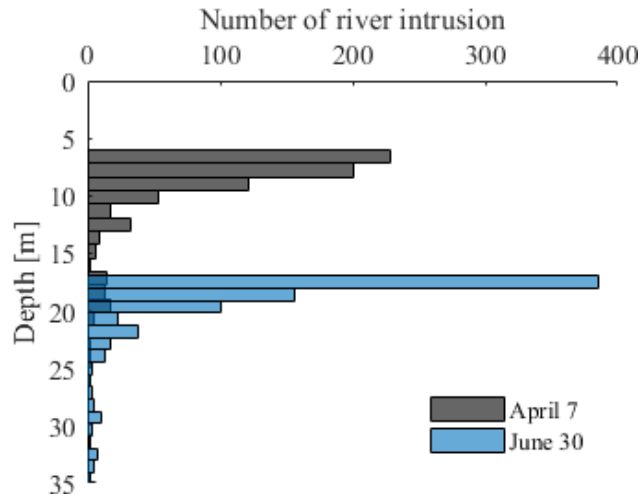


Figure 2-10: Histogram of the depth distribution of Rhône intrusions into Lake Geneva for early April 2014 (black) and for end of June 2014 (blue). River data have a time interval of 10 min and are taken over 5 days before the measurements at SHL2.

Due to particle detrainment, a Rhône River plume is still often visible at the surface (Figure 2-4 and Figure 2-7), although the river intrudes below the optical depth of the water. Using hydrodynamic model simulation we see that the spatial extent of the bright feature for June 15, 2014 correspond almost exactly to the path of particles coming from the Rhône River inlet area (Figure 2-11) and travelling within the thermocline (at ~15 m depth) within a week of the event. This suggest that the Rhône River input plays a major role in the process occurring around the north-eastern part of Lake Geneva and it allows us to comprehend its spatial extension.

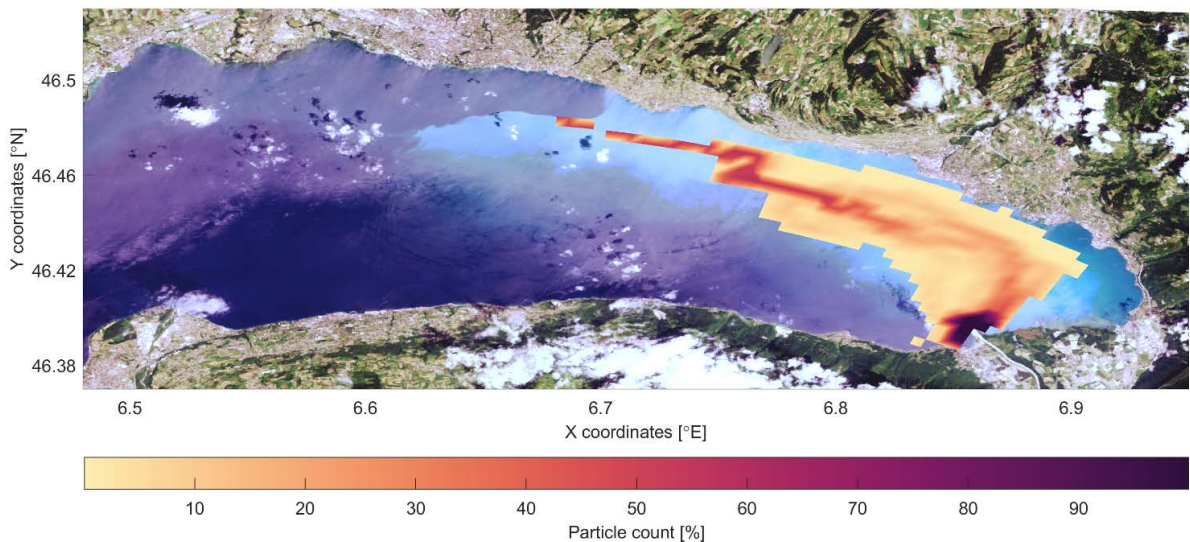


Figure 2-11: The background correspond to the Landsat-8 image of Lake Geneva from June 15, 2014 (Fig. 6). The overlaid surface plot represent the percent of particles originating from the

Rhône River inflow area, passing by an element of the grid of the hydrodynamic model. One particle was released around the Rhône River mouth (maximum spread of 500 m) every 10 minutes between June 8 and June 15 2014 and advected into the lake using the average velocity field between 1 and 15 m depth.

A milky blue coloration of water is theoretically possible also in the case of some phytoplankton blooms like the coccolithophore *Emiliania Huxleii*. However, these oceanic species do not occur in freshwater. There are freshwater phytoplankton species that scatter light effectively, like cyanobacteria, and can cause bright reflectance. However, high water reflectance from cyanobacterial blooms is associated also with elevated absorption at blue wavelengths (due to chlorophylls) making the water greenish. This was not observed in Lake Geneva. Thus, the only potential cause of this massive whitening of water is calcite precipitation. Therefore, we studied whether there were any changes in Ca concentration during the period of interest.

Measurements from the water column of Lake Geneva were available in 2014 from June 2 and 30, while the event occurred close to June 16. In the top 20 m, calcite was up to five-fold supersaturated on June 2 (Figure 2-12, left panel, eq. 2). Calcite supersaturation can persist up to very high values of Ω without precipitation occurring for various reasons, e.g. prevention of the growth of initial nuclei by sorption of phosphate (Lotter et al. 1997; Niessen and Sturm 1987), but can be initiated by the introduction of additional nucleation seeds. It is most likely that the high fine particle load of the Rhône provided such active particulate surfaces that initiated calcite precipitation, even though the river water itself was slightly below saturation with respect to calcite ($\Omega = 0.93$). The concentrations of Ca in the top 20 m of the water column decreased between June 2 and 30 (Figure 2-12, right panel **Erreur ! Source du renvoi introuvable.**), indicating the removal of calcite. Integration of the Ca removed from the top 20 m yields an event-specific areal precipitation of 44 g Ca m^{-2} (1.1 mol m^{-2}).

This amount of Ca precipitation for individual whiting event is quite realistic. In the last two decades, annual averages of Ca sedimentation in Lake Geneva were estimated to $\sim 140 \text{ g Ca m}^{-2} \text{ yr}^{-1}$ (Dominik et al. 1993) and $\sim 190 \text{ g Ca m}^{-2} \text{ yr}^{-1}$ (Graham et al. 2016), which covers a range consistent with Ca sedimentation of $\sim 170 \text{ g Ca m}^{-2} \text{ yr}^{-1}$ as determined for the two hard-water Lakes Lugano and Sempach (Ramisch et al. 1999). This comparison indicates that this individual whiting event was removing $\sim 1/4$ of an annual Ca deposition, which appears realistic in view that the Ca sedimentation was shown to scale with the organic matter production and sedimentation (Graham et al. 2016). This large amount of calcite precipitation also shows, that the net carbon removal into the sediment reaches several $10 \text{ g C m}^{-2} \text{ yr}^{-1}$, which is a major term in the carbon budget and exceeds the organic C deposition in those lakes (Loizeau et al. 2012; Schwefel et al. 2016).

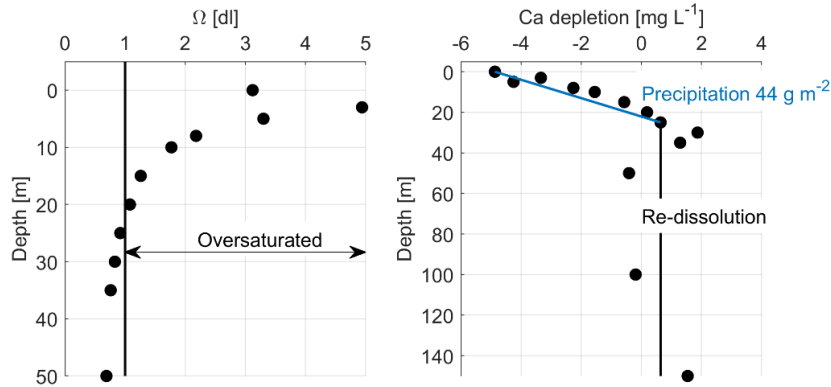


Figure 2-12: Ω at SHL2 for June 2 2014 (left), and Ca precipitation (right) estimated over the month of June 2014 plotted as the difference in the Ca concentration between June 30 and June 2. The Ca depletion is restricted to the top 20 m with the maximum right at the surface. The integrated Ca precipitation for this event was 44 g m^{-2} in the top 20 m.

The wide public attention to this whiting event suggests that something extraordinary may have happened in Lake Geneva in summer 2014. Actually, this was not the case. Monitoring data from 2011 to 2017 (Figure 2-13) shows that the 2014 summer was quite typical. It is seen also in Figure 2-9 that the phytoplankton dynamics was similar to what has been observed before (Nouchi et al. submitted). Similar decreases in Ca concentrations occurred also during previous years and were most probably associated to similar calcite precipitation events that colour water turquoise. Most probably the 2014 event got more attention because it occurred near shore and affected harbours and beaches while potential offshore whiting may not be recognised. The duration of the whiting events and frequency of monitoring makes it highly possible that the whiting events were missed also by conventional monitoring. Combining Sentinel-2A and 2B with Landsat-8 allows now to obtain lake imagery with a frequency that will reliably allow monitoring of blooms and whiting events.

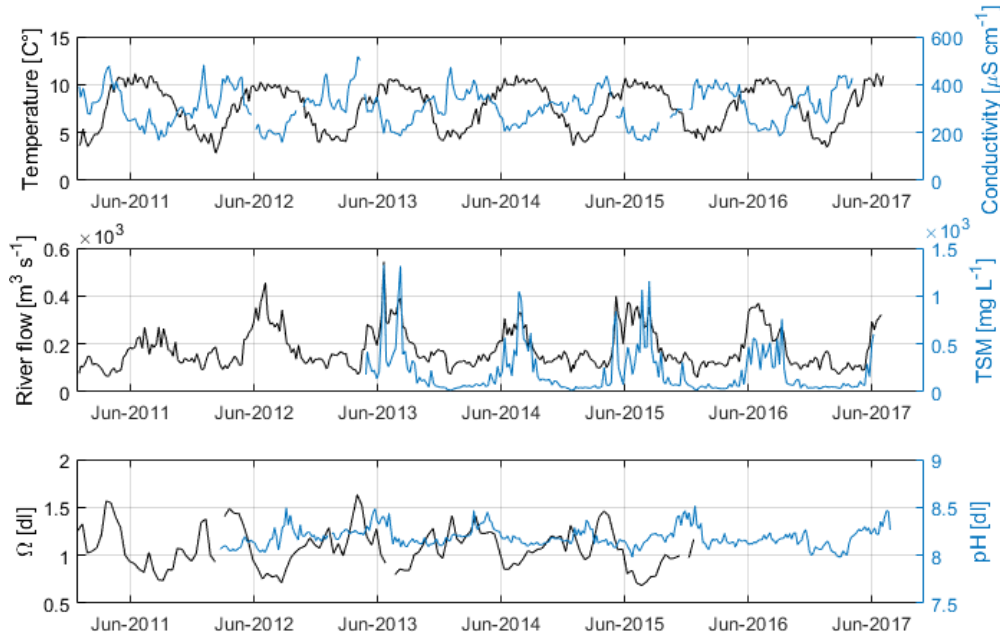


Figure 2-13: Rhône physico-chemical parameters at PS from 2011 to 2017.

2. 4. Conclusion

This study shows that remote sensing is a powerful tool to understand different simultaneously occurring processes in lakes. Remote sensing efficiently provides information regarding the spatial and temporal variability of processes. Specifically, we show that combining the spatial resolution of Landsat-8 and temporal coverage of MODIS can extend the information retrieved from remote observations. However, different processes (e.g. river plumes and calcite precipitation) may have spectrally similar signatures. In such cases, applying the same data analysis procedure may lead to erroneous interpretation of the remote sensing signals. Combining remote sensing data with additional local information (such as in-situ data, hydrodynamic and biogeochemical models, etc.) allows a much deeper understanding of processes which cannot be resolved based on remote sensing or monitoring alone.

We show that the observed whiting event was triggered by the Rhône River entering the lake and the signature of the event was mostly advected and further spread by the lake circulation. This study also indicates that whiting events may regularly occur in early summer on Lake Geneva. In the future, whiting, or any process related to the interaction between riverine and lake water, may be identified in spatial and temporal extensions much easier by applying the proposed procedure.

Acknowledgement: This work was supported by the Margaretha Kamprad Chair and by the Fondation pour l'Etude des Eaux du Léman (FEEL) on Lake Geneva. Finally, acknowledgements for

Carole Lebreton for her kind support with the configuration of the MODIS processing chain and for Brockmann Consult for operating and providing access to the Calvalus cluster computer system.

Chapter 3

Effects of non-uniform vertical constituent profiles on remote-sensing reflectance of oligo- to mesotrophic lakes

Vincent Nouchi¹, Daniel Odermatt², Alfred Wüest^{1,3}, Damien Bouffard^{1,3}

¹*Physics of Aquatic Systems Laboratory, Margaretha Kamprad Chair, EPFL-ENAC-IEE-APHYS, CH-1015 Lausanne, Switzerland*

²*Odermatt & Brockmann GmbH, Stampfenbachstrasse 57, CH-8006 Zürich, Switzerland*

³*Eawag, Swiss Federal Institute of Aquatic Science and Technology, Surface Waters – Research and Management, Seestrasse 79, CH-6047 Kastanienbaum, Switzerland*

This Chapter has been submitted to European Journal of Remote Sensing, and revision is undergoing, it is currently cited as: Nouchi, V., Odermatt, D., Wüest, A. and Bouffard, Eur. J. Remote Sens., reviewed, 2018.

Abstract

We investigate the impact on remote sensing reflectance by the vertical non-uniformities of water constituents, which are characteristic for oligo- to mesotrophic lakes. This often neglected feature is relevant for most clear systems when light penetration depth is significant. We demonstrate the need to take this phenomenon into account by analysing data from Lake Geneva because it is a representative case with diverse mixture of algal and inorganic particles and a large variability of profile shapes in the course of the seasons. Reflectance simulated for 210 pairs of in-situ measured chlorophyll-a and total suspended matter profiles ($z = 0 - 20$ m) are compared to simulations for uniform constituent gradients and non-uniform profiles approximated by Gaussian curves, orthogonal layers and steady gradients. We use the radiative transfer model Hydrolight and a generic, yet locally verified, set of specific inherent optical properties. Relevant concentration ranges are between 0 and 17 mg m^{-3} for chlorophyll-a and 0 and 4.6 g m^{-3} for total suspended matter within the photic layer. Our results show that mesotrophic lakes are specifically sensitive to non-uniformities with 20 % of the 210 samples used in this study showing deviations of the spectral angle $\theta > 5^\circ$ between a uniform assumption (homogeneous top 1 m) and observations which mostly occur for deeper-laying water constituents. By stressing the different use of blue and red parts of the spectrum, we argue further that algorithms are affected by variable vertical structures of algal and inorganic particles. Finally, we demonstrate that approximation models of the vertical structure of water constituents are a good solution to better account for non-uniformities in the development of invertible bio-optical models.

3. 1. Introduction

Passive optical water quality remote sensing provides spatially and temporally comprehensive observations of the photic surface layer in natural waters (Gordon and McCluney, 1975). The retrieval procedure is an ill-posed inverse problem and complementary information sources can significantly enhance the robustness and reliability of observational estimates. This was shown by comparing standard remote sensing products and in-situ measurements from autonomous underwater vehicles (Ryan et al., 2014), automated platforms (Odermatt et al., 2012), hydrodynamic model simulations (Curtarelli et al., 2015) or LIDAR measurements (Montes-Hugo et al., 2010). Provided that such additional information is available at suitable coverage and frequency, it can be used as a-priori knowledge when applying remote sensing retrieval algorithms. A-priori knowledge from such sources could help to overcome inherent limitations of remote sensing in optically complex waters, including vertical non-uniformities (Churnside, 2015), which cause considerable ambiguity in remote sensing signals even at hyperspectral resolution (Pitarch et al., 2014). Note that in this study non-

uniformities and shape parametrization always refer to the vertical profiles of water constituents such as total suspended matter and chlorophyll-a.

The relationship between optically detectable water constituents and remote sensing reflectance R_{rs} is significantly complicated when the vertical distribution of water quality parameters is non-uniform within the photic layer. We expect that the relative contributions to R_{rs} per depth and wavelength depend on the derivative of the round-trip attenuation (Piskozub et al., 2008; Zaneveld et al., 2005), which means that relative signals are largest from the upper zone of the photic layer. The impact of non-uniform vertical distribution of biomass on measured R_{rs} signal has been demonstrated both in optically simple oligotrophic waters (Stramska and Stramski, 2005; Gholamalifard et al., 2013), and optically complex waters (Kutser et al., 2008; Yang et al., 2013; Xue et al., 2015). Yet, the non-uniformities of vertical chlorophyll-a and turbidity gradients in inland and coastal waters come in many shapes with water constituents often varying independently from each other (Fig. 2 in Lee et al., 2013; Fig. 6 in McCulloch et al., 2013; e.g. Fig. 4 in Erga et al., 2014), and the 14 years of measurements in Lake Geneva are a good representation of the variability found in those systems to effectively transfer this basic understanding into application.

Current inversion algorithms (e.g. those reviewed by Matthews, 2011; Odermatt et al., 2012) facilitate self-contained retrieval of water constituent concentrations from R_{rs} . Most of them are based on radiative transfer simulations, which are used directly as look-up-tables for non-linear optimization (e.g. Van Der Woerd et al., 2008) and as training data for neural networks (e.g. Doerffer and Schiller, 2007), or indirectly for the parameterization of semi-analytical approximations such as Gordon et al. (1988) in Lee et al. (2002). The extension of such simulations towards vertical non-uniformities requires a shape parameterization to enhance the comparability of measured and simulated R_{rs} . To minimize the dimensions of such look-up-tables, the number of shape parameters should be small. Previous studies made use of the Gaussian shape approximation by Lewis et al. (1983) in Stramska and Stramski (2005) or two-layer models (Yang et al., 2013), and other representations such as a straight surface-to-peak gradient should be taken into consideration. An assessment of how appropriately they approximate R_{rs} for real vertical constituent distribution is needed, and the findings of this assessment must be traded off against the potential use of a-priori knowledge, which could provide the needed shape parameters.

So far, due to obvious water quality issues, emphasis was put on eutrophic systems where most of the remote sensing optical information is limited to the top meter of the water column. Yet, the problem of retrieving information in lakes characterized by non-uniform vertical constituents apply to most oligo- to mesotrophic lakes that is most lakes on Earth. This study focus on Lake Geneva as a well-

documented example of a system with peaks of turbidity and chlorophyll from the surface to the deeper reaches of the photic layer. Our approach is meant to be directly applicable to any oligo- to mesotrophic lake.

Here, we investigate vertical non-uniformities and assess shape approximations using R_{rs} simulated for chlorophyll-a and turbidity profiles measured in Lake Geneva between 2002 and 2015. During this period, the Secchi depths varied in the range of 1 to 10 m, turbidity was between 0.4 and 4.6 Formazin Turbidity Units (FTU) and chlorophyll-a in the range of 0.8 to 17 mg m⁻³ for more than 95 % of the profiles (plus a very few high exceptions of up to 10 FTU and 45 mg m⁻³, respectively). Lake Geneva is a partial monomictic lake with a seasonal thermal stratification representative for lakes in temperate climate zones, making this study representative for a wide range of mesotrophic lakes worldwide.

3. 2. Methods

3.2.1. Site description

Lake Geneva is the largest natural freshwater lake of Western Europe with a surface area of 582 km² and a maximum depth of 310 m. It is situated between France and Switzerland and consists of two main water bodies, the deep Grand Lac and shallow Petit Lac (Figure 3-1). The Rhône River is the main tributary and the Rhône Valley is the largest part of its watershed. Minor contributors are the rivers Venoge and Aubonne in the north flowing down from the Jura and the Dranse in the south originating in the Alps. The only outflow is the Rhône River at Geneva on the western end of the lake. Lake Geneva became eutrophic in the 1970s largely due to increased human activities in the catchment (Rapin et al., 1989). Extensive wastewater treatment, reduction of fertilizer use and law enforcement reduced nutrient inputs and improved water quality towards mesotrophic status (Anneville and Pelletier, 2000; Kiefer et al., 2015). The first annual phytoplankton blooms generally occur close to the surface in spring, and their growth gradually moves towards deeper layers in the annual course (Dokulil and Teubner, 2012). Since 1957, the lake is regularly monitored by the Commission Internationale pour la Protection des Eaux du Léman (CIPEL) at two stations, SHL2 and GE3, in the Grand and Petit Lac, respectively.

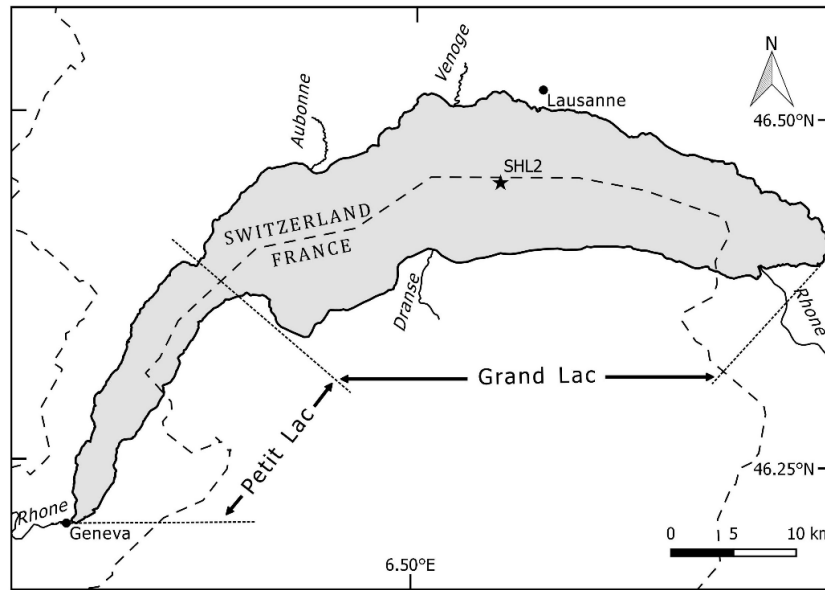


Figure 3-1: Overview map of Lake Geneva. SHL2 indicates the main location of routine monitoring.

3.2.2. Bio-geochemical constituents

Turbidity (*TUR*) and chlorophyll-a (*CHL*) profiles acquired at monitoring station SHL2 (Figure 3-1) between 2002 and 2015 that are available from SOERE OLA (INRA and CIPEL, 2016). The sampling frequency is fortnightly during the productive season between March and November, and monthly for the rest of the year. *TUR* profiles are sampled using different nephelometers and backscatter turbidity sensors according to the latest turbidity standard (ISO 7027-1, 2016): three Seapoint Turbidity Meters that measure FTU in the ranges of 0 to 1000 FTU (CTM214) and 0 to 2500 FTU (CTD009, CTD620) as well as an ECO-A sensor by ME Grisard (formerly ME Meerestechnik-Elektronik). The probes are lowered in the water by an electrical winch and profiles are inspected in real time. The turbidity found in Lake Geneva is only about one percent of the sensitivity range of the instruments, therefore an averaging filter with a window size of 3 m is applied for noise reduction through outlier removal. Up to seven vertically consecutive records within no more than 3 m are clustered, and the central record is removed if its difference from the cluster's median is larger than four times the interquartile range. 32 out of a total of 11,000 records are removed by this procedure. We use *TUR* as equivalent to Total Suspended Matter (*TSM*, in g m^{-3}), according to findings for lakes, coastal and ocean waters (Bukata et al., 1978; Kallio et al., 2012; Neukermans et al., 2012). This correlation decreases with increasing particle diversity in riverine waters (Pfannkuche and Schmidt, 2003; Ruzycski et al., 2014), but is a fair approximation for pelagic lake sites like SHL2 (Figure 3-1). Water samples for *CHL* laboratory analysis are collected at nine depths; 0, 2.5, 5, 7.5, 10, 15, 20, 25, and 30

m, and processed according to the spectrophotometric method by Strickland-Parsons (1968) with regular quality and repeatability control. Given the impeccable quality of the *CHL* data, measurements are only excluded where no concurrent turbidity data is available. After quality control, the remaining 210 pairs of *CHL*(*z*) and *TSM*(*z*) are linearly interpolated to regular 10 cm vertical resolution, *CHL*(*z*_{INT}) and *TSM*(*z*_{INT}).

3.2.3. Vertical profile approximations

Five different models are applied for the approximation of vertical non-uniformities, including the Gaussian approximation according to Lewis et al. (1983; henceforth referred to as GAL), a k-means based Two-Layer Model (TLM) and a linear model (LIN). Using *CHL*(*z*_{INT}) and *TSM*(*z*_{INT}) profiles as input, the GAL model provides depth-dependent concentration *B*(*z*) according to equation (3-1):

$$B(z) = B_0 + \frac{h}{\sigma\sqrt{2\pi}} \exp\left[-\frac{(z-z_{\max})^2}{2\sigma^2}\right] \quad (3-1)$$

Where *B*₀ is the background concentration, *h* is the vertical integral concentration in excess of *B*₀, *z*_{max} is the depth of maximum concentration *B*_{max} and *σ* quantifies the thickness of the layer with *B* > *B*₀. The TLM model provides for a layer boundary at *z*_{l2} if *z*_{l2} is neither zero nor below the maximum expected Secchi depth (i.e. 10 m) and with *z*_{l2} the depth of the shoulder in the TLM as described below. After binary k-means classification of all *CHL*(*z*) and *TSM*(*z*) profiles in the range 0 - 15 m, the upper layer concentration is calculated as the median of all *CHL*(*z*) and *TSM*(*z*) with *z* < *z*_{l2} that are not in the same class as *B*_{max}, and with *z*_{l2} the depth of the shallowest point in the class of *B*_{max}. The lower layer concentration is set to the median of all *CHL*(*z*) and *TSM*(*z*) with *z* ≥ *z*_{l2}. The LIN model uses the same *z*_{max} as GAL and lower layer concentration *B*_{max}, according to the conclusions in Piskozub et al. (2008); for the upper layer a linear gradient is assumed between *B*(*z* = 0) and *B*(*z*_{max}). Finally, two profiles representing vertical uniformity are compiled for reference simulations, by taking the median of *CHL*(*z*_{INT}) and *TSM*(*z*_{INT}) for the top 1 and 5 m (henceforth referred to as M1 and M5, respectively).

3.2.4. Radiometric measurements

Fifteen reflectance measurements acquired between 2014 and 2016 with a TriOS RAMSES system deployed in *z* = 1 m depth (Table 3-1) are used to verify the representativeness of the simulations for Lake Geneva. The extrapolation of in-water measurements towards and through the surface can be a considerable source of errors when striving for *R*_{rs} (Mueller and McClain, 2003). Therefore, *R*[−] is preferred in this study because it is calculated from direct measurements at specific depths. Dimen-

sionless irradiance reflectance R^- is derived according to equation (3-2) from simultaneous measurements of up- and downwelling spectral irradiance, E_u and E_d respectively, at a sampling rate of 0.1 Hz during a 3 minutes run at 1 m depth:

$$R^-(\lambda, z) = \frac{E_u(\lambda, z)}{E_d(\lambda, z)} \quad (3-2)$$

Where $E_d(\lambda, z)$ and $E_u(\lambda, z)$, in units of $\text{W m}^{-2} \text{nm}^{-1}$, correspond to the median of the individual cast for each quantity over each run. The superscript ‘-’ refers to in-water measurements. For optical closure, reflectance R^- was sampled under cloud-free conditions (wind speed $< 2 \text{ m s}^{-1}$) in 15 stations between Lausanne and SHL2 during the 4 campaigns listed in Table 3-1. Water depth was greater than three times the Secchi depth for all measurements, precluding bottom reflectance effects. At every station, 3.0 L of water were sampled at 0.5 m depth and stored in a dark cool box on the boat before filtration in the evening of each campaign. Two separate subsamples were filtered and stored at -40°C before analysis within a month for the following purpose: (i) CHL concentration was determined spectrophotometrically after 1.0 L of water was filtered through $0.8 \mu\text{m}$ GF/F filter papers and immersed in 99 % ethanol for pigment extraction; (ii) 2.0 L was filtered to quantify TSM using gravimetric method on $0.8 \mu\text{m}$ pre-weighted and pre-combusted GF/F filters. Additional 100 mL of water were sampled at the same depth at seven out of the 16 stations for the analysis of Coloured Dissolved Organic Matter (CDOM) absorption. 50 mL was filtered on-boat directly after sampling through $0.2 \mu\text{m}$ polycarbonate filters (Whatman Nuclepore) in dark glass vials stored in a cool box. The filters were pre-washed with consecutively 50 mL of Milli-Q water and 50 mL of water sample. In the evening after fieldwork, CDOM absorption was analysed using a dual-beam spectrophotometer.

Table 3-1: In-situ campaigns conducted in Lake Geneva.

Date	Number of stations	Region
June 6, 2014	3	Lausanne to SHL2
May 11, 2015	9	Lausanne to SHL2
July 4, 2015	1	SHL2
September 22, 2016	2	Lausanne to SHL2

3.2.5. Specific Inherent Optical Properties

The bio-optical model shall be representative for Lake Geneva yet easily comparable to a larger number of optically complex waters. Like in comparable studies (Gholamalifard et al., 2013; Stramska and Stramski, 2005), Specific Inherent Optical Properties (SIOPs) remain fixed for all sampling dates

and depths, which is owed to practical constraints but also favours the interpretability of the simulations. They are defined according to the simulations provided with IOCCG Report no. 5 (2006), other scientific publications and own measurements. Phytoplankton absorption a_{ph}^* (400 - 700 nm) normalized by $a_{ph}^*(440 \text{ nm}) = 0.05 \text{ m}^2 \text{ mg}^{-1}$ is taken from Bricaud et al. (1995), which agrees quite well with long-term averaged coefficients for perialpine Lake Garda (Giardino et al., 2014). The 700 - 800 nm interval was added based on record 237 of the IOCCG dataset, whose 675 nm peak agrees best with the Bricaud et al. (1995) absorption spectrum.

Phytoplankton scattering is neglected because the turbidity used for TSM(z) accounts for scattering by all particle types. Particle absorption a_{TSM}^* is defined according to the exponential model in equation (3-3) from the IOCCG Report no. 5 (2006):

$$a_{TSM}^*(\lambda) = a_{TSM}^*(\lambda_0) \exp[-S_{NAP}(\lambda - \lambda_0)] \quad (3-3)$$

Where the subscript NAP stands for Non-Algal Particles and coefficients $S_{NAP} = 0.0146 \text{ nm}^{-1}$ and $a_{TSM}^*(440) = 0.025625 \text{ m}^2 \text{ g}^{-1}$ are adopted again from IOCCG (2006) record 237, representing approximately median conditions when comparing to the variability of coefficients across the whole IOCCG dataset. The same record is used for b_{TSM}^* , which means the power-law in equation (3-4) is used with $b_{NAP}^*(550 \text{ nm}) = 0.526255 \text{ m}^2 \text{ g}^{-1}$ and $m = 0.716$:

$$b_{NAP}^*(\lambda) = b_{NAP}^*(\lambda_0) \left(\frac{\lambda_0}{\lambda} \right)^m \quad (3-4)$$

Furthermore the Fournier-Forand scattering phase function is used (Fournier and Forand, 1994), with a backscattering fraction b_b/b of 0.0183.

The spectral absorption of CDOM, a_{CDOM} , is approximated with equation (3-5), whose parameters are estimated on the basis of irregular in-situ measurements in Lake Geneva taken between 0 and 3 m of the water column.

$$a_{CDOM}(\lambda) = a_{CDOM}(\lambda_0) \exp[-\gamma(\lambda - \lambda_0)] \quad (3-5)$$

For a_{CDOM} measurements acquired in parallel to the abovementioned reflectance measurements, range and median of spectral slope γ are 0.010 - 0.018 and 0.014 nm^{-1} , respectively, which agrees with measurements in Lake Constance (Gege, 2000; Heege and Fischer, 2004), while for Lake Garda $\gamma = 0.021 - 0.025 \text{ nm}^{-1}$ (Giardino et al., 2007; 2014) are considerably higher. The range and median of the magnitude parameter $a_{CDOM}(\lambda_0 = 440 \text{ nm})$ across our measurements for Lake Geneva are 0.06 - 0.19 m^{-1} and 0.12 m^{-1} , respectively. Simulations are carried out with fixed, vertically uniform a_{CDOM}

(440 nm) = 0.12 m^{-1} and slope ($\gamma = 0.014 \text{ nm}^{-1}$) parameters, because the monitoring data available from INRA-Thonon SOERE and CIPEL lack a suitable proxy for representing vertical non-uniformity in CDOM, and our subsurface measurements display rather stable conditions in the middle of the lake. Expected gradients in $a_{\text{CDOM}}(z)$ due to photobleaching near the surface (Del Vecchio and Blough, 2002) or alignment with the deep CHL maximum as observed in ocean waters (Green et al., 2014; Yamashita et al., 2013) are likely to amplify uniformity effects, but they are not evident in the scarce measurements in Lake Geneva, and rejected in order to err on the side of conservatism when it comes to non-uniformity effects on R_{rs} .

The absorption by pure water is derived with spectral spline fits using several sources for different wavelength ranges, and resampled to 5 nm. From 350 to 550 nm, absorption by pure water is taken from Lee et al. (2015), and from 550 to 725 nm from Pope and Fry (1997) according to Pitarch et al. (2016), and results by Smith and Baker (1981) are used for the range 725 to 800 nm (Pitarch, pers. Comm). Scattering by pure water is computed at the resolution of its absorption using Zhang et al. (2009) relation with zero salinity and a water temperature of 15 °C. Its phase function is taken from the Hydrolight model default file (pureh2o.dbf; see following section for definition) with $b_b/b = 0.5$.

3.2.6. Radiative Transfer Model

Using the abovementioned SIOPs, the Hydrolight 5.3 Radiative Transfer Model (Mobley, 1994; Mobley and Sundman, 2016) is applied to simulate R_{rs} for assessing the effect of different vertical approximation profiles. The solar zenith angle was set to 30° , wind speed is set to 2 m s^{-1} , clear-sky conditions are assumed for solar and sky irradiance calculations by the Hydrolight RADTRAN-X subroutine, and bottom reflectance effects are disabled.

3.2.7. Optical closure

The direct verification of bio-optical models with measured inherent and apparent optical properties requires comprehensive and accurate in-situ measurements, in particular if vertical non-uniformities should be taken into account. Due to the lack of such measurements, we consider the approximation of several measured R^- with Hydrolight simulations at $z = 1 \text{ m}$ for uniform constituent gradients as sufficient evidence that the selected SIOPs are suitable for Lake Geneva. We use the Downhill-Simplex method (Nelder and Mead, 1965) with simultaneously measured CHL, TSM, as initial guess and minimizing the root mean squared error (RMSE) according to equation (3-6) during fit iterations with the function `fminsearch` of the Matlab Optimization toolbox (Coleman, 1999). Because CDOM was not measured at all stations, we used median in-situ measurements of CDOM absorption at 440 nm in the initialisation and γ was fixed using the median value of 0.012 nm^{-1} .

$$RMSE = \sqrt{\frac{1}{N} \sum_{i=1}^N (x_1 - x_2)^2} \quad (3-6)$$

N enumerates wavelengths in 5 nm intervals between 405 to 705 nm, the subscripts meas and sim indicate simulated and measured reflectance spectra, respectively, and x stands for any reflectance spectra under evaluation (in this study either R^- or R_{rs}).

3.2.8. Statistics

The Percent Difference (PD) [%] is used to assess the differences between measured and simulated spectra, or between different approximation models, defined at every wavelength as:

$$PD = \frac{|x_1(\lambda) - x_2(\lambda)|}{\left(\frac{x_1(\lambda) + x_2(\lambda)}{2}\right)} \times 100 \quad (3-7)$$

This metric in percent allows exhibiting the similarities between spectra x_1 and x_2 in terms of amplitude. The larger the PD value, the more distant are the spectra x_1 and x_2 . On the other hand, the spectral shape difference is assessed using the spectral angle (θ), defined as (Dennison et al., 2004; Xue et al., 2015):

$$\theta = \cos^{-1} \left(\frac{\sum_{\lambda=400}^{710} R_1(\lambda) R_2(\lambda)}{\sqrt{\sum_{\lambda=400}^{710} R_1^2(\lambda)} \sqrt{\sum_{\lambda=400}^{710} R_2^2(\lambda)}} \right) \quad (Eq, 3-8)$$

The term θ varies between 0° and 90° , with 0° meaning similar spectra and larger θ showing increasing dissimilarities.

3.2.9. Inversion Algorithms

For evaluating the impact of non-uniformities on inversion algorithms we apply band-ratio-based algorithms that use R_{rs} in different spectral regions. First, the standard Ocean Colour OC4 band-ratio is tested, which uses the blue and green region of the spectra with the general form:

$$\log_{10}(CHL) = a_0 + \sum_{i=1}^4 a_i \left(\log_{10} \left(\frac{R_{rs}(\lambda_{blue})}{R_{rs}(\lambda_{green})} \right) \right)^i \quad (3-9)$$

Where a_i coefficients are taken from Werdell and Bailey (2005) for use of the MERIS sensor, and R_{rs} were convolved using MERIS bands' specific spectral response. The numerator, $R_{rs}(\lambda_{blue})$, in OC4 is the maximum of MERIS bands 2, 3 and 4 (centred at 443, 490 and 510 nm, respectively) over the green band 5 (centred at 560 nm).

The second algorithm used was developed by Gons et al. (2002, 2005) and is henceforth referred to as GONS. It is a semi-analytic algorithm that uses the red near-infrared (red-NIR) region of the spectra as:

$$CHL = \{R_M(0.7 + b_b) - 0.4 - b_b^{1.06}\}/0.016 \quad (3-10)$$

where R_M is the ratio between MERIS bands 9 to 7 (centred at 709 and 665 nm, respectively) of R_{rs} . Again, R_{rs} was convolved to MERIS bands. The term b_b stands for the backscattering coefficient (m^{-1}) derived in the original algorithm using MERIS band 12 (centred at 779 nm) according to:

$$b_b = \frac{1.61\pi R_{rs}(779)}{0.082 - 0.6\pi R_{rs}(779)} \quad (3-11)$$

3. 3. Results

3.3.1. Optical closure

Across all 15 radiometric measurements, the median PD between measured and optimized R^- in the wavelength range between 405 and 700 nm is 4.7 %, and it is always lower than 24 % with larger median PD occurring around 565 nm, and a larger spread occurring above 610 nm (Figure 3-2). The optimization of reflectance magnitudes in blue and red wavelengths is a trade-off because most IOPs come with large magnitude differences between these two wavelength regions. At the same time the euphotic depth for blue light is much larger than for red, and therefore potential non-uniformity effects in the measured R^- complicate the interpretation of the uneven PD level. However, the agreement of spectral shapes between 600 and 700 nm is quite good, indicating that the selected pigment absorption from Bricaud et al. (1995) has an appropriate secondary peak, even though it may be responsible for a small spectral shape bias around 565 nm (Figure 3-2). For the three examples in Figure 3-3, initial and optimized concentrations of CHL, TSM and CDOM are given in Table 3-2 along with minimum and maximum for all simulations. The disagreement is considerable, but still in the range of expected measurement uncertainties and within the non-uniformity effects demonstrated hereafter. Hence we consider the selected set of SIOPs representative for our simulation study.

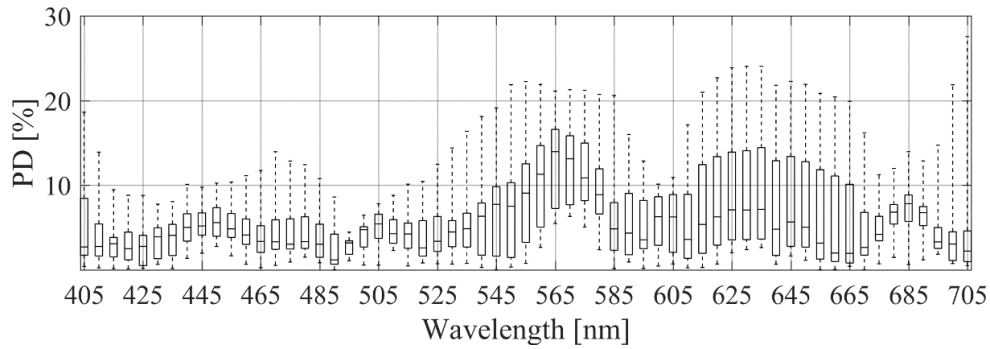


Figure 3-2: PD between 15 in-situ measured and simulated R_r for the concentrations obtained by the Nelder-Mead optimization. $N = 15$, boxes are 1st and 3rd quartile and bars extend to min and max. The line in each box corresponds to the median.

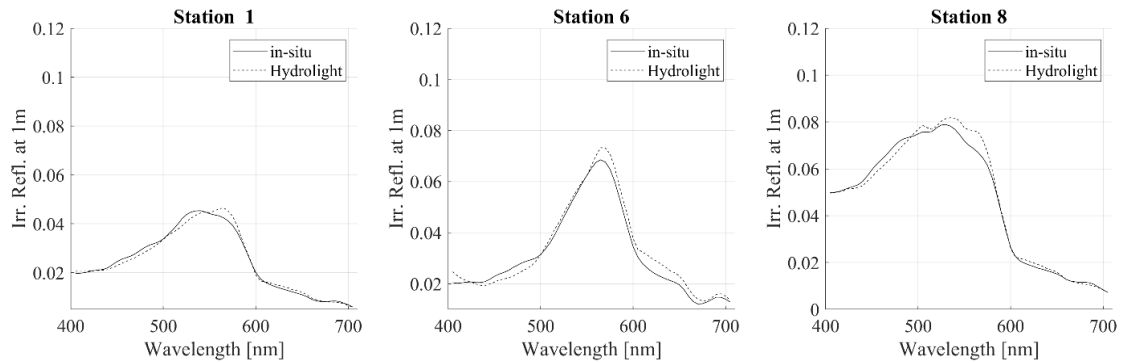


Figure 3-3: Irradiance reflectance at 1 m depth from in-situ measurements (solid lines) and simulated by Hydrolight (dashed lines) for the three different stations listed in Table 3-2.

Table 3-2: Water constituents parameters used in the optical closure. Note: CHL and TSM are near-surface measurements, while a long-term average is used as initial guess for a_{CDOM} .

Stations	Initial concentrations			Optimized concentrations		
	CHL (mg m^{-3})	TSM (g m^{-3})	a_{CDOM} (m^{-1})	CHL (mg m^{-3})	TSM (g m^{-3})	a_{CDOM} (m^{-1})
1	4.1	0.8	0.12	2.6	1.4	0.15
6	18	3.0	0.12	12.7	3.2	0.07
8	2.0	1.5	0.12	1.2	1.7	0.06
Min	1.8	0.5	0.12	0.8	0.7	0.03
Max	18	4.4	0.12	13.4	4.7	0.13

3.3.2. Average annual course of constituent non-uniformities

The average annual course of vertical CHL and TSM non-uniformities in the centre of Lake Geneva corresponds roughly to the four climatic seasons (Figure 3-4). In most years a clear-water phase in winter is subject to low and vertically uniform concentrations in both CHL and TSM, peaking around

4 mg m⁻³ and 1 g m⁻³, respectively. Around the second half of March, spring blooms develop in the top 5 m of the water column, with maximum CHL concentrations between 10 - 20 mg m⁻³. It must be considered that the chance of fortnightly samples representing the actual spring peak in Lake Geneva is low (Kiefer et al., 2015), but CHL levels often remain around 10 mg m⁻³ for several weeks during this period. In summer, productivity decreases and the CHL maximum descends to 10 - 20 m depth due to the depletion of nutrients in the epilimnion and the supply by riverborne nutrients in the thermocline. The fall season is marked by a transition in phytoplankton assemblage with species more adapted to low insolation and mixed water column conditions characterised by lower CHL concentrations compared to the first phytoplankton bloom of the year. The seasonal turbidity peak in the thermocline largely results from the fine glacial inorganic particles transported by the Rhône River and trapped in the thermocline where riverine water typically intrudes during summer (Bouffard and Perga, 2016; Finger et al., 2006).

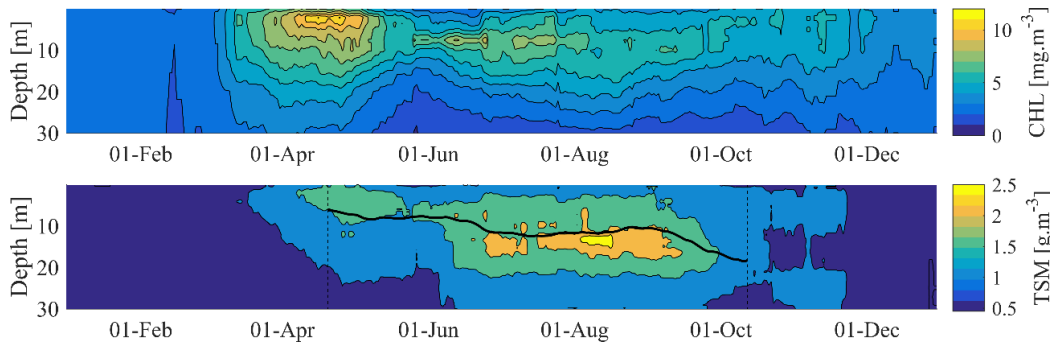


Figure 3-4: Average annual course of CHL(z) (top) and TSM(z) (bottom panel) at station SHL2 (Figure 3-1) in the years 2002 - 2015, aggregated by moving a 15-days averaging time window, and using interpolated 10 cm depth intervals. The black line in the TSM plot shows the thermocline depth aggregated by moving a 15-days averaging time window.

3.3.3. Vertical approximation of seasonally typical profiles

The vertical non-uniformities in CHL and TSM have seasonally specific effects on R_{rs} (Figure 3-5). In winter, the approximation of the constituent's fairly uniform vertical distributions is as simple as redundant, even though the highest light penetration depths occur in this season. Contrariwise, near-surface phytoplankton blooms in spring reduce the euphotic depth in all wavelengths. Non-uniformities develop quickly in the top few meters of CHL profiles, but less so in turbidity profiles. Accordingly, the divergence of R_{rs} simulations for different profile approximations affects predominantly wavelengths with pigment absorption when phytoplankton distribution is assumed to extend to the very surface, as shown for M5 and GAL in the example of 16 April 2007 (Figure 3-5). As non-uniformities in turbidity amplify throughout the productive season, magnitude differences increase. At the same time, the descent of the CHL peak beyond the euphotic depth of red-NIR wavelengths

also constrains that R_{rs} remains representative of a relatively homogeneous upper mixed layer while the most productive layer becomes inaccessible at these wavelengths, e.g. when comparing the alignment of the secondary CHL absorption band at 665 nm for M1 and TLM on 23 June, 2003. The breakup of stratification in autumn brings about a variety of different vertical constituent distributions, ranging from a steady fading towards uniformity in some years, to short-term, near-surface phytoplankton blooms with potentially large effects in other years (e.g. 26 September 2012).

Henceforth, we investigate the appropriateness of profile approximation models by comparing Hydrolight simulated R_{rs} for the five profiles M1, M5, GAL, LIN, and TLM with the simulations for the corresponding measured profiles (INT). In the bottom row of Figure 3-5 R_{rs} spectra are compared and θ and PD are shown as measures of spectral offset.

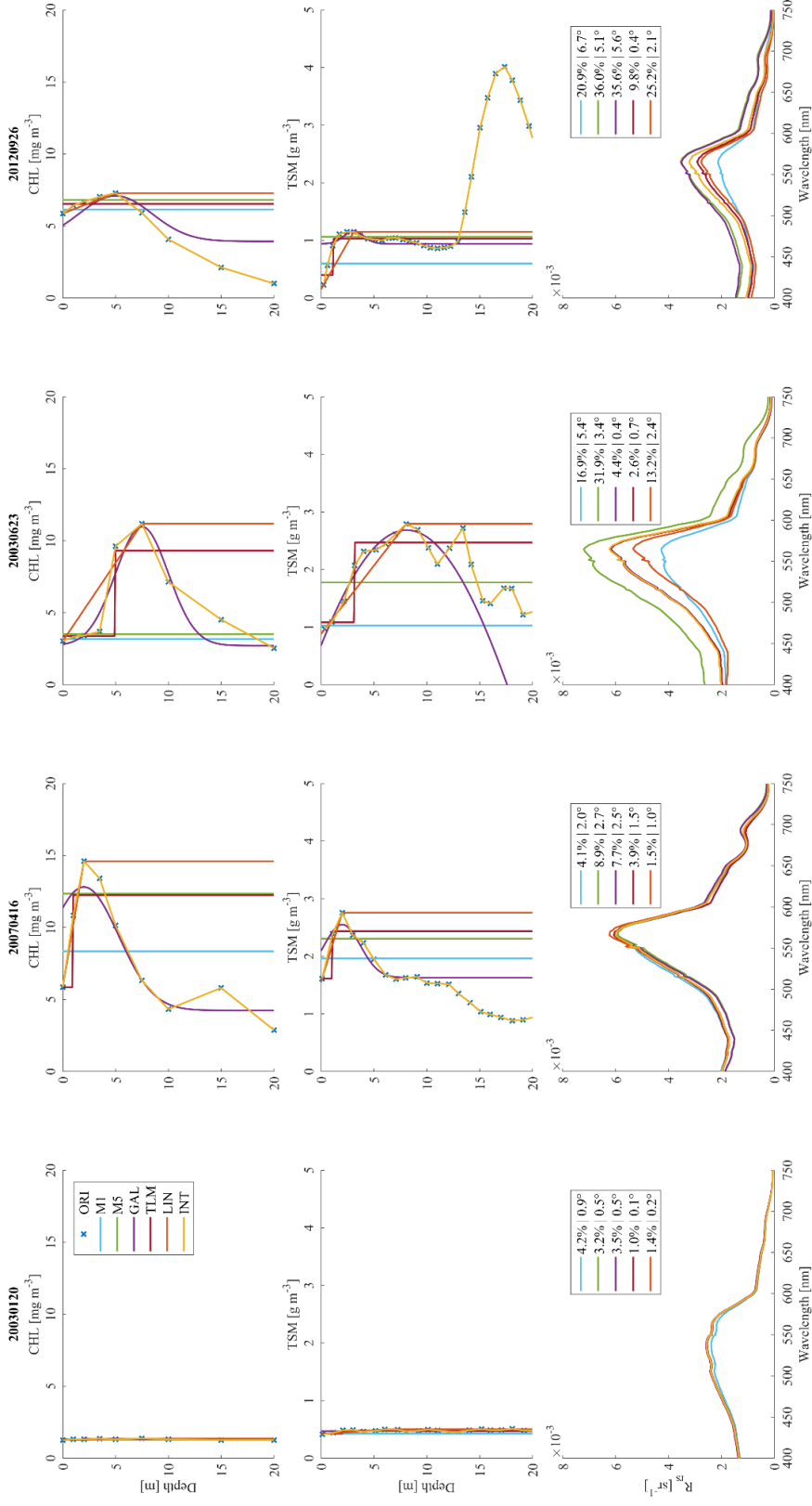


Figure 3-5: Typical examples of CHL profiles (top row), TSM profiles (middle row) and resulting R_{rs} (bottom row) for winter, spring, summer and autumn (left to right). The legend in the top left plot indicates the color code for each simulation and in the bottom row the PD and θ values of M1, M5, GAL, TLM and LIN against INT.

3.3.4. Frequency and temporal distribution of non-uniformities

The temporal distribution of θ for each of the five approximation models for the years 2002 - 2015 provides an overview of the relevance of vertical non-uniformities (Figure 3-6). First we consider M1 and M5, where $\theta > 3^\circ$ for roughly half of the profiles between May and September. The maximum values occur in July with $\theta > 5^\circ$ for roughly half and one-third of profiles approximated by M1 and M5, respectively. During the rest of the year the deviations are generally low even in early spring, which confirms the representativeness of the examples chosen in Figure 3-5. This means that the overall frequency of cases with $\theta > 5^\circ$ is low (20 % and 9 % for M1 and M5, respectively), but these cases cause strong uncertainty during the productive season, which is underestimated when considered only as arithmetic means or medians.

The other three non-uniformity approximation models show significantly lower θ than M1 and M5 (Figure 3-6, bottom row). Their spectral match with INT reference R_{rs} is significantly higher during the productive season, in spite of occasional limitations. In general, GAL and TLM show smallest deviations from the observational estimates. They both provide for a homogeneous surface layer and concentration increases along a more or less sharp layer boundary, as opposed to LIN, which assumes that concentrations increase steadily. TLM's main limitation is that such steady increases still occasionally occur in the measurements, while TLM always defines a sharp boundary. This is less the case with GAL, which simulates perfectly large bell-shaped profiles, but fails when there is a strong gradient at the surface. Maximum θ observed for TLM and GAL are 6.3° and 9.3° , respectively.

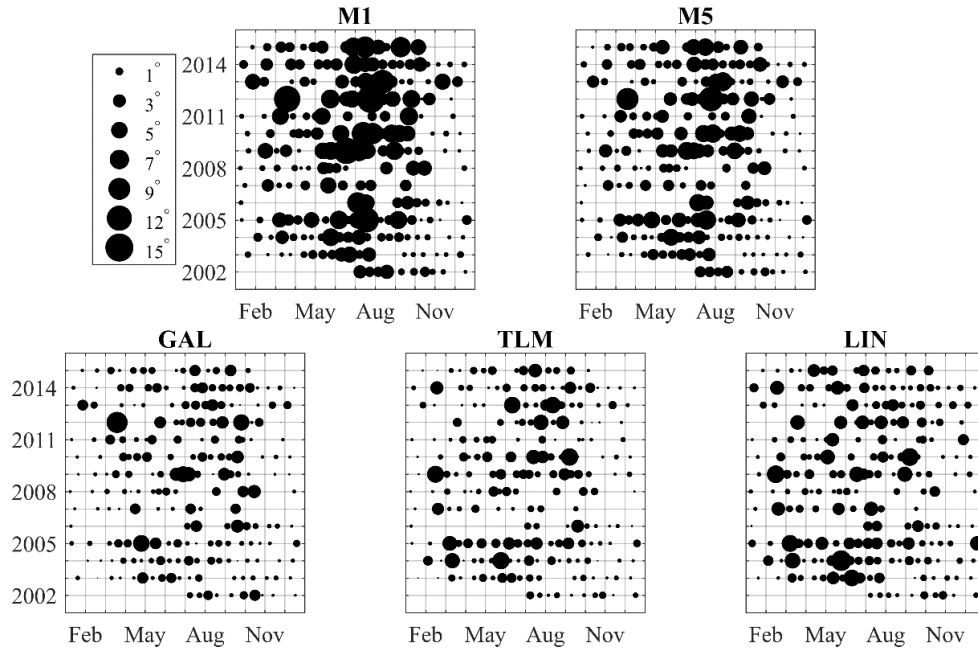


Figure 3-6: Seasonal evolution of the spectral angle for the uniform profiles M1 and M5 (top row) and for the three non-uniform approximation models GAL, TLM and LIN (bottom row).

3.3.5. Assessment of profile approximation models

The performance of the considered approximations depends on the range of the euphotic depths for the different wavelengths during the course of the year, and the approximations' ability to reproduce the constituent concentrations at these depths. This is most obvious for vertically uniform profiles M1 and M5, which are quite appropriate when euphotic depths are in the order of ~ 1 m and ~ 5 m, respectively, but much less in the other spectral regions (Figure 3-7, left). Accordingly, maximum spectral PD of these two non-uniform approximations vary strongly and almost contrariwise, while the median PD of M5 at 400-590 nm is relatively constant.

The accuracy of the GAL, LIN and TLM approximation models is illustrated on the right panel of Figure 3-7. We note that GAL PD distribution is similar to M5 with generally better performances from the former by a factor between 1.5 and 2.0 and it is the model which performs best in the green region, where the maximum PD reaches only 26 % around 560 nm. TLM and LIN have both very similar performances with maximum PD increasing between 400 - 550 nm from 30 % to 64 %. However, the median of TLM is significantly lower varying between 2 to 3 % in the same region against 3 to 6 % for LIN. In the red the median PD for both model remains relatively low and the differences between them decrease whereas maximum values increase from 50 % at 600 nm to > 100 % at 750 nm.

The θ score for each model in Table 3-3: Median and maximum spectral angles between INT and individual approximation models over all simulations. shows that M1 performs significantly worse when it comes to the spectral shape as is the case for magnitudes and the PD (Figure 3-7). The non-uniformity models achieve again a significantly better agreement with INT, with rather insignificant differences between GAL, TLM and LIN.

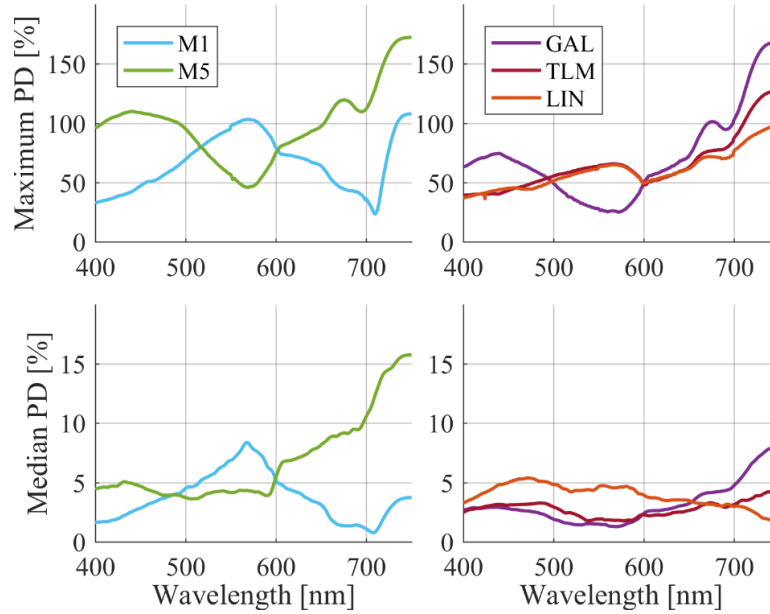


Figure 3-7: Maximum PD (top row) and median PD (bottom row) over all simulations for INT input profiles against the uniform (left) and non-uniform profile approximation models (right).

Table 3-3: Median and maximum spectral angles between INT and individual approximation models over all simulations.

Θ [degrees]	M1	M5	GAL	TLM	LIN
Median	1.96	1.53	0.65	0.67	0.62
Maximum	15.9	12.4	9.3	6.3	8.6

3.3.6. Relative relevance of CHL and TSM

The relative importance of vertical non-uniformities in CHL (z) and TSM (z) is of particular interest given that their vertical gradients are independent. When comparing M1 and M5 for 16 April 2007 and 23 June 2003 (Figure 3-5), we note that the difference in CHL (8.35 and 12.35 mg m^{-3} , respectively) prevails in spring, while the difference in TSM (1.03 and 1.78 g m^{-3} , respectively) prevails in summer. The PD for the former are considerably lower than for the latter, even though the non-uniformities are closer to the surface in spring. A number of similar examples suggest that TSM variations have a considerably larger effect on PD. In order to test this hypothesis on our entire dataset, we investigate the relation between the CHL and TSM variations and the PD between 400 and 700

nm. To get the difference of either CHL or TUR between two different simulations we use M1 and M5 profiles because their difference yields a single scalar. After visual inspection, a log-log relation was selected. For TSM, we found a significant relation ($p < 1 \times 10^{-10}$) at all wavelengths with R^2 minimum in the blue range ($R^2 = 0.3$) and steadily increasing until the red at 650 nm ($R^2 = 0.8$). Those results suggest that a non-linear relation exist between the TSM differences of two profiles and the PD between the resulting R_{rs} . The large R^2 values implies that TSM difference explain a significant amount of variations in the amplitude of the reflectance. For CHL, the null hypothesis can be rejected only around 550 nm ($p > 0.15$) although in the rest of the spectra R^2 is always < 0.05 . As expected, the CHL difference cannot explain a significant part of the variations in PD.

In order to see the direct relation of CHL and TSM on the shape of the R_{rs} spectra rather than the amplitude, we conducted the same experiment using θ instead of the average PD as response variable. Using θ both p-value are almost equal to 0 and gives R^2 of 0.27 and 0.39 for TSM and CHL respectively, showing that both TSM and CHL have a significant impact on the shape of the spectra with the latter being more significant.

3.3.7. Band-ratio algorithm

The effects of vertical non-uniformities on water constituent retrieval algorithms are complex and require individual clarification. As indicative example for expected retrieval errors, we compare CHL retrieved from vertically non-uniform INT simulations with CHL for the corresponding M1 and M5. Non-uniformities affect the retrieval accuracy of the algorithms, and the representativeness of their sensing depth. We investigate both aspects using OC4 and GONS algorithms. Both algorithms have known limitations for processing remote sensing imagery of Lake Geneva. The use of OC4 is impaired by independently varying CDOM and TSM concentrations, and water-leaving radiance and CHL levels are usually too low for robust retrieval from red-NIR reflectance as with GONS. In the case of our factitious simulations, neither effects due to CDOM variations nor uncertainties in R_{rs} at red-NIR wavelengths must be expected, leaving OC4's TSM sensitivity and weak performance of GONS at low CHL levels (see Gons et al., 2008, Fig. 2) as sole inconsistency. As implied by PD in the red for M1 in Figure 3-7, the GONS for INT and M1 are highly correlated in spite of the poor sensitivity of the algorithm for low CHL concentrations (Figure 3-8, $R^2 = 0.89$). This confirms that red-NIR algorithms are almost unaffected by vertical uniformities at least as far as vertical scales resolved by standard in-situ measurements are concerned. However, the restriction on red-NIR wavelengths with minimal penetration depth also means that red-NIR algorithms can resolve near-surface phenomena like spring blooms, while they cannot access relevant dynamics at 5 to 10 m depth in the second half of the year. On the contrary, for OC4 the correlation between INT and M5 ($R^2 = 0.46$) is

slightly higher than between INT and M1 ($R^2 = 0.4$). And, given the potential impact of a few outliers on the determination coefficient, the alignment along the 1:1 line is much better, confirming that the OC4 algorithm has a sensing depth that is overall closer to 5 m than to 1 m.

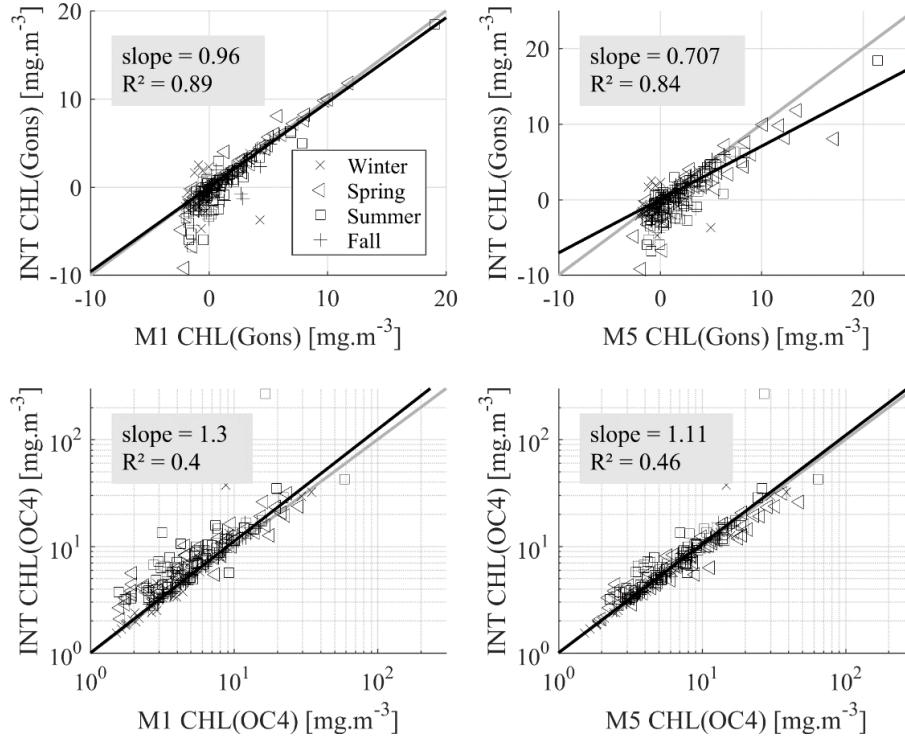


Figure 3-8: Scatter plot of GONS (top row) and OC4 (bottom row) algorithms applied on M1 (left) and M5 (right) against R_{rs} from measured CHL(z). The grey line represents the 1:1 relationship and the black line represent the regression with the resulting slope and R^2 provided in the text box of each plot. Note that a log-log scale is applied to cope with the scatter of OC4 samples while a lin-lin scale is required to display the negative values in GONS.

3. 4. Discussion and conclusions

Our findings suggest a number of practical implications for water quality remote sensing of oligo- to mesotrophic lakes, which represent the global majority. These implications concern effects of non-uniformity on retrieval accuracy, the relevance of different sensing depths across the visible and near-infrared spectrum, and the integration of vertical non-uniformities in invertible bio-optical models.

In standard water quality remote sensing validation, retrieval results from (atmospherically corrected) R_{rs} of vertically non-uniform profiles are compared to vertically explicit or averaged water constituent concentration measurements. The comparisons in Figure 3-8 emulate such a validation by comparing retrieval results from R_{rs} of vertically non-uniform profiles and those from R_{rs} of constant vertical concentration profiles. The resulting R^2 and sample alignment are slightly better than in typical validation exercises for similar lakes (e.g. Odermatt et al., 2010), even though significant error sources

are ineffective (CDOM, sensor noise, atmospheric correction). We found that about 20 % of the 210 samples in our dataset are affected by significant non-uniformities (INT compared to M1, $\theta > 5^\circ$). This means that together with other limitations, such as different horizontal sampling locations (e.g. Moses et al., 2016) and related variations in IOPs (e.g. Babin et al., 2003), vertical non-uniformities are a major obstacle to provide accurate remote sensing products in oligo- to mesotrophic lakes.

Based on this first conclusion, we argue further that the increasing popularity of red-NIR algorithms is supported by their minimal sensitivity to vertical non-uniformities. Using adjacent wavelengths with similar and low penetration depths, such algorithms retain robustness and comparability to surface samples even where non-uniformities occur. However, given that only a relatively small part of the annual primary productivity and other relevant near-surface processes in oligo- and mesotrophic waters occur in the top 1 m of the water column (Figure 3-4), the usage of such algorithms implies that a significant amount of these processes remain unnoticed. On the other hand, we conclude that algorithms using larger portions of the reflective spectrum suffer much more from differences in light penetration depth due to vertical non-uniformities.

Developing retrieval algorithms that account for non-uniformities introduces the challenge of an increased number of unknown parameters. In this regard, we observed that vertical non-uniformities in TSM have a larger effect on R_{rs} than those in CHL, and that the vertical gradients in TSM and CHL are independent. When it comes to the approximation of those vertical gradients, GAL requires four shape parameters (B_0 , z_{max} , h and σ) and approximates the entire gradient across the defined 10 m depth. On the contrary, TLM and LIN require only three shape parameters to approximate the upper and more relevant side of approximately bell-shaped constituent gradients. Based on the performance assessment in Figure 3-7 and Table 3-3, the TLM is best suited to produce realistic R_{rs} for algorithm development.

Further research is required to relate predictable stratification indicators, such as thermocline depth (Figure 3-4), to the TLM layer boundary of vertical constituent distributions, and hence create applicable a-priori information for inversion procedures. Specifically, we aim to compile a Look-up Table that accounts for non-uniformities and which can be searched by means of model-derived a-priori knowledge. Based on promising results from validation and long-term analyses of remotely-sensed chlorophyll-a concentrations (Kiefer et al., 2015), a hydrodynamic model for the lake (Razmi et al., 2013, 2014) is in further development to provide near-real time estimates of mixing layer depth and other physical parameters as potential input for remote sensing methods (<http://meteolakes.ch>). In addition, it should be investigated whether analogous effects can be observed for near-surface CDOM gradients due to photo-degradation.

In summary, we demonstrated the need to account for vertical inhomogeneity in CHL and TSM for correctly analysing remote sensing reflectance in oligo- to mesotrophic lakes, which show characteristic non-uniformities to significant depth. This work is part of an attempt to better connect remotely sensed observations with hydrodynamic and water quality modelling. While the former typically provides information for validation of the latter, the latter can also be used to provide ancillary information to better constrain the classical ill-posed inverse retrieval procedures. It is through such activity of coupling various sources of information that breakthrough solution will be provided for lake ecosystem understanding and monitoring.

Acknowledgments

This work was supported by the Margaretha Kamprad Chair and by the Fondation pour l'Etude des Eaux du Léman (FEEL) on Lake Geneva, as well as Dr. Paulsen Foundation Inc. and the Council Foundation for Baikal Protection on Lake Baikal. We gratefully acknowledge Tiit Kutser, Koponen Sampsa and Peter Gege for their comments and help to improve the manuscript as well as all members of the APHYS laboratory (EPFL) for their contribution during fieldwork and long-lasting support.

Chapter 4

Inter-comparison of atmospheric corrections for S-2 observations over Lake Geneva

Vincent Nouchi¹, Daniel Odermatt², Alfred Wüest^{1,4}, Damien Bouffard⁴

¹*Physics of Aquatic Systems Laboratory, Margaretha Kamprad Chair, EPFL-ENAC-IEE-APHYS, CH-1015 Lausanne, Switzerland (vincent.nouchi@epfl.ch)*

²*Odermatt & Brockmann GmbH, Stampfenbachstrasse 57, CH-8006 Zürich, Switzerland*

³

⁴*Eawag, Swiss Federal Institute of Aquatic Science and Technology, Surface Waters – Research and Management, Seestrasse 79, CH-6047 Kastanienbaum, Switzerland*

Manuscript under preparation for submission in: European Journal of Remote Sensing.

Abstract

In this study we investigate the performances of four atmospheric correction procedure applied to Sentinel-2 observations over the clear water Lake Geneva, namely, ACOLITE, c2rcc, iCor and Polymer. We use a comprehensive dataset in order to assess the representativity of the comparison in terms of both atmospheric and water conditions. We provide an evaluation of the current alternatives for atmospheric correction over water targets, to guide the selection of an adapted procedure in future applications over Lake Geneva and the peri-alpine region.

4. 1. Introduction

The recent launch of Sentinel-2 (S2) Multi Spectral Instrument (MSI) and Sentinel-3 Ocean and Land Colour Instrument (OLCI) is a great leap toward the systematic integration of remote sensing products for the monitoring of complex systems such as inland waters (Bukata, 2013; Bresciani et al., 2018). Recent studies have shown the potential of MSI to accurately retrieve water quality parameters (Liu et al., 2017; Pahlevan et al., 2017; Toming et al., 2016) given that an appropriate atmospheric correction (AC) is applied.

The electromagnetic radiation collected by a space-borne sensor predominantly originates from the atmosphere (Gordon, 1978), and the correction of aerosol reflectance in AC methods is known to be the largest source of error for the retrieval of water quality parameters in inland waters (Doerffer and Fischer, 1994). It is therefore necessary to apply reliable correction to remote observations. For operational monitoring of inland waters, AC methods that rely solely on concurrent measurements of atmospheric parameters to remote observations is mostly irrelevant for practical operation reasons. In this study we focus on methods referred to as image-based, which are much more practical in terms of required inputs. The term ‘image-based’ refers to the fact that those methods use the satellite image itself to estimate the atmospheric contribution to the at-sensor radiance.

Here, we tested the retrieval performances of four AC methods for the water-leaving reflectance from S2 over one clear water lake, namely Lake Geneva. The performance assessment was split in two sections: (i) comparison against in-situ water-leaving reflectance measurements, (ii) image based performance visualisation using change detection algorithm and principal component analysis.

4. 2. Methods

The ACs output consist of S2 bands 1 to 7 and band 8a, however the type of lake under investigation, the last two bands are very noisy due to general low reflectance in the NIR and are excluded from the analysis.

4.2.1. Lake Geneva

Lake Geneva is the largest freshwater lake in Western Europe located between France and Switzerland. It is a clear water lake with bi-annual bloom events (Kiefer et al., 2015), occasional calcite precipitations (Nouchi et al., submitted) and particle plumes initiated by the melting of ice from the surrounding mountains. The Rhône River is the main tributary of the lake on the eastern end originating from the Rhône Glacier. Minor rivers are the Dranse in the south also originating from the Alps and the Venoge and Aubonne in the north flowing down from the Jura Mountains.

Satellite data

Lake Geneva is covered by Sentinel-2 (S2) tile 34TGM at a resolution of 10 to 60 m for bands used in inland water monitoring. The S2 L1C product were obtained from the Copernicus open access HUB (<https://scihub.copernicus.eu/>) on six days where ground sampling was performed. For each S2 scenes we obtained the Aerosol Optical Depth (AOD) (m^{-1}) product MOD04 (Levy et al., 2015) from the U.S NASA Goddard Space Flight Center (GSFC, <https://oceancolor.gsfc.nasa.gov>). The aerosol product is generated at 3 km using the dark target aerosol algorithm from look-up-table-derived reflected and transmitted fluxes. A summary of AOD statistics over the leman region is provided in Table 4-1, along with the number of the sampled station for the same day.

Table 4-1: AOD statistics from MODIS observations over the Lemman region, and station number sampled for six Sentinel-2 observations in Lake Geneva. All water sampling was performed the same day of the overpass, except for the acquisition on June 19, 2017 when the sampling was performed on June 22, 2017.

	25.05.2016	24.06.2016	23.08.2016	22.09.2016	10.05.2017	19.06.2017
Median	0.194	0.131	-0.009	0.15	0.022	0.201
Min	0.088	0.011	-0.039	0.062	-0.041	0.093
Max	0.642	0.323	0.078	0.354	0.145	0.385
Station #	3, 4	1, 2, 3, 4	1, 2	1, 2, 5	1, 2, 3	6, 7, 8

We selected three S2 scenes (Figure 4-1 to Figure 4-3) representative of the situations found in Lake Geneva during matchup activities. The boxes on the top right corner of Figure 4-1 to Figure 4-3 depict the AOD product for the same day and the box used in the statistics in Table 4-1. The image from June 24, 2016 displays a large river plume on the East from the Rhone River coming from the melting of ice in the Alps, which reach its intensity peak in spring of each year. The second image is covered with high altitude clouds, an often ambiguous situations for atmospheric corrections. The last image is dominated with a large plume further discussed in the following.

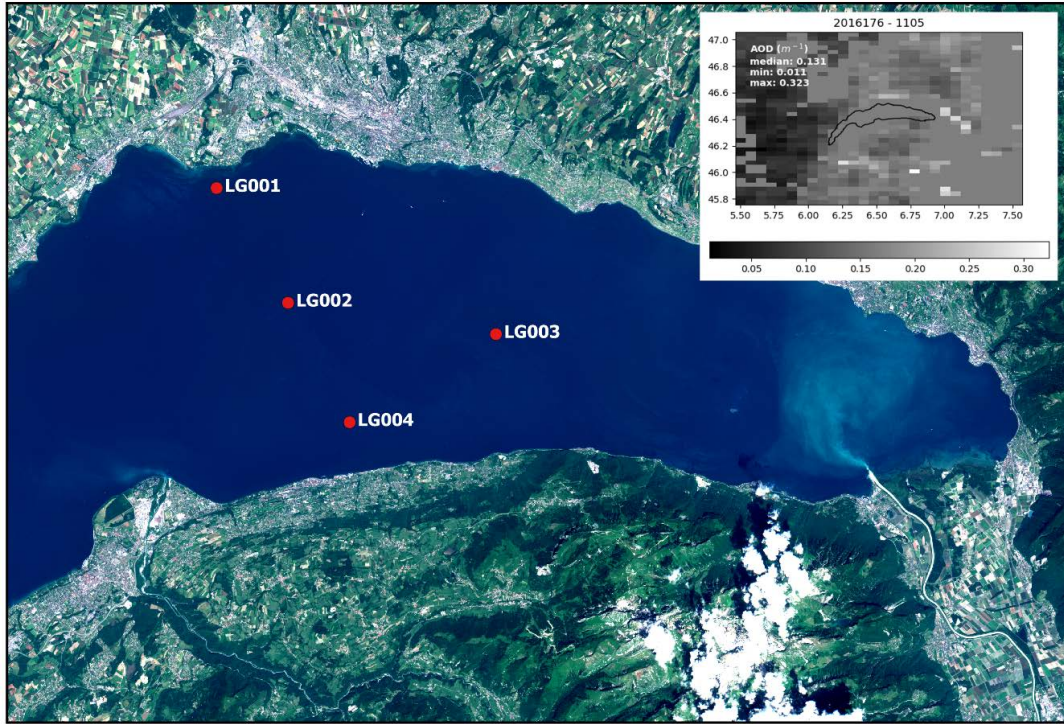


Figure 4-1: S2 acquisition over Lake Geneva on June 24, 2016. The red circles show the water sampling locations for the same day.

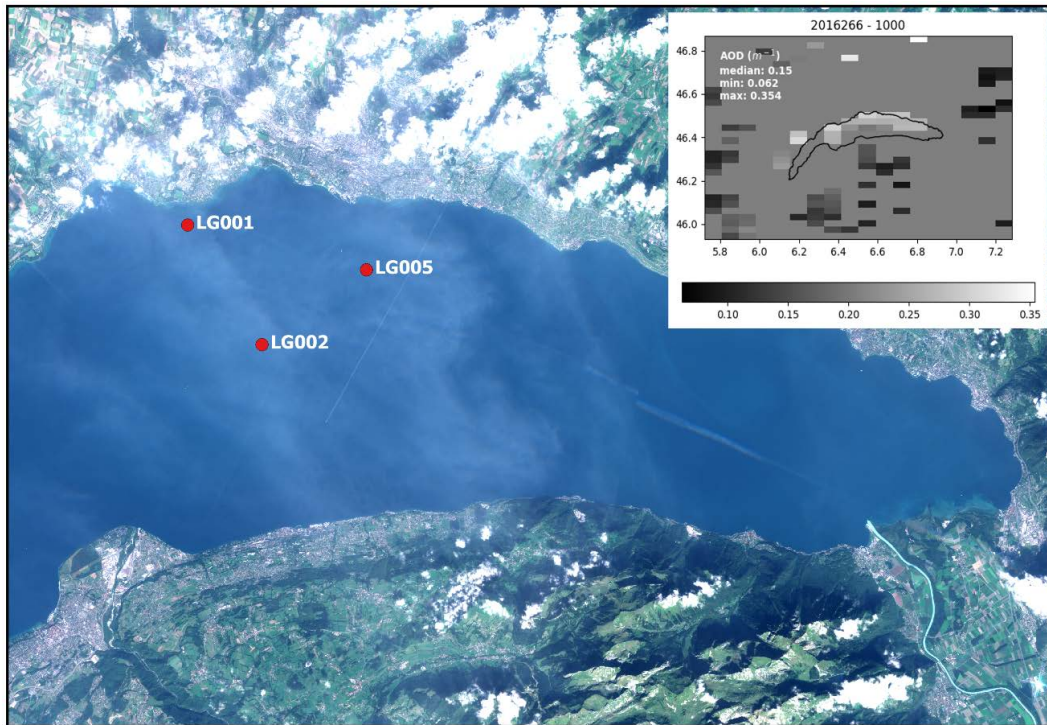


Figure 4-2: S2 acquisition over Lake Geneva on September 22, 2016. The red circles show the water sampling locations for the same day.

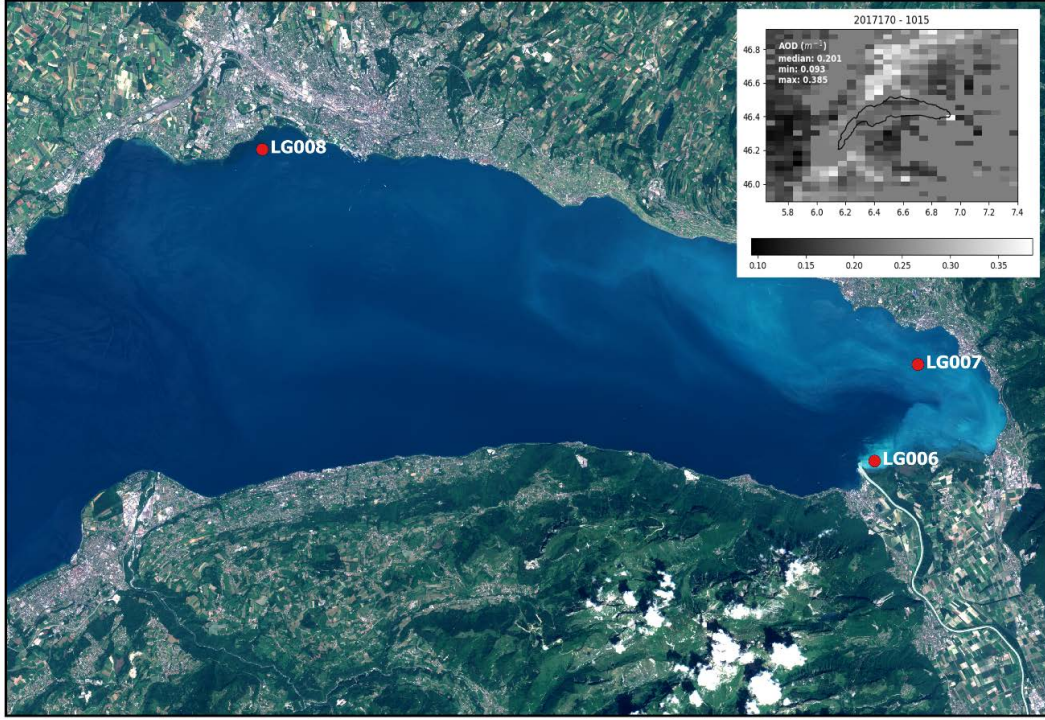


Figure 4-3: S2 acquisition over Lake Geneva on June 19, 2017. The red circles show the water sampling locations on June 22, 2017.

In-situ dataset

For each S2 scene, ground reflectance was measured and lake water was sampled within 3 hours of the acquisition except for June 19, 2017 when field measurements were carried out 3 days later on June 22. Eight different stations were sampled for a total of 17 matchups (Table 4-1). In-situ sampling stations used to validate S2 acquisition are displayed in Figure 4-1 to Figure 4-3. Reflectance was measured using the Water Insight WISP-3 (Hommerson et al., 2012), a hand-held radiometer which combines 3 sensors to measure above-water the downwelling reflectance E_d ($\text{W m}^{-2} \text{nm}^{-1}$), the sky radiance L_s ($\text{W m}^{-2} \text{nm}^{-1} \text{sr}^{-1}$) and the upwelling radiance L_u ($\text{W m}^{-2} \text{nm}^{-1} \text{sr}^{-1}$) at 3 nm resolution. Both radiance sensors are tilted with an angle of 42° from zenith and nadir respectively and the instrument was pointed 135° away from the sun following the recommendation from Mobley (1999) to minimise the impact of sun glint. The remote sensing reflectance R_{rs} (sr^{-1}) is derived using equation (4-1) from Mobley (1999) and a factor of π was applied to obtain the water-leaving reflectance ρ_w (λ). In turn, $\rho_w(\lambda)$ was convolved to S2 resolution by applying the MSI bands response.

$$R_{rs}(\lambda) = \frac{L_u(\lambda) - \rho L_s(\lambda)}{E_d(\lambda)} \quad (4-1)$$

Where ρ is the proportionality factor that relates the amount of sky reflectance by the sea surface. Because of low wind conditions during measurements campaign ($< 5 \text{ m s}^{-1}$), ρ was set to 0.028 following the recommendations from Mobley (1999). At each station, a minimum of 6 individual records were acquired and the median was taken. Finally, all water samples were analyzed for Chlorophyll-a (Chl) using the Strickland and Parsons (1968) method, and for total suspended matter (TSM) using gravimetric measurements. Their concentration varied between 1.2 and 13.1 $\mu\text{g L}^{-1}$, and between 0.7 and 4.6 mg L^{-1} for Chl and TSM, respectively. Largest TSM concentrations occurred on June 22, 2017 (Figure 4-3) with a large plume extending from the Rhône River mouth to the northern shores of the lake. Further investigation is ongoing to identify the characteristics of this plume, the S-2 scene (Figure 4-3) and in-situ R_{rs} measurements point toward a calcite precipitation event, but additional measurements are required¹ (Chapter 2) to advance conclusions. This clarification is particularly relevant in the case of c2rcc and Polymer, where the backscattering of water constituents plays an important role in the atmospheric correction procedure (see below).

4.2.2. Atmospheric corrections

The Top Of Atmosphere (TOA) reflectance $\rho_t(\lambda)$ measured by a sensor can be partitioned into three main contributors as:

$$\rho_t(\lambda) = \rho_a(\lambda) + \rho_r(\lambda) + t \cdot \rho_w(\lambda)$$

where $\rho_a(\lambda)$ is the aerosol reflectance, $\rho_r(\lambda)$ is the Rayleigh reflectance, and t is the two-way diffuse atmospheric transmittance. The purpose of the atmospheric correction procedure is to retrieve $\rho_w(\lambda)$. In most methods presented below, the Rayleigh correction is performed using modified version of the look-up-table-based 6 SV code (Vermote et al.; 2006) to account for haze and surface effects and is currently not included in the analysis. The combination of $\rho_a(\lambda)$ and $\rho_r(\lambda)$ and their interactions constitute altogether the path radiance $\rho_{\text{path}}(\lambda)$.

Acolite

ACOLITE AC is distributed by the Royal Belgian Institute of Natural Science (<https://odnature.naturalsciences.be/remsem/software-and-data/acolite>) and is fully described in Vanhellemont and Ruddick (2014, 2015, and 2016). It is an adaptation of Sea-viewing Wide Field-of-View Sensor Data Analysis System for the processing of Landsat-8 / Operational Land Imager (OLI) and Sentinel-2 MSI for marine and inland waters application. This method is based on the approach by Gordon and

¹ The dataset is currently available on the website of the SOERE-OLA and is ready for analysis.

Grodon and Wang (1994), which revolve around the aerosol type (ϵ). This term is calculated over water pixels where $\rho_w(\lambda)$ is assumed to be null, in the SWIR procedure using band 11 (1.6 μm) and band 12 (2.2 μm), as the ratio between Rayleigh corrected reflectance $\rho_c(\lambda)$ at the two wavelengths. This ratio is then extrapolated to the visible domain using a simple exponential relation in order to compute $\rho_w(\lambda)$ at each wavelength λ_i as:

$$\rho_w(\lambda_i) = \frac{1}{t^i} (\rho_c(\lambda_i) - \epsilon^{i,j} \rho_{am}(\lambda_j))$$

where the subscript j denotes the largest wavelength used in the calculation of ϵ .

In this study, we tested different setup to estimate ϵ (Table 4-2) in order to assess the suitability of the different method under relatively clear atmospheric conditions (Table 4-1) over typical conditions in Lake Geneva. The experiment is designed to (i) get a comprehensive understanding of the error associated with a wrong parametrization of ϵ including comparison with previous studies (Doxani et al., 2018; Martins et al., 2017; Vanhellemont and Ruddick, 2014; 2015), (ii) identify the consequence of the spatial assumption, (iii) identify the best method for Lake Geneva,.

Table 4-2: Description of the methods tested for the estimation of ϵ in Acolite.

Method	Name	Bands (nm)	ϵ spatial assumption	ϵ determination
SWIR	exp1	(1600, 2200)	fixed	equal 1
SWIR	exp3	(1600, 2200)	fixed	median over entire scene
SWIR	exp4	(1600, 2200)	fixed	median over clear waters
SWIR	exp5	(1600, 2200)	variable	per-pixel
NIR	exp6	(665, 865)	fixed	median over clear waters
NIR	exp7	(665, 865)	fixed	median over entire scene
NIR	exp11	(665, 865)	fixed	equal 1

C2RCC

The Case 2 Regional CoastColour (C2RCC) processor is a Neural-Network-based method for AC over coastal and inland waters. It is an extension of the original Case 2 Regional processor developed by Doerffer and Schiller (2007) through the CoastColour project to cover extreme ranges of scattering and absorption (Brockmann et al., 2016). C2RCC is part of the Sentinel-3 toolbox for SNAP (ESA). The neural nets responsible for the atmospheric correction is trained using a procedure based on the one mentioned above. The neural-net is fully autonomous and the only input is the atmospheric parametrization. In this study we used NASA meteorological data (<https://oceandata.sci.gsfc.nasa.gov/>) for ozone and atmospheric pressure at sea-surface parameters.

iCor

iCor, formerly known as OPERA is distributed by VITO (Sterckx et al., 2015). The method is based on Guanter et al. (2007) for the land-based Aerosol Optical Thickness retrieval, and can be used on both land and water pixels for L-8 OLI and S2 MSI. All parameters used in the processor are retrieved from the image and from ancillary data. Specific atmospheric correction parameters are derived from MODTRAN-5 LUTs. The AOD is retrieved using a top-down approach, in order to relate $\rho_t(\lambda)$ to known end-members within the image. The different end-members are typical of lands, like dense vegetation or bare soil, and this procedure is referred to as land-based AOD retrieval. The AOD is then extended locally of water pixel assuming local spatial invaribility of the aerosol. The water vapour is also retrieved from the image using S2 bands across this feature.

Polymer

Polymer is a python package distributed by HYGEOS (<https://www.hygeos.com/polymer>) and described in Steinmetz et al. (2011). POLYMER is based on a spectral matching method within the visible and NIR spectral region and it is applicable in the whole glitter pattern. The spectral matching is based on two models for the estimation of the path reflectance. The first model is an atmospheric model which makes use of a polynomial to estimate the reflectance of atmospheric contribution based on the SOS radiative transfer code (Lenoble et al., 2007) based LUT mentioned above. The second model is an ocean reflectance model based on Morel (1988) and the update from Morel and Martorena (2001). Even though this model was developed for Case-1 water, the introduction of a variable backscattering coefficient makes it possible to be applicable to case 2 waters (Steinmetz et al., 2011). Like iCor, the atmospheric parameters are retrieved from the image and ancillary meteorological data (ozone, water vapour concentration, atmospheric pressure) are automatically downloaded from NASA.

4.2.3. Statistics

Prior to the analysis all bands of the atmospherically corrected images were down-sampled to the resolution of the coarser band investigated at 60 m. We used Python 3.6 programming language for the entire analysis and SNAP (ESA) software and Java API to process and read the S-2 images.

The root mean squared error (RMSE) is used to assess the differences between the spectral signature vector of an image pixel and ground control points R_w , defined at S-2 bands between 443 and 740 nm as:

$$RSME = \sum_{i=1}^n \sqrt{\frac{(x_i - y_i)^2}{n}} \quad (4-2)$$

With x_i and y_i any reflectance spectra and at band i and n is the number of S2 band used for the analysis. This metrics allows to see the amplitude difference between atmospherically corrected image and the ground control reflectance. For assessing the spectral shape differences, we used the spectral angle (θ) defined as (Kruse et al, 1993):

$$\theta(x, y) = \cos^{-1} \left(\frac{\sum_{i=1}^n x_i y_i}{(\sum_{i=1}^n x_i^2)^{\frac{1}{2}} \times (\sum_{i=1}^n y_i^2)^{\frac{1}{2}}} \right) \quad (4-3)$$

The spectral angle goes from 0° when spectra are very similar to 90° when spectra are completely different.

Regression analysis was performed between AC output $\rho_w(\lambda)$ and ground control $\rho_w(\lambda)$ to evaluate the performances of the AC methods used in this study. We used robust regression to take into account errors on both side of the axis. In fact, ground measurements and simulations yield errors that must be taken into account and the robust regression is a workable approach to account such deviation. The advantage is the absence of distribution assumption, where the slope and R^2 value depends solely on observations.

Finally, a PCA was used in order to show the impact of environmental factors such as glint and adjacency effect on the ACs. For each spectral band of S2, we carried out PCA using the water-leaving reflectances from the different ACs as the four original dimensions. The first Principal Component obtained in such manner indicates where the algorithms obtained consensus, subsequent components indicate features that are not equally resolved by all ACs.

4. 3. Preliminary results and discussion

4.3.1. Atmospheric conditions

The assessment of atmospheric conditions during S-2 observations is mandatory to assess the representativeness of this study in terms of aerosol composition of the atmosphere. In the following, we rely solely on MODIS observations but our results show the limitations of this dark-target-based approach with a significant amount of flagged pixels and even slightly negative values (Figure 4-1 to Figure 4-3). In Switzerland, and around Lake Geneva, the AOD and other atmospheric parameters are consistently monitored at Palézieu < 20 km away from the northern shores of the lake. This additional dataset would allow to (i) assess the error for MODIS observations, (ii) display the typical range of variations encountered in the region of Lake Geneva, and (iii) describe the atmospheric composition. From the MODIS acquisition, the median AOD value over the Lemman region varied

between ~ 0 to 0.201 m^{-1} , with intra-scene variations of up to 0.554 m^{-1} . This relatively large variability highlight the limitations of methods based on the spatial homogeneities at different scale to estimate the aerosol contribution in every pixel of an image. It further indicates that the S2 scenes considered were acquired under relatively clear atmosphere and no special event were recorded. Exceptional events over Switzerland which can significantly alter the aerosol composition have three principal origin: the incursion of Saharan dust, volcanic ashes, and forest fires, and this study is therefore not representative of these situations.

Estimation of aerosol contribution

The AOD estimation plays a central role in iCor atmospheric correction procedure, which use a direct estimation to account for the contribution of aerosols. We compared the accuracy of retrieval against MODIS observations, but our comparison may suffer the quality limitations inherent to MOD04 products over inland waters. In general, there is a good agreement between iCor and MOD04 as illustrated in Figure 4-4 with values within the range of MODIS observations, and similar variations observed (Table 4-1). However, a more robust analysis involving reliable source of AOD is further required to assess the validity of the iCor product, but the results are coherent with previous findings over land areas (Doxani et al., 2018).

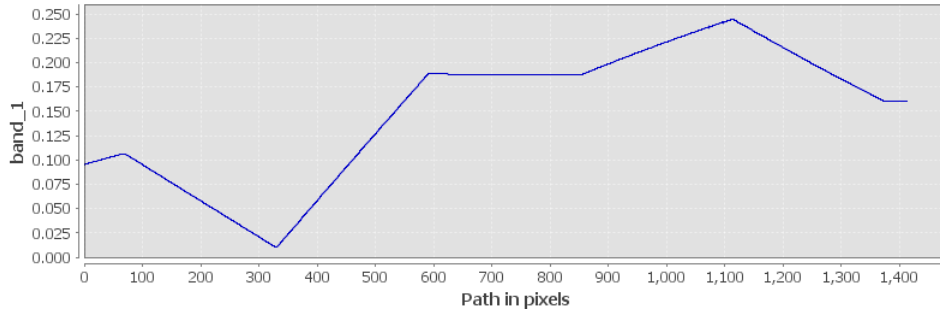


Figure 4-4: Transect of the AOD product of iCor over Lake Geneva region for the S2 acquisition of June 24, 2016.

The spatial variations of the AOD over the entire scene and its implication for Acolite estimation of the aerosol reflectance in Acolite is further developed in the following. Table 4-3 presents a résumé of the statistics for the different experiments introduced previously (Table 4-2) against ground control. Note that the acquisition under overcast conditions on September 22, 2016 was discarded from the analysis, because pixels under these conditions only reflect the issues related to the masking threshold used in the filtration. The results suggest that the impact of the variations in the estimation of ϵ yields relatively small variations in the spectral shape. The deviation observed in this regard can be attributed to the spectral rotation generated by the different exponential models involved.

The variations associated with the estimation of ε have, however, a significant impact on the amplitude accuracy of the spectra with resulting deviations ranging from 15 to $> 100\%$ compared to in-situ control. With regard to the spatial assumption, we observe almost no differences when ε is fixed over the scenes between equivalent procedures. Specifically, between Exp3 and Exp4 on one hand, and Exp 6 and Exp7 on the other hand, the only difference is the spatial region of the image involved in the estimation of ε , and using clear water pixels do not change the retrieval accuracy. However, we see important difference in the SWIR procedure when using variable aerosols within the S2 scenes with lowest rmse in both the visible and NIR domain. These findings suggest the importance to account for the spatial heterogeneity of the aerosol composition in Lake Geneva and within peri-alpine. The comparison between the SWIR and NIR procedures indicate a general performance improvement when using the NIR region of the spectra. The differences observed between Exp1 and Exp6 further suggest that a ratio of 1 of $\rho_c(\lambda)$ seems more accurate between 665 and 865 nm, but leads to an overestimation of the aerosol contribution in particular situations leading to negative values of $\rho_c(\lambda)$, which is never the case in the SWIR procedure involving this ratio. These findings suggest that a NIR procedure provides better general results in the situations observed, but gives also negative values which considerably impact the practicability of the procedure to cover a larger range of situations. In the following, we elected Exp 5 as the best configuration for Acolite over the range of conditions involved in this study.

Table 4-3: Statistics of the performances of different procedure used in ACOLITE to retrieve the aerosol contribution. The median rmse designated by ' $\langle \rangle$ ' is partitioned into two spectral region: visible (VIS) and near-infrared (NIR). The VIS region encompasses the first 4 bands of S2 from 444 to 665 nm, and the NIR region refers to band 5 and 6 of S2 centered at 704 and 740 nm, respectively. The last column indicate the number of matchups with at least one negative value in the 6 bands considered

	$\langle \text{Rmse} \rangle$ (VIS, NIR)	$\langle \theta \rangle$ ($^\circ$)	N negative (/14)
Exp1	(0.0152, 0.0071)	0.232	0
Exp3	(0.0098, 0.0032)	0.208	6
Exp4	(0.00984, 0.00324)	0.209	6
Exp5	(0.00921, 0.00271)	0.175	2
Exp6	(0.00955, 0.00334)	0.255	9
Exp7	(0.00957, 0.00334)	0.255	9
Exp11	(0.0124, 0.0028)	0.222	2

4.3.2. Water-leaving reflectance

We compared the spectral signature of matchup pixels of atmospherically corrected images against in-situ $\rho_w(\lambda)$ in Lake Geneva. From the figure we see that Polymer and c2rcc are the closest to the reference with lowest rmse for c2rcc with an average of 0.0022 over all matchups, and lowest θ for Polymer with an average of 0.12° (Figure 4-5). Those results shows the good ability of c2rcc to properly retrieve the amplitude of $\rho_w(\lambda)$ but Polymer, with slightly higher rmse (0.0029) score better in terms of spectral shape (average θ of 0.15° for c2rcc). On almost all panels of Figure 4-5 we see that iCor gives the worst performances with unlikely large values in the NIR for the clear waters of Lake Geneva. Acolite displays intermediate performances, with relatively good accuracy except for the overcast scene of September 22, 2016 and for the bright plume situation of June 19, 2017. The situation on September 22, 2016 is particular because in-situ sampling was performed in the presence of high cirrus (middle right panel of Figure 4-5). In this situation, and as it is expected Acolite and iCor over-estimate $\rho_w(\lambda)$ by a factor of 2 to 3 but, c2rcc and Polymer happen to handle the situation perfectly. This is especially true for c2rcc where even the shape of the spectra is similar to in-situ matchup. In order to remove the impact of cirrus from the analysis, this S2 scene is excluded from the statistics presented in Figure 4-5. Another peculiar situation is displayed in the bottom-right panel of the latter figure where the sampling point was within a large plume in Lake Geneva, with $\rho_w(\lambda)$ reaching 0.044 at 560 nm. In this ‘bright’ situation all ACs perform similarly, with an advantage for Polymer and Acolite with similar performances, and except for c2rcc which fails to properly retrieve the shape of $\rho_w(\lambda)$ (θ of 0.11° against 0.069° for Polymer). This situation influence considerably the rmse value in the green region of the spectra for c2rcc and illustrate the sensitivity of c2rcc to exceptional scattering properties.

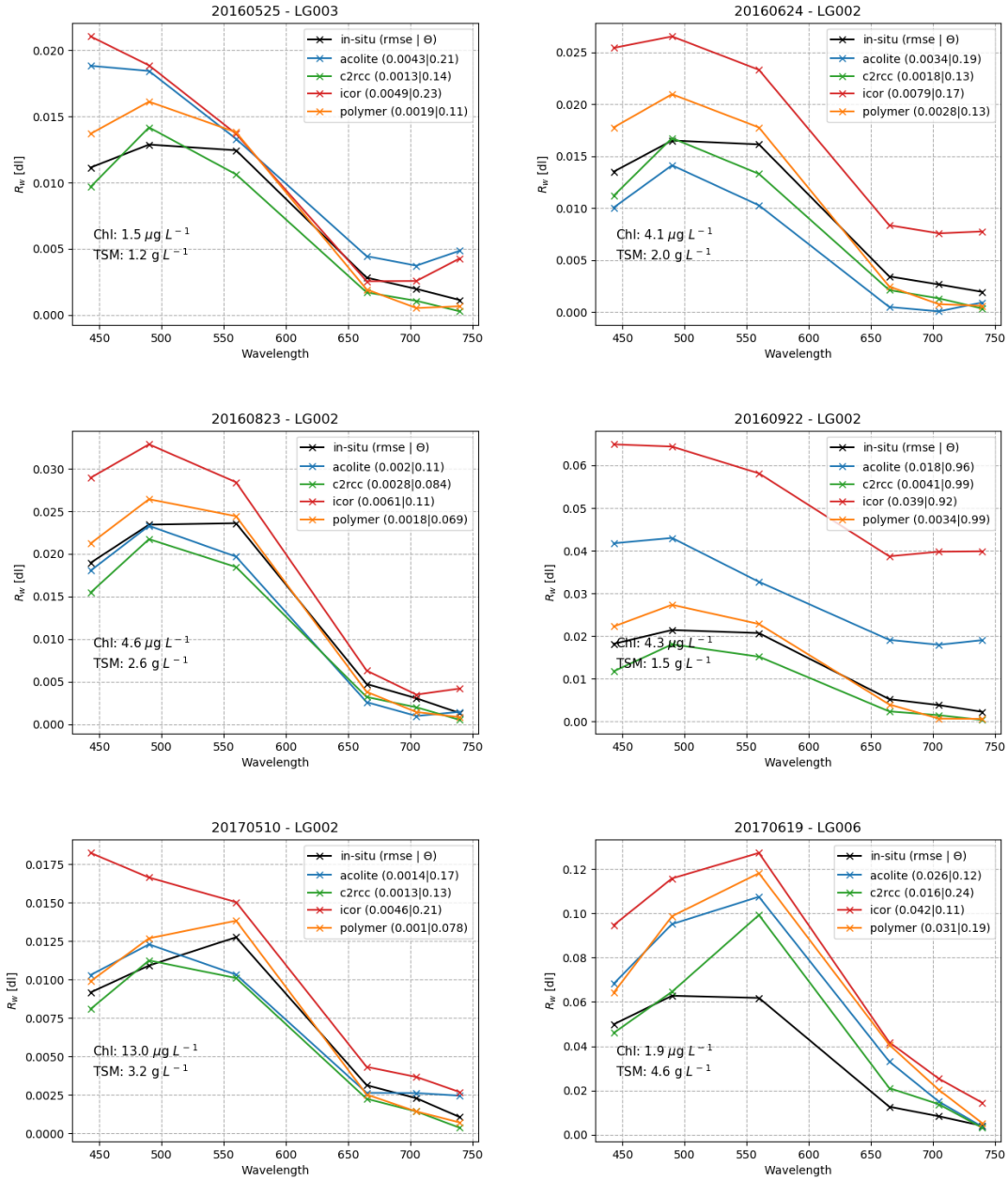


Figure 4-5: $\rho_w(\lambda)$ for Lake Geneva at S2 bands 1 to 6 for the four ACs: namely, Acolite (blue), Polymer (orange), c2rcc (green) and iCor (red) against in-situ $\rho_w(\lambda)$ (black). Each panel correspond to a different S2 scene. In the legend is given the rmse and θ in parenthesis for each AC against in-situ measurements. The quantity of TSM and Chl from water sampling is indicated on each panel.

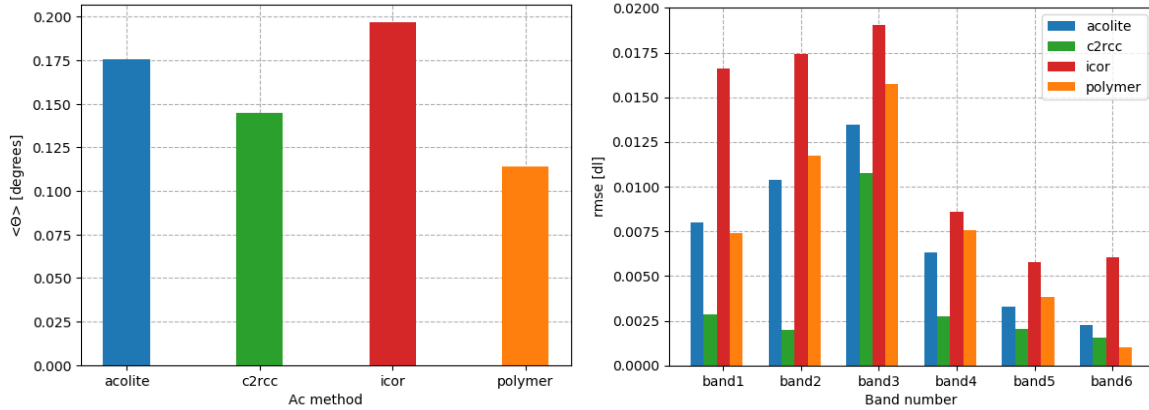


Figure 4-6: θ (left) and $\text{rmse}(\theta)$ for each bands of S2 considered in the analysis. The scene from September 22, 2016 was discarded in order to remove the impact of high altitude clouds of the retrieval accuracy.

4.3.3. Water optical properties

The relative impact of water constituent concentration profiles on the performance presented previously is difficult to assess due to the small sample size of the current study, however, our results suggest a few practical implications. In fact, c2rcc present the best overall performances but often fails to properly retrieve the shape of the spectra; assessing the impact of these variations on the accuracy of inversion algorithm is therefore especially relevant to provide accurate recommendations. The acquisition from June 19, 2017 further involves some important considerations for ACs methods which are directly impacted by water constituents in the retrieval procedure, namely c2rcc and Polymer. One direct output of c2rcc is the backscattering coefficient with two components: a white scatterer, and a typical sediment scatterer. Although the role of these components is unclear² in the atmospheric procedure due to the lack of documentation, the potential of c2rcc to identify white scatterer is of great interest within the scope of my thesis and related forthcoming studies. In this case, c2rcc do not recognize any white scatterer (Figure 4-7), and this may explain the spectral dissimilarities between the output of c2rcc and in-situ $\rho_w(\lambda)$ on June 19, 2017 (lower-right panel of Figure 4-5). The use of the conditional in the latter sentence indicates that further analysis are required for the identification of this event, and we therefore do not develop further this topic here. The accurate identification of the event will also allow to get a better understanding of the performances of Polymer in the presence of unusually bright scatterer. The current assumption involve the limitations of a

² The documentation of c2rcc is rather scarce and we will add Carten Brockmann to this study to get a comprehensive understanding of the training procedure involved in the neural net, and additional expertise for the interpretation of the results.

method developed for Case 1 waters and tested in conditions where the variable backscattering coefficient was zero. In Figure 4-8, we make a comparison between a classical plume from the Rhone River and the ‘bright’ situation of June 19, 2017. We see a more steep change between the classical plume and surrounding clear waters, with slightly lower values in the brightness area compared to the ‘bright’ plume (1.1 against 1 m^{-1} , respectively). These findings suggest the current limitations of the bio-optical model used in the spectral matching procedure and point toward potential improvements in the procedure.

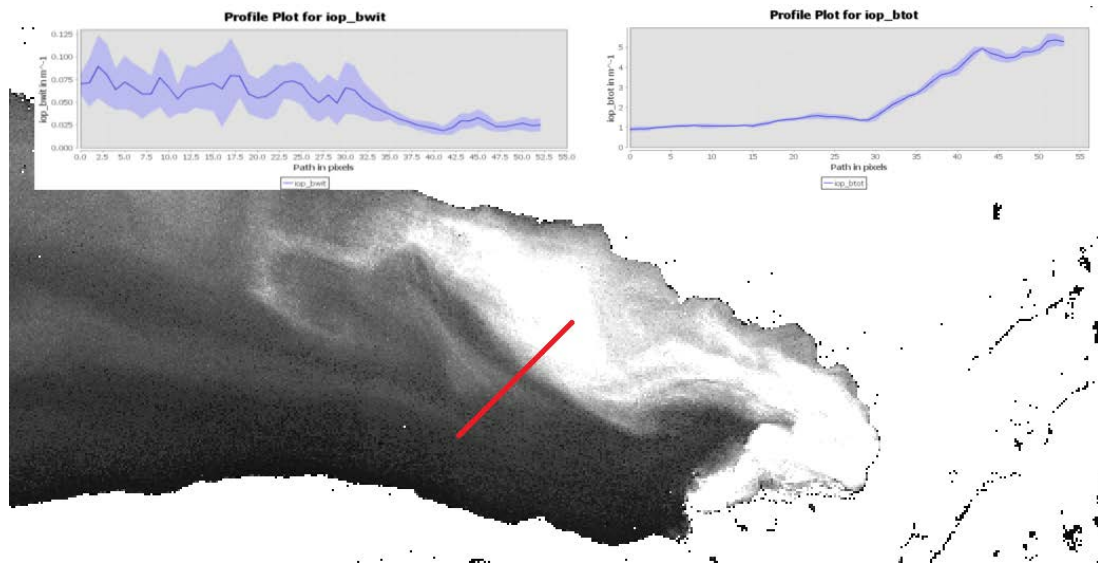


Figure 4-7: Total scattering retrieved from c2rcc AC procedure. The inlets correspond to the total scattering (right) and the relative contribution by white scatterer (left) along a transect (red line). The southern part of the arrow correspond to the zero on the x-axis. On the white scatterer plot, the y-axis ranges between 0 and 0.175 m^{-1} , and it ranges between 0 and 6 m^{-1} on the total scattering plot.

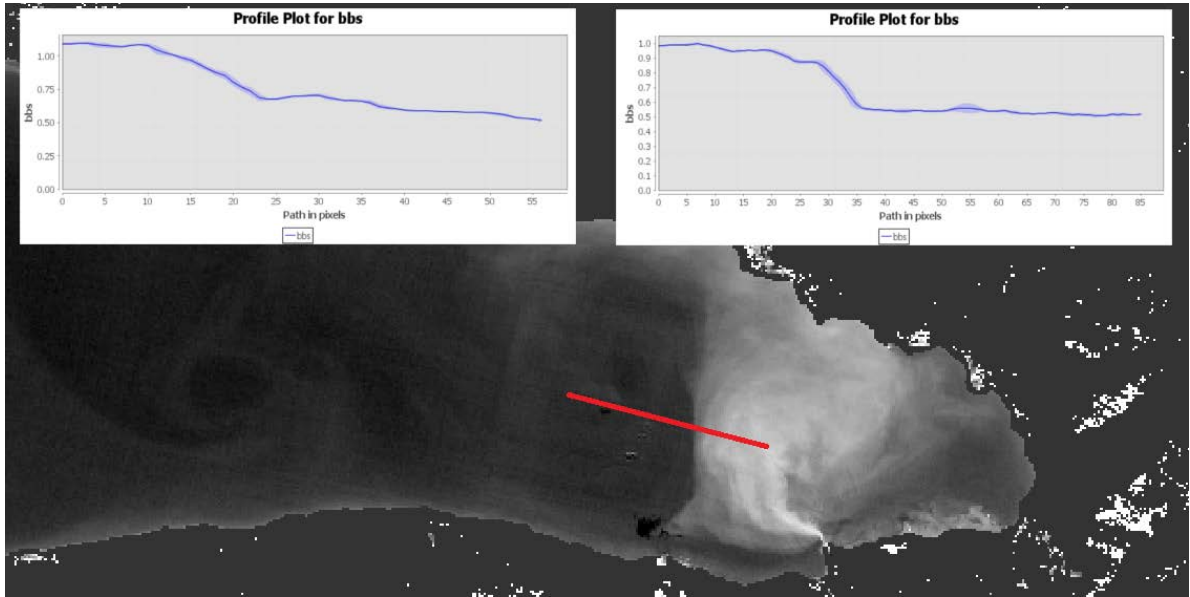


Figure 4-8: Profile plot of the backscattering coefficient retrieved by Polymer on the S2 acquisition from June 24, 2016 (right inlet) and from June 19, 2017 (left inlet). The right profile correspond to the transect represented by the red line, and the left profile to the red line in Figure 4-7. Increasing values in the x-axis correspond the east-west direction for obvious logical reason. Environmental factors

4.3.4. Environmental factors

The S2 scenes used in this study were contaminated by three significant environmental factors: cirrus, glint, adjacency effects. The effect of the former is depicted in the middle-right panel of Figure 4-5 with exceptionally large rmse value for ACOLITE and iCor (0.018 and 0.039, respectively). The good ability of c2rcc and Polymer (rmse of 0.0041 and 0.0039, respectively) to handle thin clouds is particularly promising to develop the temporal representativeness of spaceborn observations. The response of the ACs to glint and adjacency was described during a PCA-based approach. Glint and adjacency effects are responsible for the majority of dissimilarities observed among the scenes (Figure 4-10), in proportion similar to the variations depicted in the previous section (Figure 4-7 and Figure 4-8). In general, the four ACs can be separated into two groups presenting similar response (Figure 4-9). Polymer and c2rcc on one side and Acolite and iCor on the other side. The two groups displayed antagonist response to the different environmental factors: the former group handled well glint but was responsible for a large majority of the high values along the shore of the lake depicted in Figure 4-8; while glint area, almost everywhere else (except some image artifact from iCor which appears on the image as white scattered pixels), was strongly correlated with the latter group.

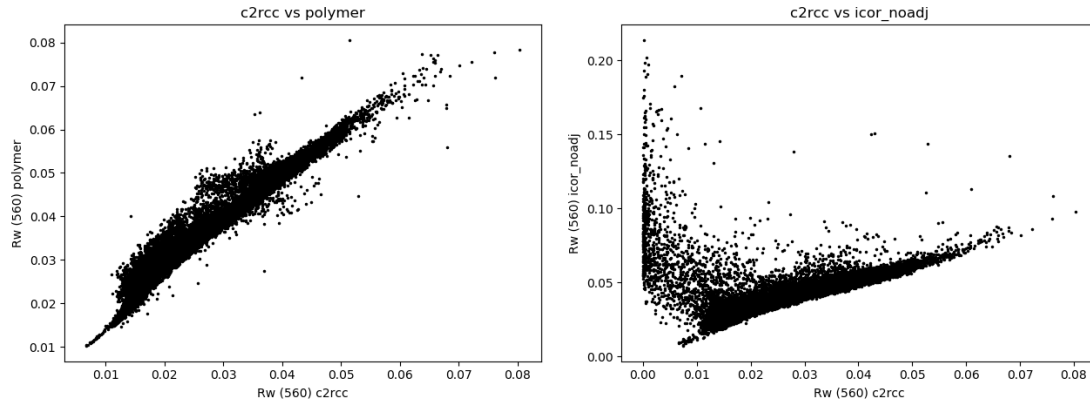


Figure 4-9: Scatter plot of ρ_w at S2 band 3 (560 nm) for the acquisition on June 24, 2016 of c2rcc versus polymer (left) and c2rcc versus iCor (right).

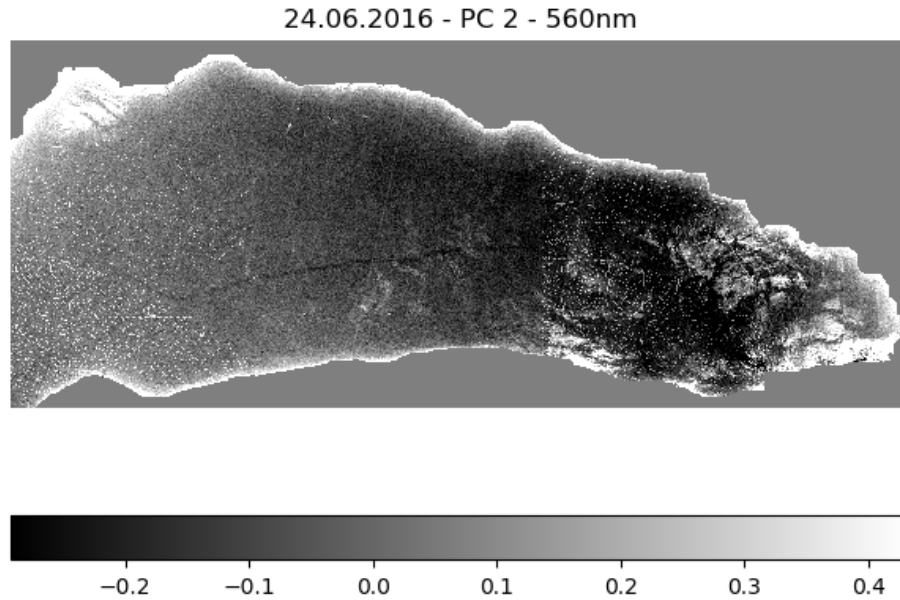


Figure 4-10: Second component of the PCA analysis of S2 band 3 (560 nm) from all atmospheric corrections applied to the acquisition from June, 24 2016

4. 4. Conclusion & perspectives

In this study, we demonstrate that Polymer and c2rcc are the most suited atmospheric corrections for Lake Geneva and we discuss some important implications for inland water monitoring. First, we show that c2rcc perform best overall to retrieve the amplitude of the spectra and that Polymer is more accurate in terms of spectral shape. Specifically, c2rcc usually fails to properly retrieve the spectral shape of R_w in the blue-green region of the spectra. Second, we show that both ACs react in a similar fashion to environmental factors such as thin clouds, sun glint, and adjacency effects. While the two former effects are properly accounted for by these ACs, the latter effect is still visible

in the output image. Finally, the bad results of iCor illustrate the invalidity of the assumption of spatial homogeneity of AODs in the perialpine region and the results for Acolite show an improvement when atmospheric parameters are estimated on a per-pixel basis.

In this chapter we present the preliminary results of ongoing research, and we identify some important challenges associated with the findings discussed in the previous section. Specifically, we identify three main axes to further develop the results of this study:

- Atmospheric conditions: The MODIS AOD product must be combined with reliable sources of observations to further evaluate the implications of the spatial assumptions involved in iCor and Acolite; and to precisely assess the range of situations covered.
- Inversion algorithms: The impact of spectral deviations of the different ACs on inversion procedures will allow to extend our conclusions.
- Calcite precipitation identification: This will allow to better understand the factors influencing the accuracy of Polymer and c2rcc and to a lesser extent ACOLITE.

In order to extend our findings to darker waters, we are collaborating with Finnish institutes, who provided a matchup database of $\rho_w(\lambda)$ simulated using Hydrolight and based on in-situ IOPs and water constituent measurements concurrent to S2 observations. A glimpse of the results is provided in Figure 4-11, where we see that c2rcc is the only method to provide somehow accurate results with yet a factor of 1.5 to 2 with Hydrolight simulations in darkest situations. To ease the interpretation the spectra depicted in this figure, the main constituent concentrations are corresponding stations are provided in Table 4-4. Note the increasing accuracy of Polymer with decreasing concentrations.

Table 4-4: In-situ matchup table in relatively dark to very dark waters in Finland.

Station #	Chl ($\mu\text{g L}^{-1}$)	TSM (g L^{-1})	aCDOM(440)
49	30	8.2	8.8
73	19	9.5	3.2
132	3.4	1	1.7
268	9.4	3.4	3.3

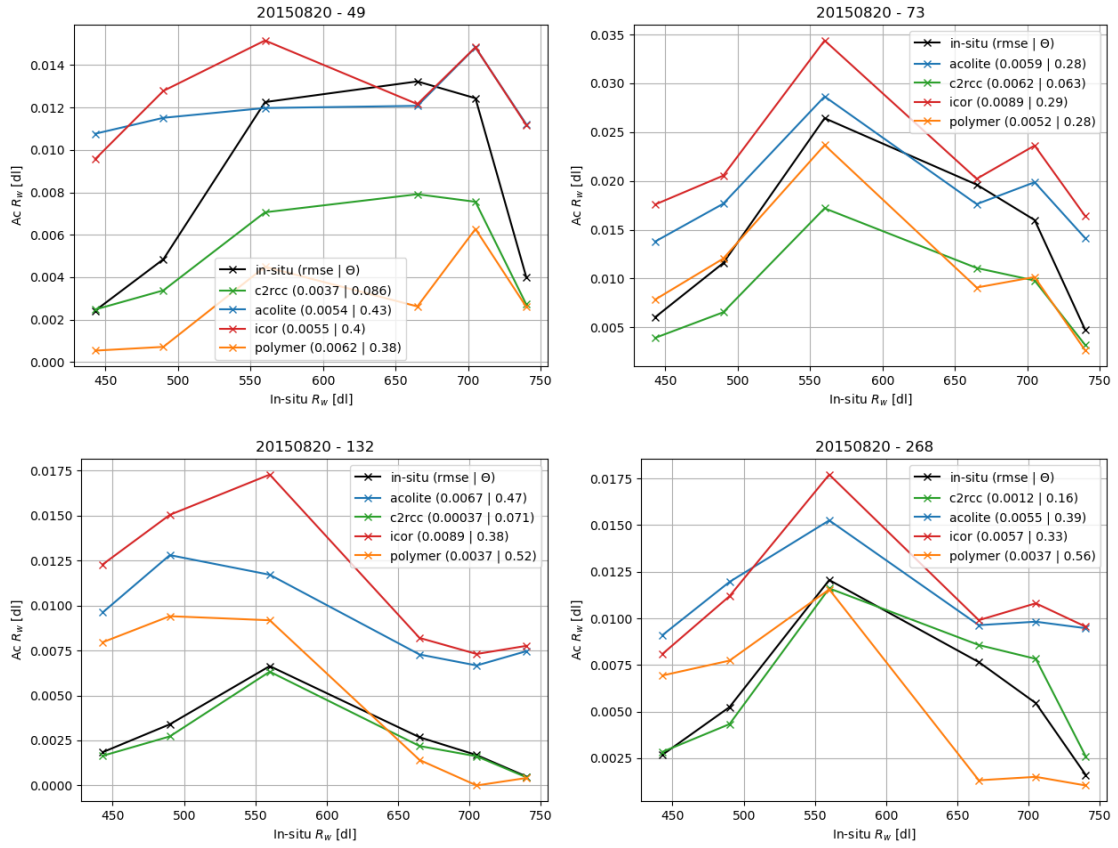


Figure 4-11: $\rho_w(\lambda)$ for Lake Geneva at S2 bands 1 to 6 for the four AC: namely, Acolite (blue), Polymer (orange), c2rcc (green) and iCor (red) against in-situ $\rho_w(\lambda)$ (black). Each panel corresponds to a different S2 scene. In the legend is given the rmse and θ in parenthesis for each AC against in-situ measurements.

Chapter 5

Conclusion

5. 1. Main achievements

The research within this thesis addresses specific challenges related to remote sensing of oligo- to mesotrophic lakes, and I propose improvements for remote sensing products for these specific natural waters. In the following, the main scientific findings of the thesis are presented as answers to the research questions formulated in section 1.3.2.

How can remote sensing be further integrated into interdisciplinary lake studies?

The results presented in Chapter 2 illustrate exemplarily the value of the integration of remote sensing in lake studies. We use complementary remote sensors to analyse at both spatial and temporal scales a distinct calcite precipitation event and provide the material for future remote sensing-based identification of such process. We further highlight the importance of understanding the connections between the optical properties and the bio-geochemical process under investigation to avoid misinterpretation of the signal. Additional information provided by hydrodynamic models and bio-geochemical analysis is the key to an integrated interpretation of satellite-borne observations.

How can additional information, provided by hydrodynamic models and biogeochemical analysis, be integrated to the interpretation of remote sensing observations?

Using river intrusion models, vertical constituent profiles and chemical analysis allow to better characterize the nature and vertical distribution of optically significant constituents in the water column. In Chapter 3, we investigate the suitability of simple approximation models to extend the vertical information provided by remote observations and we discuss a number of practical implications for water quality remote sensing of clear water lakes. These implications are developed by answering the following two questions.

How does vertical non-uniform constituents profiles affect the remote sensing reflectance measured in oligo- to mesotrophic lakes?

From the results of this thesis we show that oligo- to mesotrophic lakes are particularly sensitive to the effect of non-uniform constituent profiles. We observed that TSM and Chl vertical gradients have a different impact on R_{rs} . For instance, the former have larger effect on the amplitude of R_{rs} , but both constituents influence its shape. These considerations add to the challenges of developing accurate inversion procedure over oligo- to mesotrophic waters and we discuss the underlying constraints by answering the following question.

What is the effect of vertical non-uniform constituents profile on inversion algorithms?

The major impact of vertical non-uniform constituents profile on R_{rs} is inherent to the spectral discrepancies of the depth of light penetration. By applying different inversion procedures involving different regions of the spectra with different penetration depths, we show that the information retrieved correlates with different surface layer thicknesses. On one hand, red-NIR algorithms are less sensitive to vertical non-uniformities because of a low penetration depth of the light in this spectral region, but their output is representative of a limited portion of the water column, which limits their expressiveness for oligo- to mesotrophic waters. On the other hand, the accuracy of algorithms using a larger portion of the spectra will suffer much more from the spectral variations in the light penetration depth, even though they carry information on a larger portion of the water column and have thereby a higher value for the water quality monitoring.

What is the most suited atmospheric correction for Sentinel-2 over clear and dark inland waters?

From the results of this study we draw the following observations: (i) c2rcc and Polymer give the best results overall with an advantage for Polymer regarding the ability to accurately retrieve the spectral shape of the R_{rs} (ii) The SWIR setup with a per-pixel determination of ϵ (iii) c2rcc and Polymer resolve well situations contaminated with cirrus and glint but suffer from adjacency effect, (iv) The response of iCor and ACOLITE to environmental factor is antagonist to c2rcc and Polymer, (iv) the assumption of spatial homogeneity of the aerosol optical depth is invalid in the peri-alpine region, (v) iCor displays the largest error.

5. 2. Outlook

In this thesis we developed a method to identify and monitor calcite precipitation events but we didn't provide a quantitative description of the phenomenon. Based on the proposed procedure, the development of a systematic detection scheme for whitening events would extend the reach of our study. In fact, whitening events are not yet fully understood and real-time detection of such event from remote observations would allow researchers to adapt in-situ sampling. We further show that calcite precipitation in Lake Geneva is a major term in the carbon budget and a systematic detection scheme will develop our understanding of the role of inland waters in the carbon cycle. In the context of this thesis we showed some potential implications on the accurate interpretation of the remote sensing signal (Chapter 4). The integration of such peculiar events in terms of optical properties into inversion routines could therefore promote new applications. This is especially relevant in Lake Geneva since a platform will be deployed for the next 10 years near the north-east shore of the lake, an area especially

sensitive to calcite precipitation events. The continuous measurements of IOPs, AOPs, and other relevant parameters will further improve the current understanding of the connections between the IOPs and the optically significant constituents in Lake Geneva. The IOPs and the bio-optical model used to assess the impact of vertical non-uniformities of water constituents gave satisfactory results in terms of optical closing but continuous measurements could improve the parametrization of these models for Lake Geneva. In particular, better knowledge of vertical gradients in CDOM are needed. One important follow up of the study is the ongoing implementation of the vertical approximation models in a LUT designed for the interpretation of Sentinel-2 observations over Lake Geneva.

At a coarser scale, we identified one major constraint for the accurate interpretation of remote observations over oligo- to mesotrophic waters. The current focus of the community is the resolution of the mixed signal in turbid waters but clearer lakes raise challenges that also require the attention of the community. We showed that in Lake Geneva the traditional uniform assumption is a major source of error in the interpretation of remote observations and we propose simple vertical approximation models to account for this error (Chapter 3). This procedure, which is based on data assimilation between remote sensing and ecological and/or hydrodynamic models, is a realistic way to cope with an issue barely considered by the community and often considered unachievable.

Another important source of errors for remote sensing is the atmospheric correction method used in the processing. In this thesis we provide an evaluation of four atmospheric correction models but our recommendations are valid only for Lake Geneva and maybe other lakes in the peri-alpine region. This supposition, however, require actual measurements in different lakes to be converted to a statement, and additional research is required.

To extend the findings of this thesis, it is necessary for the community to coordinate validation efforts over a wider geographical setting. The LIMNADES database is a promising initiative from the Global Observatory of Lake Responses to Environmental Change (GloboLakes) to share validation dataset at an International level. Such database, when operational will greatly benefit the community and needs to be promoted.

References

- Allan, J.D., McIntyre, P.B., Smith, S., Alpern, B.S., Boyer et al., 2013. Joint analysis of stressors and ecosystem services to enhance restoration effectiveness. *Proceedings of the National Academy of Science*, 110:372-377
- Andréfouët, S., Riegl, B., 2004. Remote sensing: A key tool for interdisciplinary assessment of coral reef processes. *Coral Reefs*, 23:1-4. 10.1007/s00338-003-0360-z.
- Anneville, O., Pelletier, J.P., 2000. Recovery of Lake Geneva from eutrophication: quantitative response of phytoplankton. *Arch. Für Hydrobiol. – Hauptbände*, 148:607–624.
- Anneville, O., Ginot, V., Angeli, N., 2002a. Restoration of Lake Geneva: expected versus observed responses of phytoplankton to decreases in phosphorus. *Lakes & Reservoirs: Research & Management*, 7(2):67–80.
- Anneville, O., Souissi, S., Ibanez, F., Ginot, V., Druart, J.C., Angeli, N., 2002b. Temporal mapping of phytoplankton assemblages in Lake Geneva: annual and interannual changes in their patterns of succession. *Limnol. Oceanogr.*, 47:1355–1366.
- Babin, M., Morel, A., Fournier-Sicre, V., Fell, F., Stramski, D., 2003. Light scattering properties of marine particles in coastal and open ocean waters as related to the particle mass concentration. *Limnol. Ocean.*, 48:843–859.
- Berthon, J.-F., Shybanov, E., Lee, M.E.-G., Zibordi, G., 2007. Measurements and modeling of the volume scattering function in the coastal northern Adriatic Sea. *Appl. Opt.*, 46:5189–5203.
- Bierman, P., Lewis, M., Ostendorf, B., Tanner, J., 2011. A review of methods for analysing spatial and temporal patterns in coastal water quality. *Ecological Indicators*, 11:103-114.
- Blanc, P., Pelletier, J.P., Moille, J.P., 1993. Variabilité spatiale et temporelle des paramètres physico-chimiques et biologiques dans les eaux du Léman. *Rapp. Comm. int. prot. eaux Léman contre pollut., campagne 1992*, pp 113-162 and 162b-162p.
- Bouffard, D., Lemmin, U., 2013. Kelvin waves in Lake Geneva. *J. Great Lakes Res.*, 39:637–645. <https://doi.org/10.1016/j.jglr.2013.09.005>.
- Bouffard, D., Perga, M.-E., 2016. Are flood-driven turbidity currents hot spots for priming effect in lakes? *Biogeosciences*, 13:3573–3584.
- Bouffard, D., Kiefer, I., Wüest, A., Wunderle, S., Odermatt, D., 2018. Are surface temperature and chlorophyll in a large deep lake related? An analysis based on satellite observations in synergy with hydrodynamic modelling and in-situ data. *Remote Sens. Environ.*, 209:510–523. <https://doi.org/10.1016/j.rse.2018.02.056>.

- Boss, E., Pegau, W.S., 2001. Relationship of light scattering at an angle in the backward direction to the backscattering coefficient. *Appl. Opt.*, 40:5503–5507.
- Brando, V.E., Robson, B.J., Cherukuru, N.R.C., Dekker, A.G., Webster, I.T., 2007. Towards assimilation of ocean colour satellite observation into coastal ocean biogeochemical models: the tropical Fitzroy River Estuary case study – art. no. 66850D. Zou, X., Barker, D., LeDimet, F.X. (Eds.), *Assimilation of Remote Sensing and In Situ Data in Modern Numerical Weather and Environmental Prediction Models*, Proceedings of the Society of Photo-optical Instrumentation Engineers (SPIE) 6685, pp D6850.
- Bresciani, M., Cazzaniga, I., Austoni, M., Sforzi, T., Buzzi, F., Morabito, G., Giardino, C., 2018. Mapping phytoplankton blooms in deep subalpine lakes from Sentinel-2A and Landsat-8. *Hydrobiologia*, pp 1-18. <https://doi.org/10.1007/s10750-017-3462-2>.
- Brezonik, P., Menken, K. D., Bauer, M., 2005. Landsat-based remote sensing of lake water quality characteristics, including chlorophyll and Colored Dissolved Organic Matter (CDOM). *Lake and Reservoir Management*, 21(4):373–82. <https://doi.org/10.1080/07438140509354442>.
- Bricaud, A., Morel, A., 1986. Light attenuation and scattering by phytoplanktonic cells: a theoretical modeling. *Appl. Opt.*, 25:571. <https://doi.org/10.1364/AO.25.000571>.
- Bricaud, A., Roesler, C., Zaneveld, J.R.V., 1995. In situ methods for measuring the inherent optical properties of ocean waters. *Limnol. Oceanogr.*, 40:393–410.
- Brockmann, C., Doerffer, R., Peters, M., Stelzer, K., Embacher, S., Ruescas, A., 2016. Evolution of the C2RCC neural network for Sentinel 2 and 3 for the retrieval of ocean colour products in normal and extreme optically complex waters. *Proc. Living Planet Symposium*, ESA SP-470.
- Bukata, R.P., Jerome, J.H., Bruton, J.E., Bennett, E., 1978. Relationship among optical transmission, volume reflectance, suspended sediment concentration, and chlorophyll-a concentration in Lake Superior. *J. Great Lakes Res.*, 4:456–461.
- Bukata R.P., 2013. Retrospection and introspection on remote sensing of inland water quality: “Like deja vu all over again”. *J. Great Lakes Res.*, 39:2–5.
- Burkard, P., 1984. Hydrologie – Bilan hydrologique. In: *Comm. int. protection des eaux du Léman*, Lausanne: Le Léman Synthèse 1957–1982, pp 43–48.
- Chen, C. T., Millero, F.J., 1986. Thermodynamic properties for natural waters covering only the limnological range. *Limnol. Oceanogr.*, 31(3):657–662.
- Churnside, J.H., 2015. Bio-optical model to describe remote sensing signals from a stratified ocean. *J. Appl. Remote Sens.*, 9(1) :095989, doi:10.1117/1.JRS.9.095989.
- CIPEL, 2015. Rapports sur les études et recherches entreprises dans le bassin Lémanique, campagne 2014. Commission internationale pour la protection des eaux du Léman contre la pollution - CIPEL (Nyon, Switzerland).

- Coleman, T., Branch, M.A., Grace, A., 1999. Matlab optimization toolbox user's guide. Third ed. Math Works, Natick.
- Cubero-Castan, M., Constantin, D., Barbieux, K., Nouchi, V., Akhtman, Y., Merminod, B., 2015. A new smoothness based strategy for semi-supervised atmospheric correction: Application to the léman-Baïkal campaign, *Hyperspectral Image and Signal Processing: Evolution in Remote Sensing (WHISPERS) 2015 7th Workshop on*, pp 1-4, ISSN 2158-6276.
- Curtarelli, M.P., Ogashawara, I., Alcântara, E.H., Stech, J.L., 2015. Coupling remote sensing bio-optical and three-dimensional hydrodynamic modeling to study the phytoplankton dynamics in a tropical hydroelectric reservoir. *Remote Sens. of Environ.*, 157:185–198.
- Dall'Olmo, G., Westberry, T. K., Behrenfeld, M. J., Boss, E., Slade, W. H., 2009. Significant contribution of large particles to optical backscattering in the open ocean, *Biogeosciences*, 6:947–967, doi:10.5194/bg-6-947-2009.
- Dekker, A.G., Peters, S.W.M., 1993. The use of the Thematic Mapper for the analysis of eutrophic lakes: a case study in the Netherlands. *Int. J. Remote Sens.*, 14(5):799–821. <https://doi.org/10.1080/01431169308904379>.
- Del Vecchio, R., Blough, N.V., 2002. Photobleaching of chromophoric dissolved organic matter in natural waters: kinetics and modeling. *Mar. Chem.*, 78:231–253.
- Dennison, P.E., Halligan, K.Q., Roberts, D.A., 2004. A comparison of error metrics and constraints for multiple endmember spectral mixture analysis and spectral angle mapper. *Remote Sens. Environ.*, 93:359–367.
- Doerffer, R., Fischer, J., 1994. Concentrations of chlorophyll, suspended matter, and gelbstoff in case II waters derived from satellite coastal zone color scanner data with inverse modeling methods, *J. Geophys. Res.*, 99(C4):7457–7466.
- Doerffer, R., Schiller, H., 2007. The MERIS Case 2 water algorithm. *Int. J. Remote Sens.*, 28:517–535. <https://doi.org/10.1080/01431160600821127>.
- Dokulil, M.T., and Teubner, K., 2012. Deep living *Planktothrix rubescens* modulated by environmental constraints and climate forcing. *Hydrobiologia*, 698:29–46.
- Dominik, J., Dulinski, M., Span, D., Hofmann, A., Favarger, P.Y., Vernet, J.P., 1993. Transfert de matière et de radio-isotopes entre l'eau et les sédiments dans le Léman. Tech. rep.. Commission Internationale Pour la Protection des Eaux du Léman (CIPEL).
- Doxani, G., Vermote, E., Roger, J., Gascon, F., Adriaensen, S., Frantz, D., & Kirches, G., 2018. Atmospheric correction inter-comparison exercise. *Remote Sens.*, 10 :1–18.
- Erga, S.R., Ssebiyonga, N., Hamre, B., Frette, Ø., Hovland, E., Hancke, K., Drinkwater, K., Rey, F., 2014. Environmental control of phytoplankton distribution and photosynthetic performance at the Jan Mayen Front in the Norwegian Sea. *J. Mar. Syst.*, 130:193–205.

- Finger, D., Schmid, M., Wüest, A., 2006. Effects of upstream hydropower operation on riverine particle transport and turbidity in downstream lakes. *Water Resources Research*, 42(8):W08429. <https://doi.org/10.1029/2005WR004751>.
- Forel, F.A., 1892. *Le Léman : monographie limnologique*. F. Rouge, éditeur, Libraire de l'Université. <https://doi.org/10.3931/e-rara-49502>.
- Fournier, G.R., Forand, J.L., 1994. Analytic phase function for ocean water. In *Ocean Optics XII*, (International Society for Optics and Photonics), pp 194–201.
- Gege, P., 2000. Gaussian model for yellow substance absorption spectra. In *Proc. Conference of Ocean Optics XV*, (Monaco), pp 9.
- Gege, P., 2014. WASI-2D: A software tool for regionally optimized analysis of imaging spectrometer data from deep and shallow waters. *Comput. Geosci.*, 62:208–215.
- Gholamalifard, M., Esmaili-Sari, A., Abkar, A., Naimi, B., Kutser, T., 2013. Influence of vertical distribution of phytoplankton on remote sensing signal of Case II waters: southern Caspian Sea case study. *J. Appl. Remote Sens.*, 7(1):073550, doi:10.1117/1.JRS.7.073550.
- Giardino, C., Brando, V.E., Dekker, A.G., Strömbeck, N., Candiani, G., 2007. Assessment of water quality in Lake Garda (Italy) using Hyperion. *Remote Sens. Environ.*, 109:183–195.
- Giardino, C., Bresciani, M., Cazzaniga, I., Schenk, K., Rieger, P., Braga, F., Matta, E., Brando, V., 2014. Evaluation of multi-resolution satellite sensors for assessing water quality and bottom depth of Lake Garda. *Sensors*, 14:24116–24131.
- Gitelson, A., Szilagyi, F., Mittenzwey, K.-H., 1993. Quantitative Remote Sensing Methods for Real-time Monitoring of Inland Water Quality. *Int. J. Remote Sens.*, 14:1269-1295.
- Gleick, P.H., 1996. Water resources. In S.H. Schneider (ed.), *Encyclopedia of Climate and Weather*, New York: Oxford University Press, pp 817-823.
- Gons, H.J., 2002. A chlorophyll-retrieval algorithm for satellite imagery (Medium Resolution Imaging Spectrometer) of inland and coastal waters. *J. Plankton Res.*, 24:947–951.
- Gons, H.J., 2005. Effect of a waveband shift on chlorophyll retrieval from MERIS imagery of inland and coastal waters. *J. Plankton Res.*, 27:125–127.
- Gons, H.J., Auer, M.T., Effler, S.W., 2008. MERIS satellite chlorophyll mapping of oligotrophic and eutrophic waters in the Laurentian Great Lakes. *Remote Sens. Environ.*, 112:4098–4106.
- Gordon, H.R., McCluney, W.R., 1975. Estimation of the depth of sunlight penetration in the sea for remote sensing. *Appl. Opt.*, 14:413–416.
- Gordon, H. R., 1978. Removal of atmospheric effects from satellite imagery of the oceans. *Appl. Opt.*, 17:1631–1636.

- Gordon, H.R., Clark, D.K., 1980. Remote sensing optical properties of a stratified ocean: an improved interpretation. *Appl. Opt.*, 19:3428- 3430.
- Gordon, H.R., Brown, O.B., Evans, R.H., Brown, J.W., Smith, R.C., Baker, K.S., Clark, D.K., 1988. A semianalytic radiance model of ocean color. *J. Geophys. Res.*, 93:10909–10924.
- Gordon, H. R., Wang, M., 1994. Retrieval of water-leaving radiance and aerosol optical thickness over the oceans with SeaWiFS: a preliminary algorithm, *Appl. Opt.*, 33:443–452.
- Gordon, H.R, Du, T., Zhang, T., 1997. Remote sensing ocean color and aerosol properties: Resolving the issue of aerosol absorption, *Appl. Opt.*, 36:8670-8684.
- Graham, N.D., Bouffard, D., Loizeau, J.-L., 2016. The influence of bottom boundary layer hydrodynamics on sediment focusing in a contaminated bay. *Environ. Sci. Pollut. Res.*, 23 :25412–25426. <https://doi.org/10.1007/s11356-016-7715-9>.
- Green, R.E., Bower, A.S., Lugo-Fernández, A., 2014. First Autonomous Bio-Optical Profiling Float in the Gulf of Mexico reveals dynamic biogeochemistry in deep waters. *PLOS ONE* 9, pp e101658.
- Guanter, L., Del Carmen González-Sanpedro, M., Moreno, J., 2007. A method for the atmospheric correction of ENVISAT/MERIS data over land targets. *Int. J. Remote Sens.*, 28:3-4 and 709-728.
- Halpern, B.S., Walbridge, S., Selkoe, K.A., et al., 2008. A global map of human impact on marine ecosystems. *Science*, 319:948–952.
- Hauenstein, W., Dracos, T., 1984. Investigation of plunging density currents generated by inflows in lakes. *J. Hydraul. Res.*, 22:157–179. doi:10.1080/00221688409499404.
- Hedley, J.D., Roelfsema, C.M., Chollett, I., Harborne, A.R., Heron, S.F., Weeks, S., Skirving, W.J., Strong, A.E., Eakin, C.M., Christensen, T.R., 2016. Remote sensing of coral reefs for monitoring and management: a review. *Remote Sens.*, 8:118.
- Heege, T., Fischer, J., 2004. Mapping of water constituents in Lake Constance using multispectral airborne scanner data and a physically based processing scheme. *Can. J. Remote Sens.*, 30:77–86.
- Hieronymi, M., Krasemann, H., Müller, D., Brockmann, C., Ruescas, A., Stelzer, K., et al., 2016. Ocean colour remote sensing of extreme case-2 waters. In *Proceedings of Living Planet Symposium*, Prague, ESA, SP-740.
- Hochberg, E.J.; Atkinson, M.J., 2003. Capabilities of remote sensors to classify coral, algae, and sand as pure and mixed spectra. *Remote Sens. Environ.*, 85:174–189.
- Hu, C., Carder, K.L., Muller-Karger, F.E., 2000. Atmospheric correction of SeaWiFS imagery over turbid coastal waters: A practical method. *Remote Sens. Environ.*, 74:195-206.
- INRA, CIPEL, 2016. Long-term Observation and Experimentation System for Environmental Research - Alpine Lake Observatory (SOERE-OLA). www.si-ola.inra.fr, accessed 22 November 2016.

- IOCCG, 2000. Remote Sensing of Ocean Colour in Coastal, and Other Optically-Complex, Waters. Sathyendranath, S. (ed.), Reports of the International Ocean-Colour Coordinating Group, 3, IOCCG.
- IOCCG, 2006. Remote Sensing of Inherent Optical Properties: Fundamentals, tests of algorithms, and applications. Lee, Z.-P. (ed.), Reports of the International Ocean-Colour Coordinating Group, 5, IOCCG.
- IOCCG, 2010. Atmospheric correction for remotely-sensed ocean-colour products, Reports of the International Ocean-Colour Coordinating Group, 10, IOCCG.
- ISO 7027-1, 2016. Water quality - Determination of turbidity - Part 1: Quantitative methods.
- Jerlov, N.G., 1961. Optical measurements in the eastern North Atlantic, *Medd. Oceanogr. Inst. Göteborg*, 30:1-40.
- Jupp, D.L.B., Kirk, J.T.O., Harris, G.P., 1994. Detection, identification and mapping of cyanobacteria – using remote sensing to measure the optical quality of turbid inland waters. *Australian Journal of Marine and Freshwater Research*, 45:801–828.
- Kallio, K., Attila, J., Härmä, P., Koponen, S., Pulliainen, J., Hyytiäinen, M.J., Pyhälähti, T., 2008. Landsat ETM+ images in the estimation of seasonal lake water quality in boreal river basins. *Environmental Management*, 42(3):511-22. <https://doi.org/10.1007/s00267-008-9146-y>.
- Kallio, K., 2012. Water quality estimation by optical remote sensing in boreal lakes. Doctoral dissertation, University of Helsinki.
- Kiefer, I., Odermatt, D., Anneville, O., Wüest, A., Bouffard, D., 2015. Application of remote sensing for the optimization of in-situ sampling for monitoring of phytoplankton abundance in a large lake. *Sci. Total Environ.*, 527-528, 493- 506. <https://doi.org/10.1016/j.scitotenv.2015.05.011>.
- Kruse F.A., Lefkoff A.B., Boardman J.W., Heidebrecht K.B., Shapiro A.T., Barloon P.J., et al., 1993. The spectral image processing system (SIPS) — Interactive visualization and analysis of imaging spectrometer data. *Remote Sens. Environ.*, 44.
- Kutser, T., Vahtmäe, E., Martin, G., 2006. Assessing suitability of multispectral satellites for mapping benthic macroalgal cover in turbid coastal waters by means of model simulations. *Estuarine, Coastal and Shelf Science*, 67(3):521-29. <https://doi.org/10.1016/j.jecss.2005.12.004>.
- Kutser, T., Metsamaa, L., Dekker, A.G., 2008. Influence of the vertical distribution of cyanobacteria in the water column on the remote sensing signal. *Estuar. Coast. Shelf Sci.*, 78:649–654.
- Kutser, T. 2009. Passive optical remote sensing of cyanobacteria and other intense phytoplankton blooms in coastal and inland waters. *Int. J. Remote Sens.*, 30:4401–4425.
- Kutser, T., 2012. The possibility of using the Landsat image archive for monitoring long time trends in coloured dissolved organic matter concentration in lake waters. *Remote Sens. Environ.*, 123:334-38. <https://doi.org/10.1016/j.rse.2012.04.004>.

- Kutser, T., Verpoorter, C., Paavel, B., Tranvik, L.J., 2015. Estimating lake carbon fractions, remote sensing data. *Remote Sens. Environ.*, 157:138–146, <http://dx.doi.org/10.1016/j.rse.2014.05.020>.
- Kutser, T., Paavel, B., Verpoorter, C., Ligi, M., Soomets, T., Toming, K., Casal, G., 2016. Remote sensing of black lakes and using 810 nm reflectance peak for retrieving water quality parameters of optically complex waters. *Remote Sens.*, 8(6):497. <https://doi.org/10.3390/rs8060497>.
- Lambert, A., Giovanoli, F., 1988. Records of riverborne turbidity currents and indications of slope failures in the Rhone delta of Lake Geneva. *Limnol. Oceanogr.*, 33(3):458–468.
- Lee, Z.P., Carder, K.L., Arnone, R.A., 2002. Deriving inherent optical properties from water color: A multiband quasi-analytical algorithm for optically deep waters. *Appl. Opt.*, 41:5755–5772.
- Lee, M.E., Lewis, M.R., 2003. A new method for the measurement of the optical volume scattering function in the upper ocean. *J. Atmos. Oceanic Tech.*, 20:563–571.
- Lee, J.-Y., Kim, J.-K., Owen, J.S., Choi, Y., Shin, K., Jung, S., Kim, B., 2013. Variation in carbon and nitrogen stable isotopes in POM and zooplankton in a deep reservoir and relationship to hydrological characteristics. *J. Freshw. Ecol.*, 28:47–62.
- Lee, Z., Wei, J., Voss, K., Lewis, M., Bricaud, A., Huot, Y., 2015. Hyperspectral absorption coefficient of “pure” seawater in the range of 350–550 nm inverted from remote sensing reflectance. *Appl. Opt.*, 54(3):546–558, doi: 10.1364/AO.54.000546.
- Lee, Z., Shang, S., Qi, L., Yan, J., Lin, G., 2016. A semi-analytical scheme to estimate Secchi-disk depth from Landsat-8 measurements. *Remote Sens. Environ.*, 177:101–106. <https://doi.org/10.1016/j.rse.2016.02.033>.
- Lenoble, J., Herman, M., Deuzé, J., Lafrance, B., Santer, R., Tanré, D., 2007. A successive order of scattering code for solving the vector equation of transfer in the Earth’s atmosphere with aerosols. *Journal of Quantitative Spectroscopy and Radiative Transfer*, 107:479–507.
- Levy, R., Hsu, C., et al., 2015. MODIS Atmosphere L2 Aerosol Product. NASA MODIS Adaptive Processing System, Goddard Space Flight Center, USA: http://dx.doi.org/10.5067/MODIS/MOD04_L2.006.
- Lewis, M.R., Cullen, J.J., Platt, T., 1983. Phytoplankton and thermal structure in the upper ocean: Consequences of nonuniformity in chlorophyll profile. *J. Geophys. Res. Oceans*, 88:2565–2570.
- Liu, H., Li, Q., Shi, T., Hu, S., Wu, G., Zhou, Q., 2017. Application of sentinel 2 MSI images to retrieve suspended particulate matter concentrations in Poyang Lake. *Remote Sens.*, 9 :761.
- Loizeau, J.-L., Gitardclos, S., Dominik, J., 2012. Taux d’accumulation des sédiments récents et bilan de la matière particulaire dans le Léman (Suisse-France). *Arch. Sci.*, 65:81–92
- Lotter, A.F., Sturm, M., Teranes, J.L., Wehrli, B., 1997. Varve formation since 1885 and high-resolution varve analyses in hypertrophic Baldeggersee (Switzerland). *Aquat. Sci.*, 59:304–325. doi:10.1007/BF02522361.

- Martins, V.S., Barbosa, C.C.F., de Carvalho, L.A.S., Jorge, D.S.F., Lobo, F.d.L., Novo, E.M.L.d.M., 2017. Assessment of atmospheric correction methods for sentinel-2 MSI images applied to amazon floodplain lakes. *Remote Sens.*, 9:322
- Matthews, M.W., 2011. A current review of empirical procedures of remote sensing in inland and near-coastal transitional waters. *Int. J. Remote Sens.*, 32:6855–6899.
- Matthews, M.W., Bernard, S., 2013. Using a two-layered sphere model to investigate the impact of gas vacuoles on the inherent optical properties of *M. aeruginosa*, *Biogeosciences*, 10:813–98157.
- McCulloch, A.A., Kamykowski, D., Morrison, J.M., Thomas, C.J., Pridgen, K.G., 2013. A physical and biological context for *Karenia brevis* seed populations on the northwest Florida shelf during July 2009. *Cont. Shelf Res.*, 63:94–111.
- Miller, R.L., Mckee, B.A., 2004. Using MODIS Terra 250 m imagery to map concentrations of total suspended matter in coastal waters. *Remote Sens. Environ.*, 93:259–266.
- Mobley, C.D., 1994. *Light and Water* (San Diego, USA: Academic Press).
- Mobley, C.D., 1999. Estimation of the remote-sensing reflectance from above-surface measurements. *Appl. Opt.*, 38:7442-7745.
- Mobley, C.D., Sundman, L.K., Boss, E., 2002. Phase function effects on oceanic light fields, *Appl. Opt.*, 41(6):1035-1050.
- Mobley, C.D., Sundman, L.K., 2016. *HydroLight 5.3 - EcoLight 5.3 Technical Documentation* (Bellevue, United States: Sequoia Scientific, Inc.).
- Montes-Hugo, M.A., Churnside, J.H., Gould, R.W., Arnone, R.A., Foy, R., 2010. Spatial coherence between remotely sensed ocean color data and vertical distribution of lidar backscattering in coastal stratified waters. *Remote Sens. Environ.*, 114:2584–2593.
- Moore, T.S., Dowell, M.D., Bradt, S., Verdu, A.R., 2014. An optical water type framework for selecting and blending retrievals from bio-optical algorithms in lakes and coastal waters. *Remote Sens. Environ.*, 143:1-15.
- Morel, A., 1988. Optical modeling of the upper ocean in relation to its biogenous matter content (case I waters). *J. Geophys. Res.*, 93:10749–10768.
- Morel, A., Maritorena, S., 2001. Bio-optical properties of oceanic waters: a reappraisal. *J. Geophys. Res.*, 106 (C4):7163–7180.
- Moses, W.J., Ackleson, S.G., Hair, J.W., Hostetler, C.A., Miller, W.D., 2016. Spatial scales of optical variability in the coastal ocean: Implications for remote sensing and in situ sampling.. *J. Geophys. Res. Oceans*, 121:4194–4208.
- Mouw, C., Greb, S., Aurin, D., DiGiacomo, P., Lee, Z., Twardowski, M., et al., 2015. Aquatic color radiometry remote sensing of coastal and inland waters: Challenges and recommendations for future satellite missions. *Remote Sens. Environ.*, 160:15-30.

- Mueller, J.L., McClain, NASA, 2003. Ocean optics protocols for satellite ocean color sensor validation, revision 4, vol. III: radiometric measurements and data analysis protocols, NASA/TM-2003-211621.
- Nechad, B., Ruddick, K.G., Park, Y., 2010. Calibration and validation of a generic multisensor algorithm for mapping of total suspended matter in turbid waters. *Remote Sens. Environ.*, 114(4):854-866.
- Nelder, J.A., Mead, R. 1965. A Simplex Method for Function Minimization. *Comput. J.*, 7:308–313.
- Neukermans, G., Ruddick, K., Loisel, H., Roose, P., 2012. Optimization and quality control of suspended particulate matter concentration measurement using turbidity measurements. *Limnol. Oceanogr. Methods*, 10:1011–1023.
- Niessen, F., Sturm, M., 1987. The sediments of Lake Baldegg (Switzerland)—sedimentary environment and development of eutrophication for the last 100 yr. (in German, with English abstract). *Arch. Hydrobiol.*, 108:365–383. doi:10.4319/lo.2005.50.3.0914/pdf.
- Nouchi, V., Odermatt, D., Wüest, A., Bouffard, D., Effects of non-uniform vertical constituent profiles on remote-sensing reflectance of oligo- to mesotrophic lakes. Submitted to *European Journal of Remote Sensing* on October 2017.
- Obst, M., Wehrli, B., Dittrich, M., 2009. CaCO₃ nucleation by cyanobacteria: laboratory evidence for a passive, surface-induced mechanism. *Geobiology*, 7(3):324-347. <https://doi.org/10.1111/j.1472-4669.2009.00200.x>.
- Odermatt, D., Giardino, C., Heege, T., 2010. Chlorophyll retrieval with MERIS Case-2-Regional in perialpine lakes. *Remote Sens. Environ.* 114 :607–617. <https://doi.org/10.1016/j.rse.2009.10.016>.
- Odermatt, D., Gitelson, A., Brando, V.E., Schaepman, M.E., 2012. Review of constituent retrieval in optically deep and complex waters from satellite imagery. *Remote Sens. Environ.*, 118:116–126.
- Oishi, T., 1990. Significant relationship between the backward scattering coefficient of sea water and the scatterance at 120°. *Appl. Opt.*, 29:4658–4665.
- Olmanson, L., Marvin, G., Bauer, E., Brezonik, P., 2008. A 20-year Landsat water clarity census of Minnesota's 10,000 Lakes. *Remote Sens. Environ.*, 112(11):4086-4097. <https://doi.org/10.1016/j.rse.2007.12.013>.
- Pahlevan, N., Garret, A., Gerace, A.D., Schott, J.R., 2012. Integrating Landsat 7 imagery with physics-based models for quantitative mapping of coastal waters near river discharges. *Photogramm. Eng. Remote Sensing (PE&RS)*, 78:11.
- Pahlevan, N., Lee, Z., Wei, J., Schaaf, C.B., Schott, J.R., Berk, A., 2014. On-Orbit Radiometric Characterization of OLI (Landsat-8) for Applications in Aquatic Remote Sensing. *Remote Sens. Environ.*, 154:272-284. <https://doi.org/10.1016/j.rse.2014.08.001>.

- Pahlevan, N.; Sarkar, S.; Franz, B.A.; Balasubramanian, S.V., He, J., 2017. Sentinel-2 MultiSpectral Instrument (MSI) data processing for aquatic science applications: Demonstrations and validations. *Remote Sens. Environ.*, 201:47–56.
- Palmer, S.C.J., Kutser, T., Hunter, P.D., 2015. Remote sensing of inland waters: Challenges, progress and future directions. *Remote Sens. Environ.*, 157 :1–8. <https://doi.org/10.1016/j.rse.2014.09.021>.
- Petzold, T.J., 1972. Volume scattering functions for selected ocean waters. *Scripts Inst. Oceanogr. Report SIO*, pp 72-78.
- Pfannkuche, J., Schmidt, A., 2003. Determination of suspended particulate matter concentration from turbidity measurements: particle size effects and calibration procedures. *Hydrol. Process.*, 17:1951–1963.
- Piskozub, J., Neumann, T., Wozniak, L., 2008. Ocean color remote sensing: Choosing the correct depth weighting function. *Opt. Express*, 16:14683–14688.
- Pitarch, J., Odermatt, D., Kawka, M., Wüest, A., 2014. Retrieval of vertical particle concentration profiles by optical remote sensing: a model study. *Opt. Express*, 22(S3):A947–A959. doi: 10.1364/OE.22.00A947.
- Pitarch, J., Volpe, G., Colella, S., Santoleri, R., Brando, V., 2016. Absorption correction and phase function shape effects on the closure of apparent optical properties. *Appl. Opt.*, 55:8618–8636.
- Plée, K., Pacton, M., Ariztegui, D., 2010. Discriminating the role of photosynthetic and heterotrophic microbes triggering low-Mg calcite precipitation in freshwater biofilms (Lake Geneva, Switzerland). *Geomicrobiol. J.*, 27(5):391–99. <https://doi.org/10.1080/01490450903451526>.
- Plummer, L.N., Busenberg, E., 1982. The solubilities of calcite, aragonite and vaterite in CO₂-H₂O solutions between 0 and 90°C, and an evaluation of the aqueous model for the system CaCO₃-CO₂-H₂O. *Geochim. Cosmochim. Acta*, 46(6):1011–1040. [https://doi.org/10.1016/0016-7037\(82\)90056-4](https://doi.org/10.1016/0016-7037(82)90056-4).
- Pope, R.M., Fry, E.S., 1997. Absorption spectrum (380–700 nm) of pure water. II. Integrating cavity measurements. *Appl. Opt.*, 36:8710–8723.
- Preisendorfer, R.W., 1961. Application of radiative transfer theory to light measurements in the sea. *International Union of Geodesy and Geophysics Monograph*, pp 11-29.
- Råman Vinnå, L., Wüest, A., Bouffard, D., 2017a. Physical effects of thermal pollution in lakes. *Water Resour. Res.*, 53:3968–3987. <https://doi.org/10.1002/2016WR019686>.
- Råman Vinnå, L., Wüest, A., Zappa, M., Fink, G., Bouffard, D., 2017b. Tributaries affect the thermal response of lakes to climate change. *Hydrol. Earth Syst. Sci.*, 22(1):31-51. <https://doi.org/10.5194/hess-2017-337>.
- Ramisch, F., Dittrich, M., Mattenberger, C., Wehrli, B., Wüest, A., 1999. Calcite dissolution in two deep eutrophic lakes. *Geochim. Cosmochim. Acta*, 63:3349–3356.

- Rapin, F., Blanc, P., Corvi, C., 1989. Influence des apports sur le stock de phosphore dans le lac Léman et sur son eutrophisation. *Rev. Sci. Eau*, 2:721–737.
- Razmi, A.M., Barry, D.A., Bakhtyar, R., Le Dantec, N., Dastgheib, A., Lemmin, U., Wüest, A., 2013. Current variability in a wide and open lacustrine embayment in Lake Geneva (Switzerland). *J. Gt. Lakes Res.*, 39:455–465.
- Razmi, A.M., Barry, D.A., Lemmin, U., Bonvin, F., Kohn, T., Bakhtyar, R., 2014. Direct effects of dominant winds on residence and travel times in the wide and open lacustrine embayment: Vidy Bay (Lake Geneva, Switzerland). *Aquat. Sci.*, 76(Suppl 1): S59–S71.
- Reynolds, R.A., Stramski, D., Wright, V.M., Wozniak, S.B., 2010. Measurements and characterization of particle size distributions in coastal waters, *J. Geophys. Res. Oceans*, 115:C08024.
- Ruzycki, E.M., Axler, R.P., Host, G.E., Henneck, J.R., Will, N.R., 2014. Estimating sediment and nutrient loads in four Western Lake Superior streams. *JAWRA J. Am. Water Resour. Assoc.*, 50:1138–1154.
- Ryan, J.P., Davis, C.O., Tufillaro, N.B., Kudela, R.M., Gao, B.-C., 2014. Application of the Hyper-spectral Imager for the coastal ocean to phytoplankton ecology studies in Monterey Bay, CA, USA. *Remote Sens.*, 6:1007–1025.
- Santer, R., Schmechtig, C., 2000. Adjacency effects on water surfaces: Primary scattering approximation and sensitivity study. *Appl. Opt.*, 39:361–375.
- Sastre, V., Loizeau, J.-L., Greinert, J., Naudts, L., Arpagaus, P., Anselmetti, F., Wildi, W., 2010. Morphology and recent history of the Rhone River Delta in Lake Geneva (Switzerland). *Swiss J. Geosci.*, 103:33–42. doi:10.1007/s00015-010-0006-4.
- Schaeffer, B.A., Schaeffer, K.G., Keith, D., Lunetta, R.S., Conmy, R., Gould, R.W., 2013. Barriers to adopting satellite remote sensing for water quality management. *Int. J. Remote Sens.*, 34 (21):7534–7544.
- Schwefel, R., Gaudard, A., Wüest, A., Bouffard, D., 2016. Effects of climate change on deepwater oxygen and winter mixing in a deep lake (Lake Geneva): Comparing observational findings and modeling: climate change effect in a deep lake. *Water. Resour. Res.*, 52:8811–8826. <https://doi.org/10.1002/2016WR019194>.
- Siegel, D.A., Wang, M., Maritorena, S., Robinson, W., 2000. Atmospheric correction of satellite ocean color imagery: The black pixel assumption. *Appl. Opt.*, 39:3582–3591.
- Simis, S.G.H., Peters, S.W.M., Gons, H.J., 2005. Remote sensing of the cyanobacterial pigment phycocyanin in turbid inland water. *Limnol. Oceanogr.*, 50:237–245.
- Simis, S.G.H., Ruiz-Verdú, A., Dominguez-Gomez, J.A., Pena-Martinez, R., Peters, S.W.M. and Gons, H.J., 2007. Influence of phytoplankton pigment composition on remote sensing of cyanobacterial biomass. *Remote Sens. Environ.*, 106:414–427.

- Slonecker, E.T., Jones, D.K., Pellerin, B.A., 2016. The new Landsat 8 potential for remote sensing of Colored Dissolved Organic Matter (CDOM). *Marine Pollution Bulletin*, 107(2):518-27. <https://doi.org/10.1016/j.marpolbul.2016.02.076>.
- [dataset] SOERE OLA-IS, INRA Thonon-les-Bains, CIPEL, accessed on May 19th 2017, developed by the dispositif Eco-Informatique ORE de l'INRA.
- Smith, R.C., Baker, K.S., 1981. Optical properties of the clearest natural waters (200–800 nm). *Appl. Opt.*, 20(2):177-184. doi: 10.1364/AO.20.000177.
- Spencer, R.J., Eugster, H.P., Jones, B.F., 1985. Geochemistry of great Salt Lake, Utah II: Pleistocene-Holocene evolution. *Geochim. Cosmochim. Acta*, 49:739–747. [https://doi.org/10.1016/0016-7037\(85\)90168-1](https://doi.org/10.1016/0016-7037(85)90168-1).
- Spyrakos, E., O'Donnell, R., Hunter, P.D., Miller, C., Scott, M., Simis, S.G.H., Neil, C., Barbosa, C.C.F., Binding, C.E., Bradt, S., Bresciani, M., Dall'Olmo, G., Giardino, C., Gitelson, A.A., Kutser, T., Li, L., Matsushita, B., Martinez-Vicente, V., Matthews, M.W., Ogashawara, I., Ruiz-Verdú, A., Schalles, J.F., Tebbs, E., Zhang, Y., Tyler, A.N., 2018. Optical types of inland and coastal waters. *Limnol. Oceanogr.*, 63(2):846-870. <https://doi.org/10.1002/lno.10674>.
- Steinmetz F, Deschamps PY, Ramon D, 2011. Atmospheric correction in presence of sun glint: application to MERIS. *Opt. Express*, 19(10):9783–9800.
- Sterckx, S.; Knaeps, E.; Adriaensen, S.; Reisen, I.; De Keukelaere, L.; Hunter, P.; Giardino, E.; Odermatt, D., 2015. OPERA: An atmospheric correction for land and water. In *Proceedings of the ESA Sentinel-3 for Science Workshop*, Venice, Italy, pp 2–5.
- Stramska, M., Stramski, D., 2005. Effects of a nonuniform vertical profile of chlorophyll concentration on remote-sensing reflectance of the ocean. *Appl. Opt.*, 44:1735–1747.
- Strickland, J.D.H., Parsons, T.R., 1968. A practical handbook of seawater analysis. *Bull. Fish. Res. Board Canada*, pp 167.
- Stumm, W., Morgan, J.J., 1996. *Aquatic chemistry: chemical equilibria and rates in natural waters*. Wiley Inter-science, 3rd edition, New York, pp 1040. ISBN: 978-0-471-51185-4.
- Tranvik, L. J. et al., 2009. Lakes and reservoirs as regulators of carbon cycling and climate. *Limnol. Oceanogr.*, 54:2298–2314.
- Toming, K., Kutser, T., Laas, A., Sepp, M., Paavel, B., Nõges, T., 2016. First experiences in mapping lake water quality parameters with Sentinel-2 MSI imagery. *Remote Sens.*, 8:640.
- Tyler J.E., 1961. Scattering properties of distilled and natural waters. *Limnol. Oceanogr.*, 6:451–456.
- Tyler, A.N., Svab, E., Preston, T., Présing, M., Kovács, A., 2006. Remote sensing of the water quality of shallow lakes: A mixture modelling approach to quantifying phytoplankton in water characterized by high-suspended sediment. *Int. J. Remote Sens.*, 27(8):1521.

- Ulloa, O., Sathyendranath, S., Platt, T., 1994. Effect of the particle-size distribution on the backscattering ratio in seawater, *Appl. Opt.*, 33:7070–7077.
- [dataset] USGS, 2006. Shuttle Radar Topography Mission, 1 Arc Second Data, Global Land Cover Facility, University of Maryland, College Park (United States).
- Van Der Woerd, H.J., Pasterkamp, R., H., 2008. HYDROPT: A fast and flexible method to retrieve chlorophyll-a from multispectral satellite observations of optically complex coastal waters. *Remote Sens. Environ.*, 112(4):1795-1807.
- Vanhellemont, Q., Ruddick, K., 2014. Turbid wakes associated with offshore wind turbines observed with Landsat 8. *Remote Sens. Environ.*, 145:105-15. <https://doi.org/10.1016/j.rse.2014.01.009>.
- Vanhellemont, Q., Ruddick, K., 2015. Advantages of high quality SWIR bands for ocean colour processing: examples from Landsat-8. *Remote Sens. Environ.*, 161(5):89-106. <https://doi.org/10.1016/j.rse.2015.02.007>.
- Vanhellemont, Q., Ruddick, K., 2016. Acolite for Sentinel-2: aquatic applications of MSI imagery. In *Proceedings of the ESA Living Planet Symposium, Prague, Czech Republic*, pp 9–13. http://od-nature.naturalsciences.be/downloads/publications/2016_Vanhellemont_ESALP.pdf.
- Vermote, E., Tanré, D., Deuzé, J.L., Herman, M., Morcrette, J.J., Kotchenova, S.Y., 2006. Second simulation of a satellite signal in the solar spectrum-vector (6SV). 6S User Guide Version3.
- Wang, G.; Lee, Z.; Mishra, D.R.; Ma, R., 2016. Retrieving absorption coefficients of multiple phytoplankton pigments from hyperspectral remote sensing reflectance measured over cyanobacteria bloom waters: Retrieval of absorption coefficients of multiple pigments. *Limnol. Oceanogr. Methods*, 14:432–447.
- Werdell, P.J., Bailey, S.W., 2005. An improved in-situ bio-optical data set for ocean color algorithm development and satellite data product validation. *Remote Sens. Environ.*, 98:122–140.
- Wells, A.J., Illing, L.V., 1964. Present-Day Precipitation of Calcium Carbonate in the Persian Gulf. *Developments in Sedimentology*, 1:429–435. [https://doi.org/10.1016/S0070-4571\(08\)70517-X](https://doi.org/10.1016/S0070-4571(08)70517-X).
- Xue, K., Zhang, Y., Duan, H., Ma, R., Loiselle, S., Zhang, M., 2015. A Remote Sensing Approach to Estimate Vertical Profile Classes of Phytoplankton in a Eutrophic Lake. *Remote Sens.*, 7:14403–14427.
- Yacobi, Y.Z., Gitelson, A., Mayo, M., 1995. Remote sensing of chlorophyll in Lake Kinneret using high spectral resolution radiometer and Landsat TM: spectral features of reflectance and algorithm development. *J. Plankton Res.*, 17(11):2155-73. <https://doi.org/10.1093/plankt/17.11.2155>.
- Yamashita, Y., Nosaka, Y., Suzuki, K., Ogawa, H., Takahashi, K., Saito, H., 2013. Photobleaching as a factor controlling spectral characteristics of chromophoric dissolved organic matter in open ocean. *Biogeosciences*, 10:7207–7217.
- Yang, Q., Stramski, D., He, M.-X., 2013. Modeling the effects of near-surface plumes of suspended particulate matter on remote-sensing reflectance of coastal waters. *Appl. Opt.*, 52:359–374.

Zaneveld, J.R.V., Barnard, A.H., Boss, E., 2005. Theoretical derivation of the depth average of remotely sensed optical parameters. *Opt. Express*, 13:9052–9061.

Zhang, X., Hu, L., He, M.-X., 2009. Scattering by pure seawater: Effect of salinity. *Opt. Express*, 17(7):5698-5710. doi 10.1364/OE.17.005698.

Zheng, Z., Ren, J., Li, Y., Huang, C., Liu, G., Du, C., Lyu, H., 2016. Remote sensing of diffuse attenuation coefficient patterns from Landsat 8 OLI imagery of turbid inland waters: a case study of Dongting Lake. *Sci. Total Environ.*, 573:39-54. <https://doi.org/10.1016/j.scitotenv.2016.08.019>.

Curriculum Vitae

Vincent NOUCHI

Rue des alpes, 2

1020, Renens

vincent.nouchi@epfl.ch

Education

- | | |
|-----------|--|
| 2014-2018 | Ph.D. candidate in the aquatic physics laboratory (APHYS) at Ecole Polytechnique Fédérale de Lausanne (EPLFL, Switzerland). Thesis untitled “ <i>Toward a systematic integration of optical remote sensing in lake water studies</i> ”. Advisors: Wüest, A., Bouffard, D., Odermatt, D., |
| 2011-2013 | M.sc. in environmental science at University of Versailles (Paris, France) |

Experience

- | | |
|-----------|---|
| 2017 | Teaching assistant. <i>Imagery of territory</i> with Frank de Morsier for M.sc. students. |
| 2017 | M.sc. co-supervision: Sonia Dupuis. “ <i>Validation of Landsat-8 and Sentinel-2 algorithms for atmospheric correction on Lake Geneva</i> ” |
| 2016 | Teaching assistant. Linear algebra for B.sc. students. |
| 2013-2015 | <i>Léman-Baïkal</i> project. Management and collection of a large database in Lake Geneva (Switzerland) and Lake Baïkal (Russia) of in-situ optical and bio-geochemical measurements concurrent to airborne observations of an ultralight aircraft equipped with hyperspectral cameras (see conference papers below). |

Conference papers

Akhtman, Y., Constantin, D., Rehak, M., Nouchi, V., Shinkareva, G., Bouffard, D., Pasche, N., Chalov, S., Lemmin, U., Merminod, B., 2014. *Leman-baikal: Remote sensing of lakes using an ultralight plane*, 6th Workshop on Hyperspectral Image and Signal Processing, 2014.

Cubero-Castan, M., Constantin, D., Barbieux, K., Nouchi, V., Akhtman, Y., Merminod, B., 2015. *A new smoothness based strategy for semi-supervised atmospheric correction: Application to the léman-Baïkal campaign*, 7th Workshop on Hyperspectral Image and Signal Processing: Evolution in Remote Sensing (WHISPERS), Tokyo, 1-4. doi: 10.1109/WHISPERS.2015.8075379

Barbieux, K., Nouchi, V., Merminod, B., 2016. *Airborne hyperspectral sensor radiometric self-calibration using near-infrared properties of deep water and vegetation*, SPIE remote sensing, proceedings volume 9999, Remote Sensing of the Ocean, Sea Ice, Coastal Waters, and Large Water, 9999OM, doi: 10.1117/12.2241251

Software & OS

Matlab, python, c++, Hydrolight, Linux, Windows

